Dielectric Relaxation and Frequency Dependence of HfO_2 Doped by Lanthanide Elements

A Thesis Submitted to

University of Liverpool

in Partial Fulfillment of the Requirements for

the Degree of Doctor of Philosophy

in the Department of Electrical Engineering and Electronics

by

Chun Zhao

Master of Science in IC Design,

Hong Kong University of Science and Technology, Hong Kong, 2007

Bachelor of Science in Communication Engineering

Southeast University, Nanjing, China, 2006

Abstract

The decreasing sizes in complementary metal oxide semiconductor (CMOS) transistor technology requires the replacement of SiO_2 with gate dielectrics that have a high dielectric constant (*k*). When the SiO_2 gate thickness was reduced below 1.4 nm, electron tunneling effects and high leakage currents occurred which presented serious obstacles for the reliability issue in terms of metal-oxide-semiconductor field-effect transistor (MOSFET) devices. In recent years, various alternative gate dielectrics have been researched. Following the introduction of HfO_2 into the 45 nm process by Intel in 2007, the screening and selection of high-*k* gate stacks, understanding their properties, and their integration into CMOS technology has been a very active research area. Frequency dispersion of high-*k* dielectrics was commonly observed and classified into two parts: extrinsic and intrinsic causes. The frequency dependence of the dielectric constant (*k*-value), that is the intrinsic frequency dispersion, could not be assessed before suppressing the effects of extrinsic frequency dispersion, such as the effects of the lossy interfacial layer (between the high-*k* thin film and silicon substrate) and the parasitic effects. The significance of parasitic effects

(including series resistance and the back metal contact of the metal-oxide-semiconductor (MOS) capacitor) on frequency dispersion was studied. The effect of the lossy interfacial layer on frequency dispersion was investigated and modeled using a dual frequency technique. The effect of surface roughness on frequency dispersion is also investigated. Several mathematic models were discussed to describe the dielectric relaxation of high-*k* dielectrics. Some of the relaxation behavior can be modeled using the Curie-von Schweidler (CS) law, the Kohlrausch-Williams-Watts (KWW) relationship and the Havriliak-Negami (HN) relationship. Other relaxation models were also introduced. For the physical mechanism, dielectric relaxation was found to be related to the degree of polarization, which was dependent on the structure of the high-*k* material. The degree of polarization was attributed to the enhancement of the correlations among polar nano-scale size domain within the materials. The effect of grain size for the high-*k* materials' structure mainly originated from higher surface stress in smaller grain size due to its higher concentration of grain boundary.

Acknowledgments

After years of intense studies on high-*k* gate dielectrics, the moment has come to finalize this chapter of my life. Moreover, it is the time to recognize the support from many colleagues I have received throughout the graduate studies period of time. Without their help and support, the comprehensive study presented here would not have been possible.

First of all, I would like to thank my primary supervisor Prof. Ce Zhou Zhao for supporting my idea of carrying out a PhD from many years ago. His confidence in me has been the base for an effective and fruitful collaboration. His technical guidance and valuable insights are extremely important for the underlying research works. Besides, he is not only a master in scientific technique, but also a good mentor in living and learning. Prof. Zhao gave me not only the supervision on my research but also the guidance on my future career. It has been a great pleasure working with him.

Also, I wish to express my most sincere appreciation to my supervisors: Prof. Steve Taylor and Prof. Paul Chalker. They always encouraged me to expand my knowledge and to be innovative. They let me pursue my research independently and gave their best support by all means. Again, I would thank

them for their insightful technical guidance and steady encouragement.

I also deeply appreciate Dr. Sang Lam, Dr. Moncef Tayahi, Dr. Eng Gee Lim, Dr. Jin Ling Zhang and Dr. Kalok Man for their advice and support throughout my PhD period. Their help have been essential for the successful completion of the research program studied here.

As a member of the same research team, my colleagues: Mr. Jing Jin Wu, Mr. Yi Fei Mu and Mr. Qi Feng Lu are gratefully acknowledged for the tremendous assistances in their respective fields of interest. The success of this work is to a large extent as a result of their effort.

Beside the contribution from my colleagues, Dr. Ji Min Xiao, Dr. Shi Cheng, Dr. Yun Gang Zhang and Dr. Yuan Qian Wang at the University of Liverpool are gratefully acknowledged for their help in the respective fields and, moreover, for taking the lead in several related issues both in research and life.

Special thanks to Mr. Yu Zhao and Ms. Yong Ping Cheng for educating me and providing me with the necessary base to start my PhD. Your faith and support was of great help throughout the years. I owe deep gratitude to my parents and to all my family, for their love, for their patience with me during all these years.

Finally, there is one who deserves a distinct acknowledgement, my fiancée Viola Wang. Viola, thanks to you and your family for the time we spend together. Without your help I would not have been able to accomplish

this in such a period of time. My heartiest appreciation goes to you for your infinite love that always keeps me moving forwards.

It would be difficult for me to adequately thank all those who have helped me these years. So this is the moment and the part where I would like to express my gratitude to everyone involved. Thank you and best wishes.

Gary C. Zhao

Nov. 2013

List of Publications

{Impact Factor, Journal Citation Report Ranking in Category (Q1, Q2, Q3 and Q4)}

JOURNAL ARTICLES

[1] **Chun Zhao**, C Z Zhao, M Werner, S Taylor and P R Chalker, *Dielectric Relaxation of High-k Oxides*, 8, 456, ***Nanoscale Research Letters*** (2013) {2.89, JCR Q1}

[2] **Chun Zhao**, C Z Zhao, M Werner, S Taylor, P R Chalker and P J King, *Grain Size Dependence of Dielectric Relaxation in Cerium Oxide as High-k Layer*, 8, 172, ***Nanoscale Research Letters*** (2013) {2.89, JCR Q1}

[3] **Chun Zhao**, C Z Zhao and B Da, *A Novel Technique for Arithmetic Elements Standard Cell Library Establishment Based on Tanner Tools*, 569, 273, ***Advanced Materials Research*** (2012)

[4] J Tao, C Z Zhao, **Chun Zhao**, P Taechakumput, M Werner, S Taylor and P R Chalker, *Extrinsic and Intrinsic Frequency Dispersion of High-k Materials in Capacitance-Voltage Measurements*, 5, 1005, ***Materials*** (2012) {2.25, JCR Q1}

[5] **Chun Zhao**, C Z Zhao, Jing Tao, M Werner, S Taylor, and P R Chalker, *Dielectric Relaxation of Lanthanide-Based Ternary Oxides: Physical and Mathematical Models*, Article ID 241470, ***Journal of Nanomaterial***s (2012) {1.67, JCR Q2}

[6] **Chun Zhao**, C Z Zhao, M Werner, S Taylor, and P R Chalker, *Advanced CMOS Gate Stack: Present Research Progress*, Article ID 689023, ***ISRN Nanotechnology*** (2012)

[7] C Z Zhao, M Werner, S Taylor, P R Chalker, A C Jones and **Chun Zhao**, *Dielectric Relaxation of La-Doped Zirconia Caused by Annealing Ambient*, 6, 48, ***Nanoscale Research Letters*** (2011) {2.89, JCR Q1}

CONFERENCE PAPERS

[1] C Z Zhao, S Taylor, **Chun Zhao** and P R Chalker, *Dielectric Relaxation in Lanthanide Doped/Based Oxides Used for High-k Layers*, **3rd International Conference on the Advancement of Materials and Nanotechnology (ICAMN)**, November 19-22, 2013, Penang, Malaysia

[2] C Z Zhao, **Chun Zhao**, S Taylor and P R Chalker, *Crystal Grain and Dielectric Relaxation of High-k Thin Film Deposited by ALD and MOCVD*, **5th Energy Materials Nanotechnology EAST (EMN EAST)**, September 7-10, 2013, Beijing, China

[3] **Chun Zhao**, C Z Zhao, M Werner, S Taylor, P R Chalker and P J King, *Impact of Cerium Oxide's Grain Size for Dielectric Relaxation*, ***20th International Symposium on the Physical and Failure Analysis of Integrated Circuits (IPFA)***, July 15-19, 2013, Suzhou, China

[4] C Z Zhao, J Tao, **Chun Zhao**, M Werner, S Taylor and P R Chalker, *Dielectric Relaxation of Lanthanide-based Ternary Oxides*, ***11th IEEE International Conference on Solid-State and Integrated Circuit Technology (ICSICT)***, October 29-November 1, 2012, Xi'an, China

[5] P F Wang, **Chun Zhao**, C Z Zhao and G Liu, *Dielectric Relaxation Model in High-k Materials: Simplified Kohlrausch-Williams-Watts Function*, ***11th IEEE International Conference on Solid-State and Integrated Circuit Technology (ICSICT)***, October 29-November 1, 2012, Xi'an, China

[6] **Chun Zhao**, W Pan, C Z Zhao, K L Man, J Choi and J Chang, *Performance-Effective Compaction of Standard Cell Library for Edge-triggered Latches Utilizing 0.5 Micron Technology*, ***8th International SoC Design Conference (ISOCC)***, November 17-18, 2011, Jeju, Korea

[7] **Chun Zhao**, W Zhang, C Z Zhao, K L Man, J Ma, T T Jeong and J K Seon, *Standard Cell Library Establishment and Simulation for Scan D Flip-Flops based on 0.5 Micron CMOS Mixed Signal Process*, ***8th International SoC Design Conference (ISOCC)***, November 17-18, 2011, Jeju, Korea

[8] C Z Zhao, M Werner, S Taylor, P R Chalker, A C Jones, and **Chun Zhao**, *Dielectric Relaxation of La-Doped Zirconia Caused by Annealing Ambient*, ***3rd Collaborative Conference on Interacting Nanostructures (CCIN)***, April 19-23, 2010, San Diego, US

[9] C Z Zhao, M Werner, S Taylor, P R Chalker, A C Jones and **Chun Zhao**, *Effects of Lanthanide Doping on Dielectric Properties of Hafnia and Zirconia*, ***3rd Collaborative Conference on Interacting Nanostructures (CCIN)***, April 19-23, 2010, San Diego, US

List of Figures

List of Tables

Table of Contents

Chapter 1: Literature Review

With the advance of metal oxide semiconductor technology, Si based semiconductors, with SiO_2 as an outstanding dielectric, have been dominating microelectronic industry for decades. Recently, some semiconductor companies have moved to the leading-edge of the 32 nm technology and successfully realized advanced product development. Presently, companies are continuing research beyond 22 nm of complementary metal oxide semiconductor (CMOS) technology[1]. In the current version of the International Technology Roadmap for Semiconductors (ITRS), the scaling of the metal-oxide-semiconductor field-effect transistor (MOSFET) is projected to the year 2016 when the channel length should be 9 nm[2]. MOSFETs have been scaled down, and the physical thickness of SiO_2 dielectrics becomes as thin as 1.4 nm (just a few atomic layers)[3]. As the thickness of SiO_2 gate dielectric films used in complementary metal oxide semiconductor (CMOS) devices was reduced toward 1 nm, the gate leakage current level became unacceptable[1-3]. The reduction of oxide thicknesses resulted in increased gate leakage current, which was a difficult obstacle to be solved, particularly for large density

circuits[4]. Extensive efforts have been focused on finding alternative gate dielectrics for future technologies to overcome leakage current problem[5-7]. Oxide materials with large dielectric constants (so-called high-*k* dielectrics) have attracted much attention due to their potential application as gate dielectrics in MOSFETs[8-12]. The benefits of high-*k* dielectrics can be understood from Equation 1-1:

$$t_{eq} = t_{SiO2}\frac{\varepsilon_{high-k}}{\varepsilon_{SiO2}} = t_{SiO2}\frac{\varepsilon_{high-k}}{3.9} \quad (\varepsilon_{high\text{-}k} > \varepsilon_{SiO2}) \quad 1\text{-}1$$

where t_{eq} represents an equivalent oxide thickness (EOT), a quantity used to compare performance of high-*k* dielectric MOS gates with SiO_2-based MOS gates. The EOT is the thickness of SiO_2 gate oxide needed to obtain the same gate capacitance as that obtained with thicker high-*k* dielectrics. Thicker equivalent oxide thickness, to reduce the leakage current of gate oxides, was obtained by introducing the high-*k* dielectric to real application[13-15].

1.1 High-*k* Materials

In the past ten years, significant progress has been made in the screening and selection of high-*k* gate dielectrics, understanding their physical

properties, and their integration into CMOS technology. Now it has been recognized that a large family of oxide-based materials emerged as leading candidates to replace SiO_2 gate dielectrics in advanced CMOS applications[16-17]. There are a number of high-*k* dielectrics that have been actively pursued to replace SiO_2. Among them are cerium oxide (CeO_2)[18-25], cerium zirconate ($CeZrO_4$)[26], gadolinium oxide (Gd_2O_3)[27-29], erbium oxide (Er_2O_3)[30-31], neodymium oxide (Nd_2O_3)[32-33], aluminum oxide (Al_2O_3)[34-35], lanthanum aluminum oxide ($LaAlO_3$)[36-37], lanthanum oxide (La_2O_3)[38], yttrium oxide (Y_2O_3)[39], tantalum pentoxide (Ta_2O_5)[40], titanium dioxide (TiO_2)[41], zirconium dioxide (ZrO_2)[42-43], lanthanum doped zirconium oxide ($La_xZr_{1-x}O_{2-\delta}$)[44-45], hafnium oxide (HfO_2)[46], HfO_2-based oxides ($La_2Hf_2O_7$[47], $Ce_xHf_{1-x}O_2$)[48], hafnium silicate ($HfSi_xO_y$)[49], and rare-earth scandates ($LaScO_3$[50], $GdScO_3$[51], $DyScO_3$[52], and $SmScO_3$[53]). The detailed feature list for some of the high-*k* materials is presented in Table 1-1.

Table 1-1. High-*k* materials feature list [27-31,34-35, 40-46,48-49,51]

Oxide	Dielectric Constant	Features (including deposition, physical or electrical properties)
HfO_2	17-18	deposited by liquid injection atomic layer deposition (LI-ALD) and PDA in nitrogen (N_2) ambient
$CeHfO_2$	32	low hysteresis voltages and negligible flat band

		voltage shifts
$ErHfO_2$	28-30	its dopant elements have been demonstrated to stabilize the cubic fluorite and tetragonal phases of HfO_2
HfTiON	18.9	has an improved C-V characteristics and reduced leakage current have been achieved from HfTiON gate dielectric MOS capacitor
$HfSiO_2$	17.7	exhibits excellent C-V characteristics with an EOT of 1.3 nm which are sufficient for implementing high mobility MOSFETs using compressively strained SiGe channels in future CMOS technology
TiO_2	55	has well behaved C-V curves observed but high leakage curent
HfTaON /AlON	20	exhibits low interface state to oxide-charge densities, low gate leakage, small CET about 1.1 nm; incorporation of N into both the interlayer and high-*k* dielectric further improve the device reliability under high field stress through the formation of strong N-related bonds
$LaZrO_2$	11-14	shows good dielectric properties with low hysteresis voltages and negligible flat band voltage shifts
$GeZrO_2$	37.7	Has a very high-*k* value at low deposition

		temperatures and with excellent thermal stability
$LaZrO_2$	40	La-doped ZrO_2 thin films grown by O_3-based atomic layer deposition directly on Ge; Ge is widely considered due to its higher carrier motilities
$PrAlO_x$	14	combines the advantages of the high permittivity of the lanthanide oxide with the chemical and thermal stability of Al_2O_3
Gd_2O_3	10.6	exhibits the best electrical characteristics, including the lowest gate leakage current, the lowest noise spectra density, and the high power performance
$GdScO_3$	23	has small hysteresis and low leakage current densities

Among them, HfO_2, HfO_2-based materials, ZrO_2 and ZrO_2-based materials are considered as the most promising candidates combining high dielectric permittivity and thermal stability with low leakage current due to a reasonably high barrier height that limits electron tunneling. CeO_2 is also proposed to be a possible gate dielectric material, because it has high dielectric constant. CeO_2 has been successfully added to HfO_2 in order to stabilize the high-*k* cubic and tetragonal phases. Consequently, $La_xZr_{1-x}O_{2-\delta}$, $La_2Hf_2O_7$, $Ce_xHf_{1-x}O_2$ and CeO_2 have received lots of attentions as the promising high-*k* gate dielectric materials for their potential applications in

sub-32nm node CMOS devices.

1.2 High-k Dielectric Deposition

Thin-film deposition is the art of applying a thin film to a surface and including any technique for depositing a thin film of material onto a substrate or onto other previously deposited layers. Deposition techniques fall into two broad categories, depending on whether the process is primarily chemical or physical. Chemical deposition is further categorized by the phase of the precursor. Plating relies on liquid precursors, often a solution of water with a salt of the metal to be deposited. Chemical solution deposition (CSD) uses a liquid precursor, usually a solution of organometallic powders dissolved in an organic solvent. Chemical vapor deposition (CVD) generally uses a gas-phase precursor, often a halide or hydride of the element to be deposited. Physical deposition uses mechanical, electromechanical or thermodynamic means to produce a thin film of solid. Examples of physical deposition include thermal evaporation, sputtering, pulsed laser deposition, cathodic arc deposition and electro-hydrodynamic deposition. Some methods fall outside these two categories, relying on a mixture of chemical and physical means including reactive sputtering, molecular beam epitaxy and topotaxy. The properties of the thin films produced have been reported to be closely dependent on the

growth method. Studies to gain insight into any correlation among the properties of the films, the interfacial layers, and growth condition have been investigated.

Atomic layer deposition (ALD), a variant of CVD, is a popular technique used to deposit ultrathin metal-oxide layers with excellent electrical characteristics and conformal structure because of the layer-by-layer nature of the deposition kinetics[54]. The growth mechanism of ALD can be simply expressed as the surface exchange reactions between the chemisorbed metal-containing precursor fragments and the precursor which introduces the oxygen in the case of oxide deposition. The ALD growth mechanism can be described as a four step process, where a precursor gas is initially introduced followed by an inert gas to remove unreacted precursor from the reactor chamber. A second precursor is introduced, which completes the layer followed by inert gas to remove unreacted precursor. In self-limiting ALD, the growth surface becomes saturated with the precursor forming a new species that is unreactive with the precursor, so that the deposition automatically self-limits at one or two monolayers. Therefore, the growth rate in the system is surface-controlled. Unfortunately, many organometallic precursors commonly used for oxide growth do not exhibit a distinct self-limiting ALD window. Thus, the deposition rate in these processes is dependent on the temperature. Additionally some precursors would deposit films with a relatively high concentration of residual impurities originating from the

ligands, which is unfavorable for gate dielectrics. The choice of precursors providing low contamination and ability to self-limit is a critical issue for the ALD growth of high quality oxide films. ALD can be used to deposit several types of thin films, including various oxides (e.g. Al_2O_3, TiO_2, SnO_2, ZnO, HfO_2), metal nitrides (e.g. TiN, TaN, WN, NbN), metals (e.g. Ru, Ir, Pt), and metal sulfides (e.g. ZnS).

Metal-organic chemical vapor deposition, MOCVD, is a widely used technique of growth of the thin films[55]. Recently, as high-*k* dielectric materials came under extensive investigation, MOCVD emerged as a viable candidate for high-*k* film deposition on Si. Some oxide precursors used for high-*k* materials have low vapor pressure and low thermal stability, both of which are detrimental to the growth. This problem can be solved by applying liquid injection of precursors dissolved in a solvent. This takes place not in a vacuum, but from the gas phase at moderate pressures (2 to 100 kPa). As such, this technique is preferred for the formation of devices incorporating thermodynamically metastable alloys, and it has become a major process in the manufacture of optoelectronics. Even so, there remain some requirements for the precursors to meet: the precursors should be soluble and stable but not reactive to each other in the same liquid solution.

In general, each deposition technique has been pursued or developed because it has unique advantage over others. However, each process technology has certain limitations. In order to optimize the desired film

characteristics, a good understanding of the advantages and restrictions applicable to each technology is necessary. A table of the most popular techniques (MOCVD and ALD) is presented (in Table 1-2) and the feature of process methods for thin film deposition is briefly discussed[56-57].

Table 1-2. MOCVD and ALD feature list

Deposition Technique	**MOCVD**
Main Advantages	MOCVD is not restricted to a line-of-sight deposition which is a general characteristic of sputtering, evaporation and other PVD processed. Deep trenches, holes and other complex 3D configuration can usually be coated with relative ease. The deposition rate is high and thick coatings can be readily obtained. MOCVD equipment does not normally require ultrahigh vacuum and can be adapted to many process variations, which makes MOCVD generally more competitive and, in some cases, more economical than PVD.
Main	A major issue is the requirement of having chemical

Disadvantages	precursors (the starting materials) with suitable thermal and chemical properties. This is what makes precursor development so challenging and important. There is continuous need to develop novel concepts for the synthesis of improved chemical precursors with tailored physico-chemical properties.
Deposition Technique	**ALD**
Main Advantages	The main advantages of ALD over other gas-phase deposition techniques include: precise film thickness control by simply changing the number of deposition cycles without controlling the dose of the precursor. Similarly, uniform doping is easy to be accomplished by the growth cycle by a doping cycle at a desired interval. Another advantages and inherent feature of ALD originates from its surface-controlled nature. It allows substrates of various sizes and geometries to be conformably coated within the deposition process.
Main	A main disadvantage of ALD in certain applications is the

Disadvantages	fact that it is a relatively slow technique when thicker films of hundreds of nanometers need to be deposited. In addition, the ALD process is entirely dictated by precursor chemistry, which makes the availability of suitable chemical precursors the most critical issue for the successful development of new ALD process. This is especially true for the ALD of rare earth oxides where the very limited number of true ALD processes is mainly due to the lack of suitable precursors. There is a clear demand for novel precursor concepts, which are able to meet the demands of semiconductor industry.

1.3 Objectives of Thesis

Capacitance-voltage (C-V) measurements are the fundamental characterization technique for MOS devices. It could be used for the extraction of the oxide thickness[58], the maximal width of the depletion layer, and the interface trap densities[59]. Also, some other important parameters could be obtained, like channel length[60], mobility[61], threshold voltage, bulk doping profile[62], and the distribution of the charges in dielectrics, which is

used to evaluate the interface states between the substrate and dielectric. Frequency dispersion in SiO_2 has frequently been observed in C-V measurements[63-64]. Several models and analytical formulae have been thoroughly investigated for correcting the measurement errors. Attention has been given to eliminate the effects of series resistance[65], oxide leakage, undesired lossy interfacial layer (very thin) between oxide and semiconductor[66], surface roughness[67], polysilicon depletion[68–70] and quantum mechanical effect[71-74]. Since dielectric relaxation and associated losses impaired MOSFET performance, the larger dielectric relaxation of most high-*k* dielectrics compared with SiO_2 was a significant issue for their applications[75-80]. However, there is insufficient information about dielectric relaxation of high-*k* thin films, which prompts us to investigate the underlying mechanism. In the thesis, the dielectric relaxation of the high-*k* dielectric was discussed.

In the thesis, the extrinsic and intrinsic causes of frequency dispersion during capacitance-frequency (C-V or *C-f*) measurements in high-*k* thin films were investigated. In order to reconstruct the measured C-V curves for any given measurement data, parasitic components including imperfection of the back contact and silicon series resistance which was one of the extrinsic causes of frequency dispersion must be taken into account. The corrected capacitance was provided following related models. Furthermore, another extrinsic cause of frequency dispersion, lossy interfacial layer effect, of high-*k* MOS capacitances was investigated for zirconium oxides and then a four-element

circuit model was introduced. Frequency dispersion from the effect of surface roughness was obviously demonstrated in ultra-thin SiO_2 MOS devices[67] while the analysis of the $La_xZr_{1-x}O_{2-\delta}$ thin film and $Ce_xZr_{1-x}O_{2-\delta}$ thin film led to the conclusion that surface roughness was not responsible for the observed frequency dispersion for the thick high-*k* dielectric. The polysilicon depletion effect and quantum confinement should be also considered. The extrinsic causes of frequency dispersion during C-V measurement were studied in Chapter 3 before validating dielectric relaxation. After taking into account all extrinsic causes of frequency dispersion mentioned above, the intrinsic effect (dielectric relaxation) of high-*k* dielectric thin films arose and several dielectric relaxation models were discussed. The dielectric relaxation results of $Ce_xZr_{1-x}O_{2-\delta}$, $LaAlO_3$, ZrO_2 and $La_xZr_{1-x}O_{2-\delta}$ thin films could be described by the Curie-von Schweidle (CS) law, the Kohlrausch-Williams-Watts (KWW) and the Havriliak-Negami (HN) relationships, respectively. The higher *k*-values were obtained from $La_xZr_{1-x}O_{2-\delta}$ and $Ce_xZr_{1-x}O_{2-\delta}$ thin films with the low lanthanide concentration levels (e.g., $x \sim 0.1$) where the more severe dielectric relaxation was observed. In order to describe dielectric relaxation, many mathematic models were discussed in Chapter 4. After the mathematic models were finalized by fitting experimental data, physical mechanisms of dielectric relaxation were investigated in Chapter 5. Dielectric relaxation behaviors observed in the high-*k* dielectrics were partly due to the level of stress in the crystalline grains and the grain size. This behavior is analogous

to the behavior of ferroelectric ceramics.

References

1. L. Yan, C. M. Lopez, R. O. Shrestha, E.A. Irene, A. A. Suvorova, M. Saunders, Magnesium oxide as a candidate high-k gate dielectric, *Appl. Phys. Lett.* 2006, 88, 142901.
2. The International Technology Roadmap for Semiconductors (ITRS) Roadmap. ITRS Roadmap 2013/2014, http://public.itrs.net/.
3. S. Chen, Y. Zhu, R. Xu, Y. Q. Wu, X. J. Yang, Y. L. Fan, Z. M. Jiang, J. Zou, Superior electrical properties of crystalline ErO films epitaxially grown on Si substrates, *Appl. Phys. Lett.* 2006, 88, 222902.
4. A. A. Dakhel, Characterisation of Nd_2O_3 thick gate dielectric for silicon, *Phys. Status Solidi.* 2004, 201, 745.
5. Rahmani M, Ahmadi MT, Abadi HKF, Saeidmanesh M, Akbari E, Ismail R: Analytical modeling of trilayer graphene nanoribbon Schottky-barrier FET for high-speed switching applications. *Nanoscale Research Letters* 2013, 8: 55.
6. Ding SJ, Chen HB, Cui XM, Chen S, Sun QQ, Zhou P, Lu HL, Zhang DW, Shen C: Atomic layer deposition of high-density Pt nanodots on Al_2O_3 film

using (MeCp)Pt(Me)$_3$ and O_2 precursors for nonvolatile memory applications. *Nanoscale Research Letters* 2013, 8: 80.

7. Chalker PR, Werner M, Romani S, Potter RJ, Black K, Aspinall HC, Jones AC, Zhao CZ, Taylor S, Heys PN: Permittivity enhancement of hafnium dioxide high-*k* films by cerium doping. *Appl Phys Lett* 2008, 93: 182911.
8. Chen SH, Liao WS, Yang HC, Wang SJ, Liaw YG, Wang H, Gu HS, Wang MC: High-performance III-V MOSFET with nano-stacked high-*k* gate dielectric and 3D fin-shaped structure. *Nanoscale Research Letters* 2012, 7: 431.
9. Wang JC, Lin CT, Chen CH: Gadolinium oxide nanocrystal nonvolatile memory with HfO_2/Al_2O_3 nanostructure tunneling layers. *Nanoscale Research Letters* 2012, 7: 177.
10. Shi L, Liu ZG: Characterization upon electrical hysteresis and thermal diffusion of $TiAl_3O_x$ dielectric film. *Nanoscale Research Letters* 2011, 6: 557.
11. Khomenkova L, Sahu BS, Slaoui A, Gourbilleau F: Hf-based high-*k* materials for Si nanocrystal floating gate memories. *Nanoscale Research Letters* 2011, 6: 172.
12. Chen FH, Her JL, Shao YH, Matsuda YH, Pan TM: Structural and electrical characteristics of high-*k* Er_2O_3 and Er_2TiO_5 gate dielectrics for a-IGZO thin-film transistors. *Nanoscale Research Letters* 2013, 8: 18.
13. Dalapati G, Wong TS, Li Y, Chia C, Das A, Mahata C, Gao H, Chattopadhyay S, Kumar M, Seng H, Maiti C, Chi D: Characterization of

epitaxial GaAs MOS capacitors using atomic layer-deposited TiO_2/Al_2O_3 gate stack: study of Ge auto-doping and p-type Zn doping. *Nanoscale Research Letters* 2012, 7: 99.

14. An YT, Labbé C, Khomenkova L, Morales M, Portier X, Gourbilleau F: Microstructure and optical properties of Pr^{3+}-doped hafnium silicate films. *Nanoscale Research Letters* 2013, 8: 43.
15. Zhou P, Ye L, Sun QQ, Wang PF, Jiang AQ, Ding SJ, Zhang DW: Effect of concurrent joule heat and charge trapping on RESET for NbAlO fabricated by atomic layer deposition. *Nanoscale Research Letters* 2013, 8: 91.
16. D. P. Brunco, A. Dimoulas, N. Boukos, M. Houssa, T. Conard, K. Martens, C. Zhao, F. Bellenger, M. Caymax, M. Meuris, M.M. Heyns, Materials and electrical characterization of molecular beam deposited CeO_2 and CeO_2/HfO_2 bilayers on germanium, *J. Appl. Phys.* 2007, 102, 024104.
17. Y. Nishikawa, N. Fukushima, N. Yasuda, K. Nakayama, S. Ikegawa, Electrical Properties of Single Crystalline CeO_2 High-k Gate Dielectrics Directly Grown on Si (111), *Jpn. J. Appl. Phys.* 2002, 41, 1, 2480.
18. King PJ, Werner M, Chalker PR, Jones AC, Aspinall HC, Basca J, Wrench JS, Black K, Davies HO, Heys PN: Effect of deposition temperature on the properties of CeO_2 films grown by atomic layer deposition. *Thin Solid Films* 2011, 519:4192-4195.
19. Aspinall HC, Bacsa J, Jones AC, Wrench JS, Black K, Chalker PR, King PJ, Marshall P, Werner M, Davies HO, Odedra R: Ce(IV) complexes with

donor-functionalized alkoxide ligands: improved precursors for chemical vapor deposition of CeO_2. *Inorg Chem* 2011, 50: 11644–11652.

20. Phokha S, Pinitsoontorn S, Chirawatkul P, Poo-arporn Y, Maensiri S: Synthesis, characterization, and magnetic properties of monodisperse CeO_2 nanospheres prepared by PVP-assisted hydrothermal method. *Nanoscale Research Letters* 2012, 7: 425.
21. Fukuda H, Miura M, Sakuma S, Nomura S: Structural and electrical properties of crystalline CeO_2 films formed by metaorganic decomposition. *Jpn J Appl Phys* 1998, 37: 4158-4159.
22. Santha NI, Sebastian MT, Mohanan P, Alford NM, Sarma K, Pullar RC, Kamba S, Pashkin A, Samukhina P, Petzelt J: Effect of doping on the dielectric properties of cerium oxide in the microwave and far-infrared frequency range. *J Am Ceram Soc* 2004, 87: 1233–1237.
23. Nishikawa Y, Fukushima N, Yasuda N, Nakayama K, Ikegawa S: Electrical properties of single crystalline CeO_2 high-*k* gate dielectrics directly grown on Si (111). *Jpn J Appl Phys* 2002, 41: 2480–2483.
24. Jacqueline S, Black WK, Aspinall HC, Jones AC, Bacsa J, Chalker PR, King PJ, Werner M, Davies HO, Heys PN: MOCVD and ALD of CeO_2 thin films using a novel monomeric Ce^{IV} alkoxide precursor. *Chem Vap Deposition* 2009, 15: 259-261.
25. Tye L, ElMasry NA, Chikyow T, McLarty P, Bedair SM: Electrical characteristics of epitaxial CeO_2 on Si(111). *Appl Phys Lett* 1994, 65: 3081.

26. Gross MS, Ulla MA, Querini CA: Catalytic oxidation of diesel soot: New characterization and kinetic evidence related to the reaction mechanism on K/CeO_2 catalyst. *Applied Catalysis A: General* 2009, 360, 1: 81-88.
27. Pan TM, Liao CS, Hsu HH, Chen CL, Lee JD, Wang KT, Wang JC: Excellent frequency dispersion of thin gadolinium oxide high-*k* gate dielectrics. *Applied Physics Letters* 2005, 87, 26: 262908-262908.
28. Koveshnikov S, Tsai WOI, Lee JC, Torkanov V, Yakimov M, Oktyabrsky S: Metal-oxide-semiconductor capacitors on GaAs with high-*k* gate oxide and amorphous silicon interface passivation layer. *Applied Physics Letters* 2006, 88, 2: 022106-022106.
29. Robertson J, Falabretti B: Band offsets of high-k gate oxides on III-V semiconductors. *Journal of Applied Physics* 2006, 100, 1: 014111-014111.
30. Pan TM, Chen CL, Yeh WW, Hou SJ: Structural and electrical characteristics of thin erbium oxide gate dielectrics. *Applied Physics Letters* 2006, 89, 22: 222912-222912.
31. Liu CH, Pan TM, Shu WH, Huang KC: Physical and electrical properties of Ti-doped Er_2O_3 films for high-*k* gate dielectrics. *Electrochemical and Solid-State Letters* 2007, 10, 8: G54-G57.
32. Anthony J, Aspinall HC, Chalker PR, Potter RJ, Manning TD, Loo YF, O'Kane R, Gaskell JM, Smith LM: MOCVD and ALD of high-*k* dielectric oxides using Alkoxide precursors. *Chemical Vapor Deposition* 2006, 12: 83-98.

33. Laha A, Bugiel E, Osten HJ, Fissel A: Crystalline ternary rare earth oxide with capacitance equivalent thickness below 1nm for high-k application. *Applied Physics Letters* 2006, 88, 17: 172107-172107.

34. Souza D, Kiewra JPE, Sun Y, Callegari A, Sadana DK, Shahidi G, Webb DJ: Inversion mode n-channel GaAs field effect transistor with high-*k*/metal gate. *Applied Physics Letters* 2008, 92, 15: 153508-153508.

35. Adamopoulos G, Thomas S, Bradley DD, McLachlan MA, Anthopoulos TD: Low-voltage ZnO thin-film transistors based on Y_2O_3 and Al_2O_3 high-*k* dielectrics deposited by spray pyrolysis in air. *Applied Physics Letters* 2011, 98: 123503.

36. Yan L, Lu HB, Tan GT, Chen F, Zhou YL, Yang GZ, Liu W, Chen ZH: High quality, high-*k* gate dielectric: amorphous $LaAlO_3$ thin films grown on Si (100) without Si interfacial layer. *Applied Physics A* 2003, 77, 5: 721-724.

37. Lu XB, Liu ZG, Zhang X, Huang R, Zhou HW, Wang XP, Nguyen BY: Investigation of high-quality ultra-thin $LaAlO_3$ films as high-*k* gate dielectrics. *Journal of Physics D: Applied Physics* 2003, 36, 23: 3047.

38. Gougousi T, Kelly MJ, Terry DB, Parsons GN: Properties of La-silicate high-k dielectric films formed by oxidation of La on silicon. *Journal of Applied Physics* 2003, 93, 3: 1691-1696.

39. Mahata CM, Bera K, Das T, Mallik S, Hota MK, Majhi B, Verma S, Bose PK, Maiti CK: Charge trapping and reliability characteristics of sputtered Y_2O_3 high-*k* dielectrics on N-and S-passivated germanium. *Semiconductor Science*

and Technology 2009, 24, 8: 085006.

40. Pan TM, Lei TF, Chao TS, Chang KL, Hsieh KC: High quality ultrathin $CoTiO_3$ high-*k* gate dielectrics. *Electrochemical and Solid-State Letters* 2000, 3, 9: 433-434.
41. Kim SK, Kim KM, Kwon OS, Lee SW, Jeon CB, Park WY, Hwang CS, Jeong J: Structurally and electrically uniform deposition of high-*k* TiO_2 thin films on a Ru electrode in three-dimensional contact holes using atomic layer deposition. *Electrochemical and Solid-State Letters* 2005, 8, 12: F59-F62.
42. Abermann S, Pozzovivo G, Kuzmik J, Strasser G, Pogany D, Carlin JF, Grandjean N, Bertagnolli E: MOCVD of HfO_2 and ZrO_2 high-*k* gate dielectrics for InAlN/AlN/GaN MOS-HEMTs. *Semiconductor Science and Technology* 2007, 22, 12: 1272.
43. Adamopoulos G, Thomas S, Wöbkenberg PH, Bradley DD, McLachlan MA, Anthopoulos TD: High-mobility low-voltage ZnO and Li-doped ZnO transistors based on ZrO_2 high-k dielectric grown by spray pyrolysis in ambient air. *Advanced Materials* 2011, 23, 16: 1894-1898.
44. Gaskell JM, Jones AC, Aspinall HC, Taylor S, Taechakumput P, Chalker PR, Heys PN, Odedra R: Deposition of lanthanum zirconium oxide high-*k* films by liquid injection atomic layer deposition. *Applied Physics Letters* 2007, 91, 11: 112912-112912.
45. Gaskell JM, Jones AC, Chalker PR, Werner M, Aspinall HC, Taylor S, Taechakumput P, Heys PN: Deposition of lanthanum zirconium oxide

high-*k* films by liquid injection ALD and MOCVD. *Chemical Vapor Deposition* 2007, 13, 12: 684-690.

46. Gutowski M, Jaffe JE, Liu CL, Stoker M, Hegde RI, Rai RS, Tobin PJ: Thermodynamic stability of high-*k* dielectric metal oxides ZrO_2 and HfO_2 in contact with Si and SiO_2. In MRS Proceedings, 716, 1, *Cambridge University Press* 2002.
47. Dimoulas A, Vellianitis G, Mavrou G, Apostolopoulos G, Travlos A, Wiemer C, Fanciulli M, Rittersma ZM: $La_2Hf_2O_7$ high-*k* gate dielectric grown directly on Si (001) by molecular-beam epitaxy. *Applied Physics Letters* 2004, 85, 15: 3205-3207.
48. Gang H, Deng B, Sun ZQ, Chen XS, Liu YM, Zhang LD: CVD-derived Hf-based High-k Gate Dielectrics. *Critical Reviews in Solid State and Materials Sciences* 2013, 38, 4: 235-261.
49. Watanabe H, Saitoh M, Ikarashi N, Tatsumi T: High-quality HfSixOy gate dielectrics fabricated by solid phase interface reaction between physical –vapor -deposited metal-Hf and SiO_2 underlayer. *Applied Physics Letters* 2004, 85, 3: 449-451.
50. Darbandy G, Ritzenthaler R, Lime F, Garduño I, Estrada M, Cerdeira A, Iñiguez B: Analytical modeling of direct tunneling current through gate stacks for the determination of suitable high-*k* dielectrics for nanoscale double-gate MOSFETs. *Semiconductor Science and Technology*, 2011, 26, 4: 045002.

51. Myllymäki P, Roeckerath M, Putkonen M, Lenk S, Schubert J, Niinistö L, Mantl S: Characterization and electrical properties of high-*k* $GdScO_3$ thin films grown by atomic layer deposition. *Applied Physics A* 2007, 88, 4: 633-637.

52. Chan KC, Lee PF, Li DF, Dai JY: Memory characteristics and the tunneling mechanism of Au nanocrystals embedded in a $DyScO_3$ high-*k* gate dielectric layer. *Semiconductor Science and Technology* 2011, 26, 2: 025015.

53. Milanov AP, Xu K, Cwik S, Parala H, de los Arcos T, Becker HW, Devi A: Sc_2O_3, Er_2O_3, and Y_2O_3 thin films by MOCVD from volatile guanidinate class of rare-earth precursors. *Dalton Transactions* 2012, 41, 45: 13936-13947.

54. N. Izyumskaya, Y. Alivov, H. Morkoc, Oxides, oxides, and more oxides: high-κ oxides, ferroelectrics, ferromagnetics, and multiferroics, *Critical Review in Solid State and Materials Sciences*, 2009, 34, 89.

55. R. Huang, H. M. Wu, J. F. Kang, D. Y. Xiao, X. L. Shi, X. An, Y. Tian, R. S. Wang, L. L. Zhang, X. Zhang, Y. Y. Wang, Challenges of 22 nm and beyond CMOS technology, *Sci. China Ser. F-Inf. Sci*, 2009, 52, 9, 1491.

56. A. P. Milanov, Ph.D Thesis: MOCVD and ALD of Rare Earth Containing Multifunctional Materials: From Precursor Chemistry to Thin Film Deposition and Applications, Ruhr University Bochum, Germany, 2010.

57. Q. H. Bao, C. Z. Chen, D. G. Wang, Q. M. Ji, T. Q. Lei, The influences of target properties and deposition times on pulsed laser deposited hydroxyapatite films, *Appl. Surf. Sci.* 2005, 252, 5.

58. Ricco, B.; Olivo, P.; Nguyen, T.N.; Kuan, T.-S.; Ferriani, G. Oxide-thickness determination in thin-insulator MOS structures. *IEEE Trans. Electron Devices*, 1988, *35*, *4*, 432–438.
59. Terman, L.M. An investigation of surface states at a silicon/silicon oxide interface employing metal-oxide-silicon diodes. *Solid-State Electronics* 1962, *5*, *5*, 285–299.
60. Lee, S.-W. A capacitance-based method for experimental determination of metallurgical channel length of submicron LDD MOSFET's. *IEEE Trans. Electron Devices* 1964, *41*, *3*, 403–412.
61. Huang, C.L.; Faricelli, J.V.; Arora, N.D. A new technique for measuring MOSFET inversion layer mobility. *IEEE Trans. Electron Devices* 1993, *40*, *6*, 1134–1139.
62. Sze, S.M. *Physics of Semiconductor Devices*; Wiley: New York, NY, USA, 1981.
63. Yang, K.J.; Chenming, H. MOS capacitance measurements for high-leakage thin dielectrics. *IEEE Trans. Electron Devices* 1999, *46*, *7*, 1500–1501.
64. Choi, C.-H.; Wu, Y.; Goo, J.-S.; Yu, Z.; Dutton, R.W. Capacitance reconstruction from measured C-V in high leakage nitride/oxide MOS. *IEEE Trans. Electron Devices* 2000, *47*, *10*, 1843–1850.
65. Nicollian, E.H.; Brews, J.R. MOS (metal oxide semiconductor) physics and technology. *MOS (Metal Oxide Semiconductor) Physics and Technology*; Wiley: NewYork, NY, USA, 2003.

66. Kwa, K.S.K.; Chattopadhyay, S.; Jankovic, N.D.; Olsen, S.H.; Driscoll, L.S.; O'Neill, A.G. A model for capacitance reconstruction from measured lossy MOS capacitance-voltage characteristics. *Semicond. Sci. Technol.* 2003, *18*, *2*, 82–87.

67. Hirose, M.; Hiroshima, M.; Yasaka, T.; Miyazaki, S. Characterization of silicon surface microroughness and tunneling transport through ultrathin gate oxide. *J. Vac. Sci. Technol*. *A* 1994, *12*, *4*, 1864–1868.

68. Schuegraf, K.F.; King, C.C.; Hu, C. Impact of polysilicon depeletion in thin oxide MOS device. In *VLSI Technology*, June 1992, Seattle, WA; pp. 86–90.

69. Lee, S.-W.; Liang, C.; Pan, C.-S.; Lin, W.; Mark, J.B. A study on the physical mechanism in the recovery of gate capacitance to C_{OX} in implant polysilicon MOS structure. *IEEE Electron Device Lett.* 1992, *13*, *1*, 2–4.

70. Spinelli, A.S.; Pacelli, A.; Lacaita, A.L. An improved formula for the determination of the polysilicon doping. *IEEE Electron Device Lett*. 2001, *22*, *6*, 281–283.

71. Hauser, J.R.; Ahmed, K. Characterization of ultra-thin oxides using electrical C-V and I-V measurements. *AIP Conference Proceedings*, Gaithersburg, Maryland, USA, November 1998; 449, pp. 235–239.

72. Pregaldiny, F.; Lallement, C.; Mathiot, D. Accounting for quantum mechanical effects from accumulation to inversion, in a fully analytical surface potential-based MOSFET model. *Solid State Electron.* 2004, *48*, *5*, 781–787.

73. Sune, J.; Olivo, P.; Ricco, B. Quantum-mechanical modeling of accumulation layers in MOS structure. *IEEE Trans. Electron Devices* 1992, *39*, *7*, 1732–1739.

74. Pregaldiny, F.; Lallement, C.; van Langevelde, R.; Mathiot, D. An advanced explicit surface potential model physically accounting for the quantization effects in deep-submicron. *Solid-State Electronics* 2004, *48*, *3*, 427–435.

75. Zhao CZ, Taylor S, Werner M, Chalker PR, Murray RT, Gaskell JM, Jones AC: Dielectric relaxation of lanthanum doped zirconium oxide. *Journal of Applied Physics* 2009, 105: 044102.

76. Zhao CZ, Taylor S, Werner M, Chalker PR, Gaskell JM, Jones AC: Frequency dispersion and dielectric relaxation of $La_2Hf_2O_7$. *J. Vac. Sci. Technol. B* 2009, 27, 1: 333.

77. Zhao CZ, Werner M, Taylor S, Chalker PR, Jones AC, Zhao C: Dielectric relaxation of La-doped Zirconia caused by annealing ambient. *Nanoscale Research Letters* 2011, 6: 48.

78. Zhao C, Zhao CZ, Tao J, Werner M, Taylor S, Chalker PR: Dielectric relaxation of Lanthanide-based ternary oxides: physical and mathematical models. *Journal of Nanomaterials* 2012, 241470.

79. Tao J, Zhao CZ, Zhao C, Taechakumput P, Werner M, Taylor S, Chalker PR: Extrinsic and intrinsic frequency dispersion of high-*k* materials in capacitance-voltage measurements. *Materials* 2012, 5: 1005-1032.

80. Zhao C, Zhao CZ, Werner M, Taylor S, Chalker PR, King P: Grain size

dependence of dielectric relaxation in cerium oxide as high-*k* layer. *Nanoscale Research Letters* 2013, 8: 172.

Chapter 2: Experimental

2.1 Sample Preparation

HfO_2, ZrO_2, $LaAlO_3$ thin films were deposited on n-type Si(100) substrates using liquid injection metal organic chemical vapor deposition (MOCVD) and atomic layer deposition (ALD). MOCVD and ALD carried out on an modified Aixtron AIX 200FE AVD reactor fitted with the "Trijet"™ liquid injector system. During the MOCVD experiments, oxygen was introduced at the inlet of the reactor. For the ALD experiments, the oxygen was replaced by water vapor, which was controlled by a pneumatic valve. The substrate was rotated throughout all experiments for good uniformity. All the high-*k* dielectric layers considered were 16 nm in thickness.

$La_xZr_{1-x}O_{2-\delta}$ thin films were deposited onto n-type Si(100) wafers by liquid injection atomic layer deposition (ALD) at 300 °C. Both Zr and La sources were Cp-based precursors ([$(MeCp)_2ZrMe(OMe)$] and [$(^iPrCp)_3La$]). La concentration was varied in different films. Particular attention has been given to the results from films with a La concentration of x=0.09 (55 nm) and x=0.35 (35 nm) but results are also included from films with a concentration of

x=0.22 (50 nm) and x=0, i.e. un-doped ZrO_2 (35 nm). Post deposition annealing was performed at 900°C in a pure N_2 ambient for 15 minutes. To form MOS capacitors (Au/$La_xZr_{1-x}O_2$/IL/n-Si, where IL stands for interfacial layer), metal (Au) gate electrodes with an effective contact area of $4.9\times10^{-4}cm^2$ were evaporated onto the samples. The backsides of the Si samples were cleaned with a buffered HF solution and subsequently a 200 nm thick film of Al was deposited by thermal evaporation to form an ohmic back-contact.

$La_2Hf_2O_7$ thin films were deposited on n-type Si(100) substrates by liquid injection ALD at 300°C. Both Hf and La sources are Cp-based precursors ([$(MeCp)_2HfMe(OMe)$] and [$(^iPrCp)_3La$]). The composition of the La-doped HfO_2 thin films was estimated to be $La_2Hf_2O_7$. Selected thin films were subjected to 900°C post-deposition annealing (PDA) in N_2 for 15min.

Amorphous $Ce_xHf_{1-x}O_2$ thin films (x=0.1) were deposited on n-type Si(100) substrates using liquid injection ALD. The doping level was varied up to a concentration x=0.63. The interfacial layer between high-k thin film and silicon substrate is a ~1 nm native SiO_2. Samples were then annealed at 900℃ for 15 minutes in an N_2 ambient to crystallize the thin films.

Liquid injection ALD was used to deposit CeO_2 thin films. ALD procedures were run at substrate's temperatures of 150 °C, 200 °C, 250 °C, 300 °C and 350 °C. The evaporator temperature was 100 °C and reactor pressure was 1 mbar. CeO_2 films were grown on n-Si (100) wafers. Argon carrier gas flow was 100 cm^3min^{-1}. The duration of

[Ce(mmp)$_4$]/purge/H_2O/purge was 2/2/0.5/3.5 s and the number of growth cycles was 300.

2.2 Physical Characterization

The physical properties of the high-*k* thin films were studied using Auger electron spectroscopy (AES), X-ray diffraction (XRD), medium energy ion scattering (MEIS), cross-section transmission electron microscopy (XTEM), and atomic force microscopy (AFM).

The atomic composition of the high-*k* thin films was determined by AES, which was carried out via a Varian's scanning auger spectrometer. The atomic compositions quoted are from the bulk of the film, free from surface contamination, and were obtained by combining AES with sequential argon ion bombardment until comparable compositions were obtained for consecutive data points. Compositions were based on powder reference materials.

XRD was used to study the crystallization of the high-*k* thin films and carried out using a Rikagu Miniflex X-ray diffractometer with nickel-filtered Cu Kα radiation (λ=1.5405Å) and a 2θ increment of 0.2° per minute.

MEIS was used to obtain information on the elements depth distributions, on as deposited and annealed samples. This allowed

rearrangement of atoms following annealing to be observed. It was carried out at the STFC Daresbury facility[1]. A 200 keV He^+ ion beam was used with a current of up to 200 nA and a dose per data set of 5 μC at a scattering angle of 125.3°. The angle and energy of the scattered ions were determined using a state-of-the-art toroidal electrostatic energy analyzer with a position-sensitive detector. This allows the simultaneous collection of ions from a 27° range of scattering angles and the pass energy equals to 1.6%.

XTEM was used to obtain the film thickness and information about the crystal grain size. A JEOL 3010 and a JEOL 2000FX operated at 300 keV and 200 keV, respectively.

AFM was used to investigate surface morphology of these films. Digital Instruments Nanoscope III was used for the AFM characterization in contact mode.

2.3 Electrical Characterization

Electrical properties of the films were obtained by capacitance-voltage (C-V), capacitance-frequency (C-*f*) and current-voltage (I-V) measurements. I-V measurements were carried out using a Keithley K230 programmable voltage source and a K617 type electrometer.

The C-V and C-*f* measurements system consists of two Agilent precision

LCR meters (4284A and 4275A), a desktop computer and a manual probe station. The MOS devices were wafer-probed on the probe station's loading platform and were connected through Agilent 4284A/4275A to the desktop computer with a GPIB interface, as shown in Figure 2-1. The data measured from the LCR meters were collected by the computer and saved to obtain the C-V curves automatically.

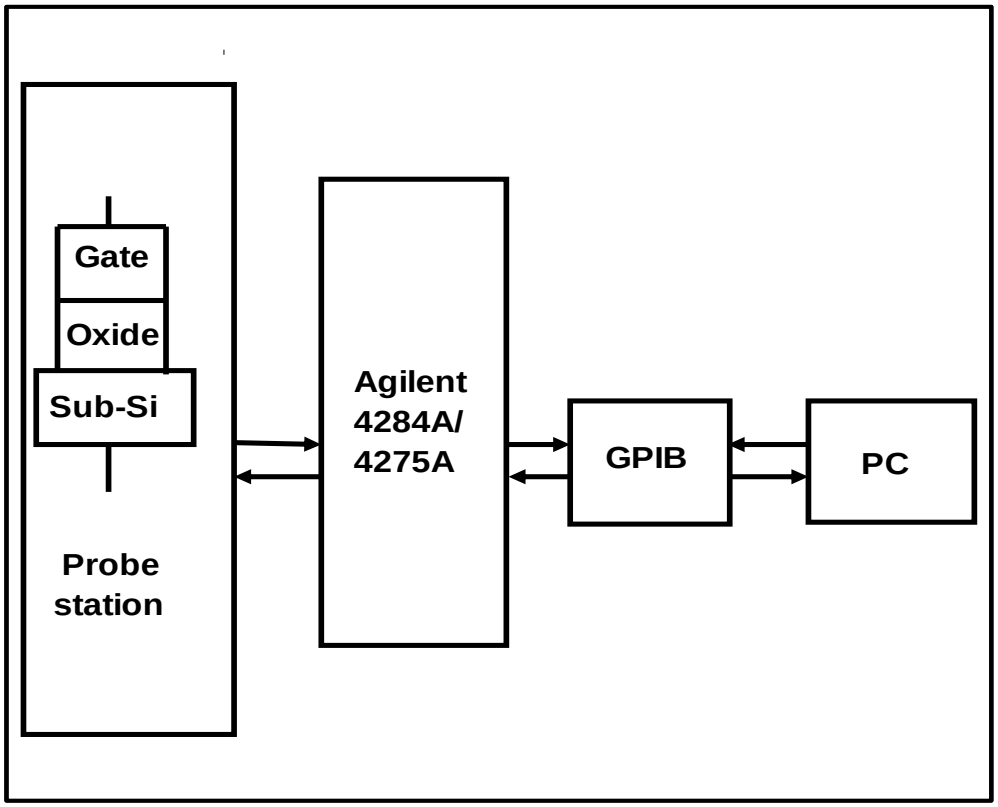

Figure 2-1. *Capacitance-voltage (C-V) measurement system of metal oxide semiconductor (MOS) devices.*

The structure of the MOS device shown in Figure 2-1 is similar to planar capacitors which are formed by metal and dielectric. The differential

capacitance of a MOS capacitor is:

$$C = A\frac{dQ_G}{dV_G} = \frac{i_{ac}}{dV_{ac}/dt} \qquad 2\text{-}1$$

where Q_G and V_G are the charge area density and voltage on the metal electrodes respectively, A is the metal electrode area, dV_{ac}/dt is the variation of AC voltage, and i_{ac} is the AC current. The capacitance of a MOS device was obtained by Agilent 4284A/4275A, which provided a small signal voltage variation rate (dV_{ac}/dt) and measured the small signal current (i_{ac}) flowing through the MOS device to calculate the differential capacitance of the MOS device according to Equation 2-1[2-3]. For the Agilent 4284A/4275A precision LCR meters, there are two optional models to calculate the device capacitance. One is the series model and the other is the parallel model, as shown in Figure 2-2. The parallel model was used in the following C-V and C-*f* measurements. In Figure 2-2, C_m is the measured capacitance. R_m and G_m are the measured resistance and conductance, respectively. C_D is the depletion capacitance and Y_{it} is the admittance due to interface states of the MOS device, and C_{ox} represents the actual frequency independent capacitance.

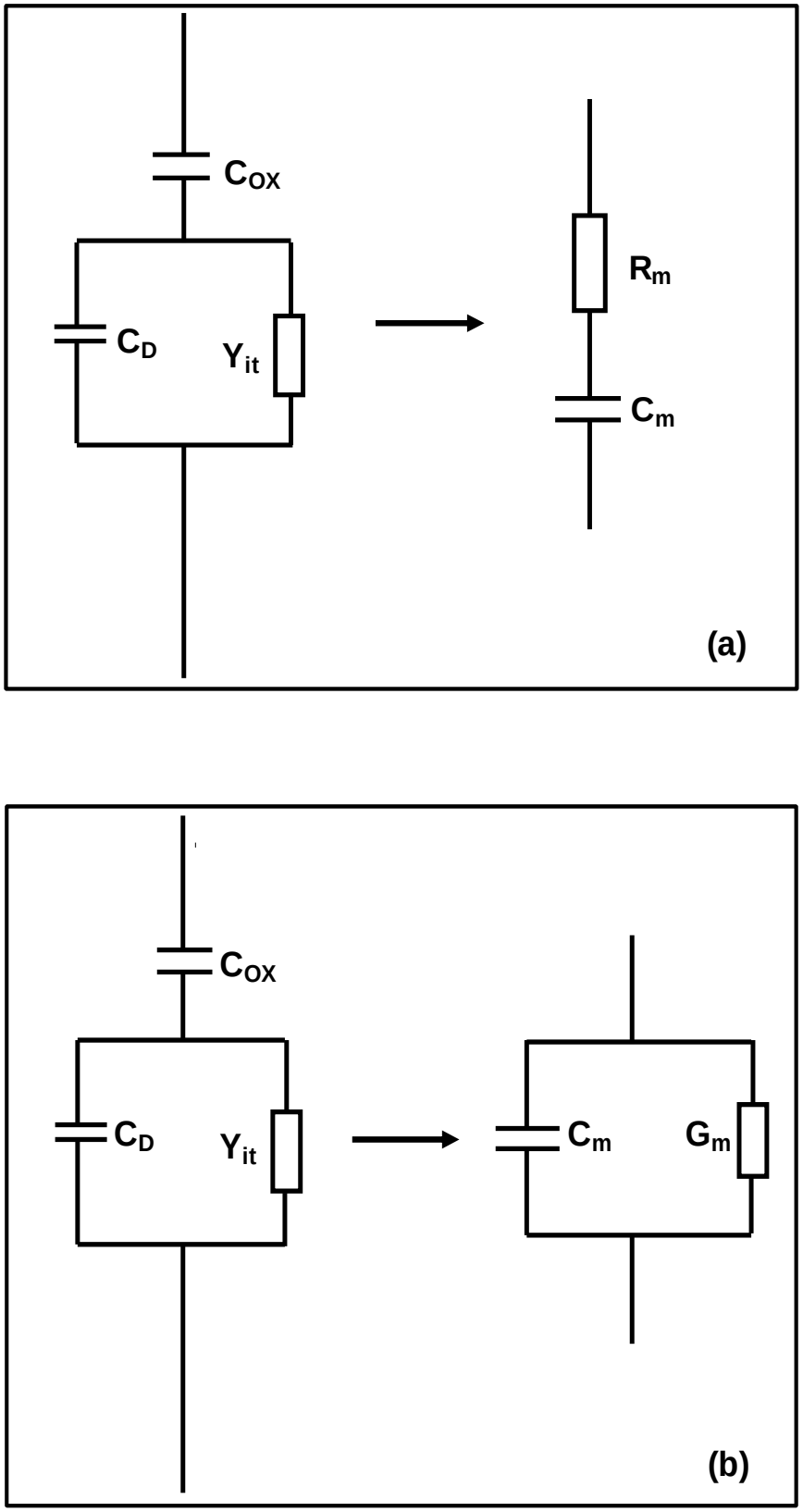

Figure 2-2. *Conventional LCR meters used to measure the device capacitance based on (**a**) Series capacitance model. (**b**) Parallel capacitance model.*

However, the influence of the leakage current of oxides on i_{ac} in the C-V and C-*f* measurements of MOS devices by the LCR meters should be taken into account. Crystalline thin films exhibit significantly higher leakage current than amorphous thin films, which could be due to the leakage pathway introduced by the grain boundaries and the local defects[4-5]. An approximation for the relative instrumental error was given by the formula:

$$E = 0.1 \times \sqrt{1 + D^2} \qquad 2\text{-}2$$

where *D* is a dissipation factor of the capacitance. Usually it can be obtained from the imaginary part of capacitance value via the C-V measurement. If the instrumentation error is less than 0.3%, the leakage current in the MOS device is negligible[6]. In the following C-V and C-*f* measurements, the leakage current in high-*k* thin films was so small that it was not contributing to frequency dispersion[7].

References

1. P. Bailey, T.C.Q. Noakes and D.P. Woodruff, A medium energy ion scattering study of the structure of Sb overlayers on Cu (111), *Surf. Sci.* 1999, **426**, 358.

2. Satter, M.M.; Haque, A. Modeling effects of interface trap states on the gate C-V characteristics of MOS devices on alternative high-mobility. *Solid-State Electronics* **2010**, *54*, *6*, 621–627.
3. Jiong, L.Z.; Ma, T.P. A new method to extract EOT of ultrathin gate dielectric with high leakage current. *IEEE Electron Device Lett*. **2004**, *25*, *9*, 655–657.
4. Bierwagen, O.; Geelhaar, L.; Gay, X.; Piešinš, M.; Riechert, H.; Jobst, B.; Rucki, A. Leakage currents at crystallites in $ZrAl_xO_y$ thin films measured by conductive atomic-force microscopy. *Appl. Phys. Lett*. **2007**, *90*, *23*, 232901.
5. Böscke, T.S.; Govindarajan, S.; Kirsch, P.D.; Hung, P.Y.; Krug, C.; Lee, B.H. Stabilization of higher-tetragonal HfO_2 by SiO_2 admixture enabling thermally stable metal-insulator-metal capacitors. *Appl. Phys. Lett*. **2007**, *91*, *7*, 072902.
6. Kwa, K.S.K.; Chattopadhyay, S.; Jankovic, N.D.; Olsen, S.H.; Driscoll, L.S.; O'Neill, A.G. A model for capacitance reconstruction from measured lossy MOS capacitance-voltage characteristics. *Semicond. Sci. Technol.* **2003**, *18*, *2*, 82–87.
7. Zhao, C.Z.; Taylor, S.; Werner, M.; Chalker, P.R.; Murray, R.T.; Gaskell, J.M.; Jones, A.C. Dielectric relaxation of lanthanum doped zirconium oxide. *J. Appl. Phys.* **2009**, *105*, *4*, 044102.

Chapter 3: Extrinsic Causes of Frequency Dispersion

Frequency dispersion was categorized into two parts: extrinsic dispersion and intrinsic dispersion. Chapter 3 presents the extrinsic frequency dispersion. After analyzing the C-V curves of SiO_2 MOS capacitors (MOSC), the parasitic effect is introduced in Section 3.1. Dispersion could be minimized by depositing an Al thin film at the back of the silicon substrate. The mathematical models were able to show that the dispersion can be minimized as well. The existence of frequency dispersion in the $LaAlO_3$ sample is discussed in Section 3.2, which is mainly due to the effect of the lossy interfacial layer between the high-*k* thin film and silicon substrate of the MOSC. Relatively larger thickness of the high-*k* thin film than the interfacial layer significantly relieved frequency dispersion. Also, extracted C-V curves were reconstructed by mathematic correction models. Frequency dispersion resulting from the effect of surface roughness was represented in an ultra-thin SiO_2 MOS device, which is discussed in Section 3.3. Furthermore, the surface property of the $La_xZr_{1-x}O_{2-\delta}$ thin films is studied. In Section 3.4 two possible extrinsic causes: polysilicon depletion effect and quantum mechanical

confinement, for frequency dispersion are considered.

Several causes for unwanted frequency dispersions in SiO_2 have been investigated. These causes includes surface roughness[1], polysilicon depletion[2-4], quantum confinement (only for an ultra-thin oxide layer)[5-8], parasitic effect (including series resistance, back contact imperfection and cables connection)[9-11], oxide tunneling leakage current (direct tunneling current, F-N tunneling *etc*.)[12], unwanted interfacial lossy layer[13] and dielectric constant (*k*-value) dependence (dielectric relaxation)[14].

Firstly, the extrinsic frequency dispersion is discussed. The extrinsic causes of frequency dispersion during C-V measurement in high-*k* thin film, which were investigated step by step before validating the effects of *k*-value dependence, were parasitic effect, lossy interfacial layer and surface roughness. The other causes like tunneling leakage current and quantum confinement are negligible if the thickness of the high-*k* thin film is large enough. Polysilicon depletion effects were not considered due to the fact that metal gates were used here. The C-V results of high-*k* or SiO_2 based dielectrics are shown in Figures 3-1, 3-2 and 3-3, respectively. The parasitic effects are summarized in detail in Figure 3-4. The back contact includes imperfection $R_{s'}$, $C_{s'}$, cables $R_{s''}$, $C_{s''}$ and substrate resistance R_s. The lossy interfacial layer effect is observed with C_i, G_i (between the high-*k* thin film and silicon substrate). Polysilicon depletion effect and surface roughness on high-*k* thin films are also shown in the Figure 3-4.

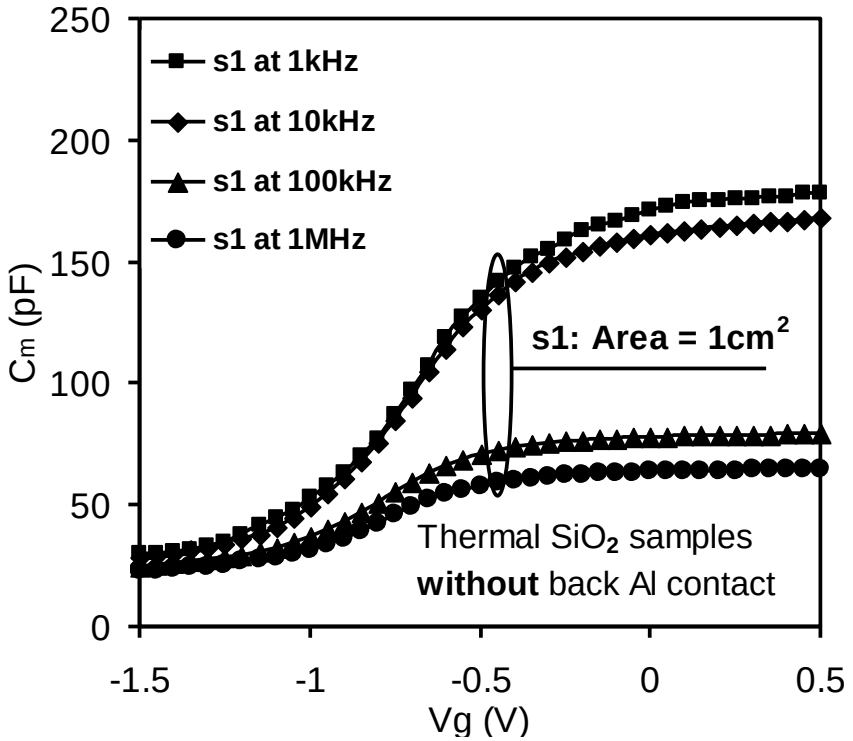

Figure 3-1. *Frequency dispersion in C-V measurements observed in the thermal oxide (SiO_2) sample.*

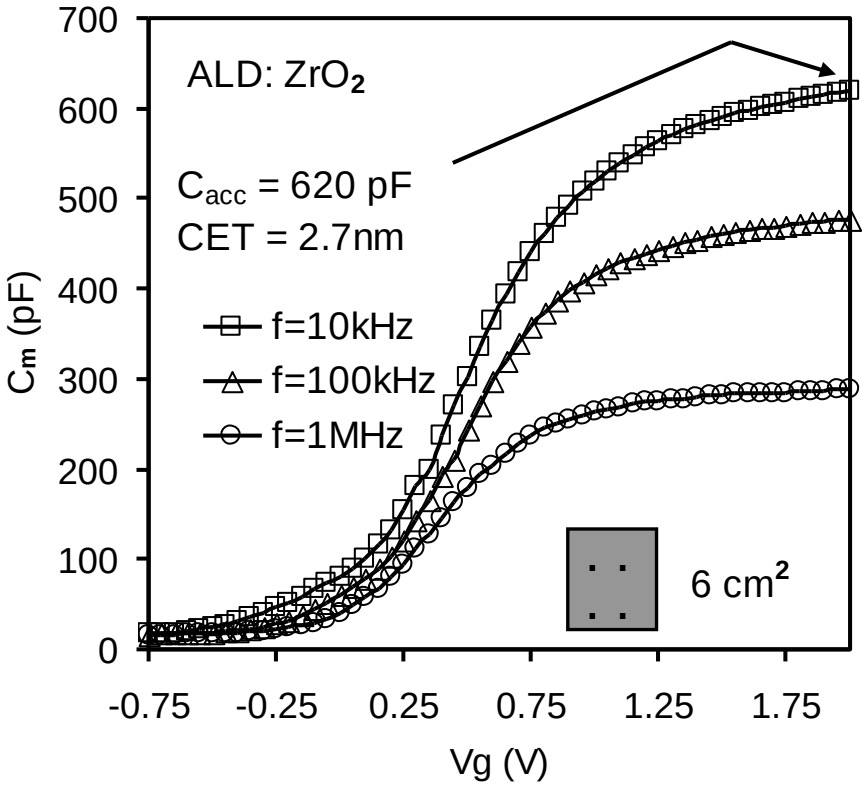

Figure 3-2. *Presence of frequency dispersion in ZrO_2 samples at different frequencies*

(10kHz, 100kHz and 1MHz).

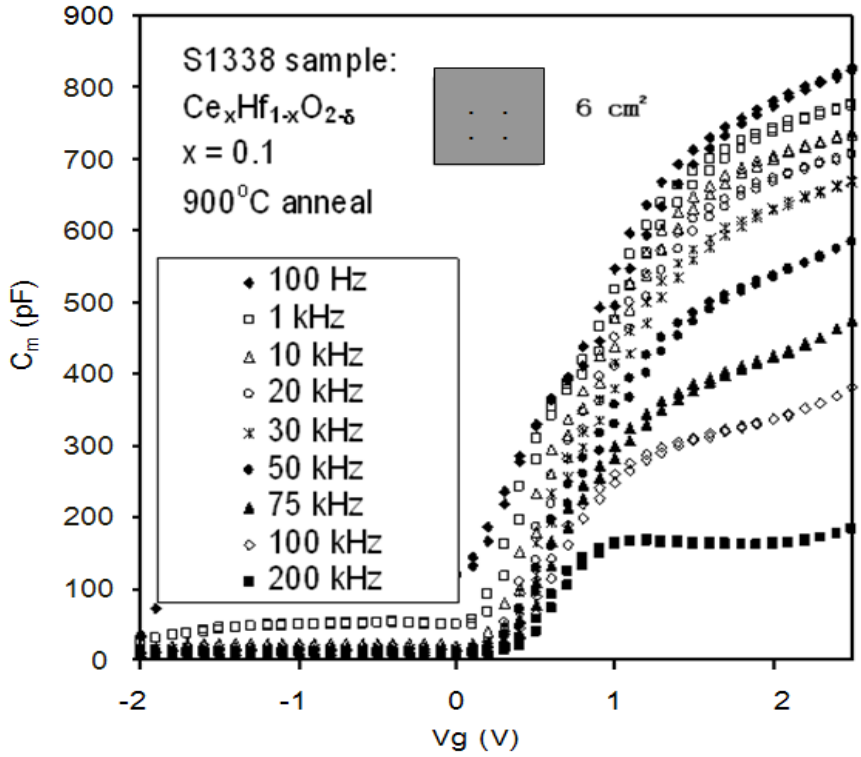

Figure 3-3. *C-V curves from a $Ce_xHf_{1-x}O_{2-\delta}$ thin film at different frequencies (from 100 Hz to 200 kHz).*

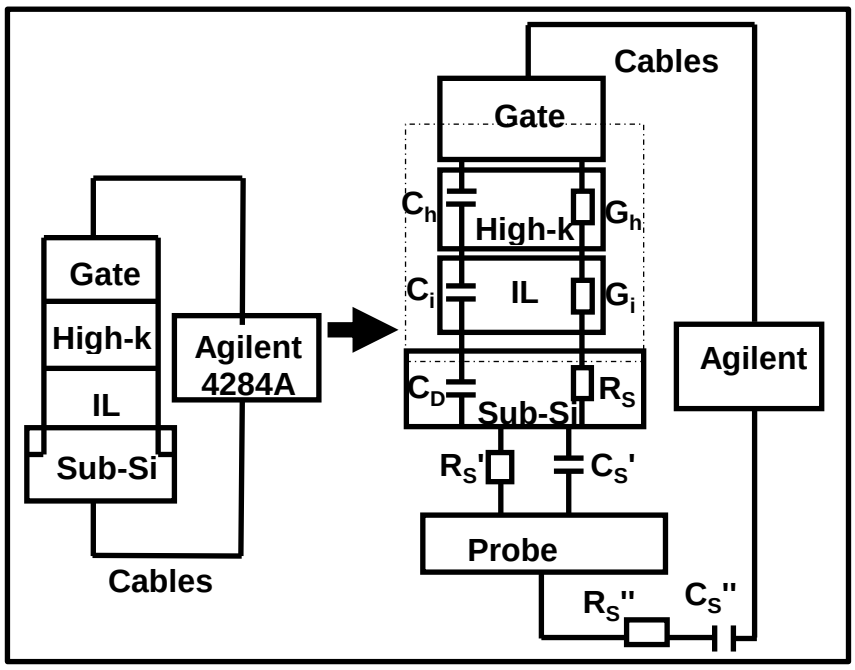

Figure 3-4. *Causes of frequency dispersion during C-V measurement in the high-k thin film were the parasitic effect.*

3.1 Parasitic Effects

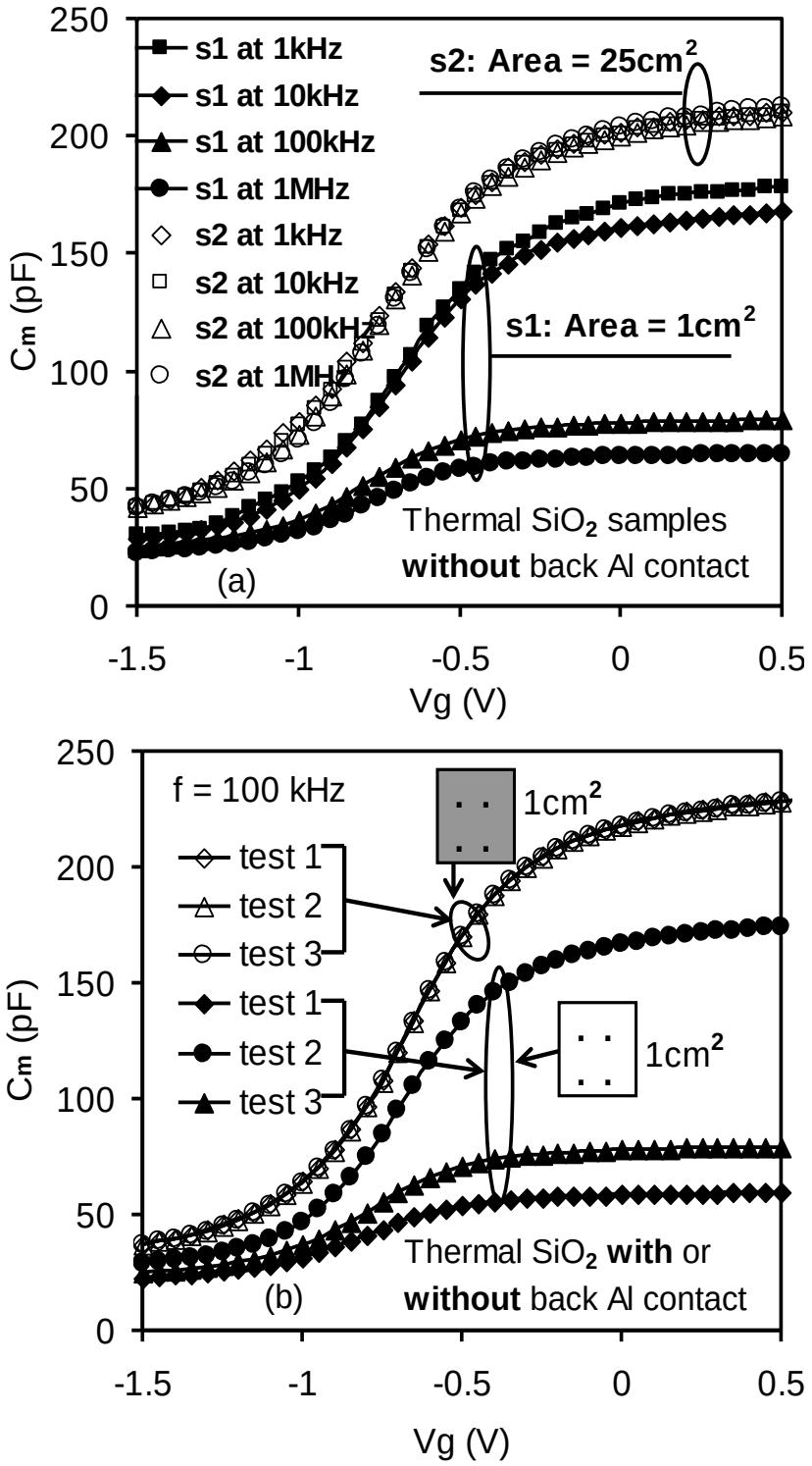

Figure 3-5. *Frequency dispersion in C-V measurements observed in thermal oxide*

*(SiO_2) samples. (**a**) In the absence of substrate back Al contact, dispersion was evident only in the sample with a smaller substrate area (denoted by s1). (**b**) The reproducibility of the tested devices in both the presence and absence of back metal contact.*

Parasitic effects in MOS devices included parasitic resistances and capacitances such as bulk series resistances, series contact, cables and many other parasitic effects[15]. Five different sources of parasitic series resistance have been suggested[16]. However, only two of them which have practical importance are listed as follows: (1) the series resistance R_S of the quasi-neutral silicon bulk between the back contact and the depletion layer edge at the silicon surface underneath the gate; and (2) the imperfect contact of the back of the silicon wafer. Frequency dispersion caused by the parasitic effect is shown in Figure 3-1.

The significance of the series resistance effect, which was common due to silicon bulk resistance and back contact imperfection, was best demonstrated in thermal SiO_2 MOS capacitors, since in this case the effect of the lossy interfacial layer between the bulk dielectric and silicon substrate can be neglected. The thickness of thermal SiO_2 was thick enough to allow the tunneling leakage current to be neglected[17-18]. Frequency dispersion in the SiO_2 capacitor was only observed in samples with small substrate effective areas as depicted in Figure 3-5a (solid symbols extracted from Figure 3-1). In addition, the measured results were also no longer reproducible for small samples in

the absence of Al back contacts, as shown in Figure 3-5b (the solid symbols). Both of the sample sets were measured three times within 24 hours. Solid symbols signified the C-V results from the sample without back Al contact (indicated by a blank square), while the opened symbols (e.g., ○) showed the C-V results from the other sample with back Al contact (indicated by a shadow square). It therefore impacted the measurement reliability.

In order to reconstruct the measured C-V curves for a set of given measurement data in the frequency domain for SiO_2, one must take into account the parasitic components that may arise due to the silicon series resistance and the imperfection of the back contact. A correction may then be applied for the measured C-V curves in order to eliminate the parasitic effects. Figure 3-6a shows an equivalent circuit of an actual case, where C_{ox} represents the actual frequency independent capacitance across the SiO_2 gate dielectric, R_S includes both the bulk resistance in the silicon substrate and contributions from various contact resistances and cable resistances. The presence of the back contact capacitance and contributions from cable capacitance were also modeled by a capacitance C_S. C_C, G_C, C_m, G_m refer to corrected (without the effect of the parasitic components R_S and C_S) measured capacitance and conductance, respectively. Following Kwa[13], the corrected capacitance C_C is given by[19]:

$$C_C = \frac{(\omega^2 C_m C_p - G_m{}^2 - \omega^2 C_m{}^2)(G_m{}^2 + \omega^2 C_m{}^2) C_p}{\omega^2 C_p{}^2 \left[G_m(1 - G_m R_S) - \omega^2 C_m{}^2 R_S\right]^2 + \left(\omega^2 C_m C_p - G_m{}^2 - \omega^2 C_m{}^2\right)^2} \qquad 3\text{-}1$$

where

$$C_p = \frac{C_{ox}\left(G_{ma}{}^2+\omega^2 C_{ma}{}^2\right)}{\omega^2\left(C_{ma}{}^2 C_{ox}-C_{ma}{}^2\right)-G_{ma}{}^2} \qquad 3\text{-}2$$

and

$$R_S = \frac{G_{ma}}{G_{ma}{}^2+\omega^2 C_{ma}{}^2} \qquad 3\text{-}3$$

where C_{ma} and G_{ma} are the capacitance and conductance measured in strong accumulation. The measured capacitance can be recovered, independently of the measurement frequencies, by applying the correction according to the model as depicted in Figure 3-6b. Dispersions disappear after considering C_S and R_S or depositing back Al contact (solid line). The blank square shows the tested device without back Al contact on silicon substrate. The effective substrate area is 1cm^2. Alternatively, the parasitic effects can simply be minimized by depositing an Al thin film on the back of the silicon substrate (open symbols in Figure 3-5b and solid line in Figure 3-6b). In summary, it has been demonstrated that once the parasitic components are taken into account, it is possible to determine the true capacitance values free from parasitic errors.

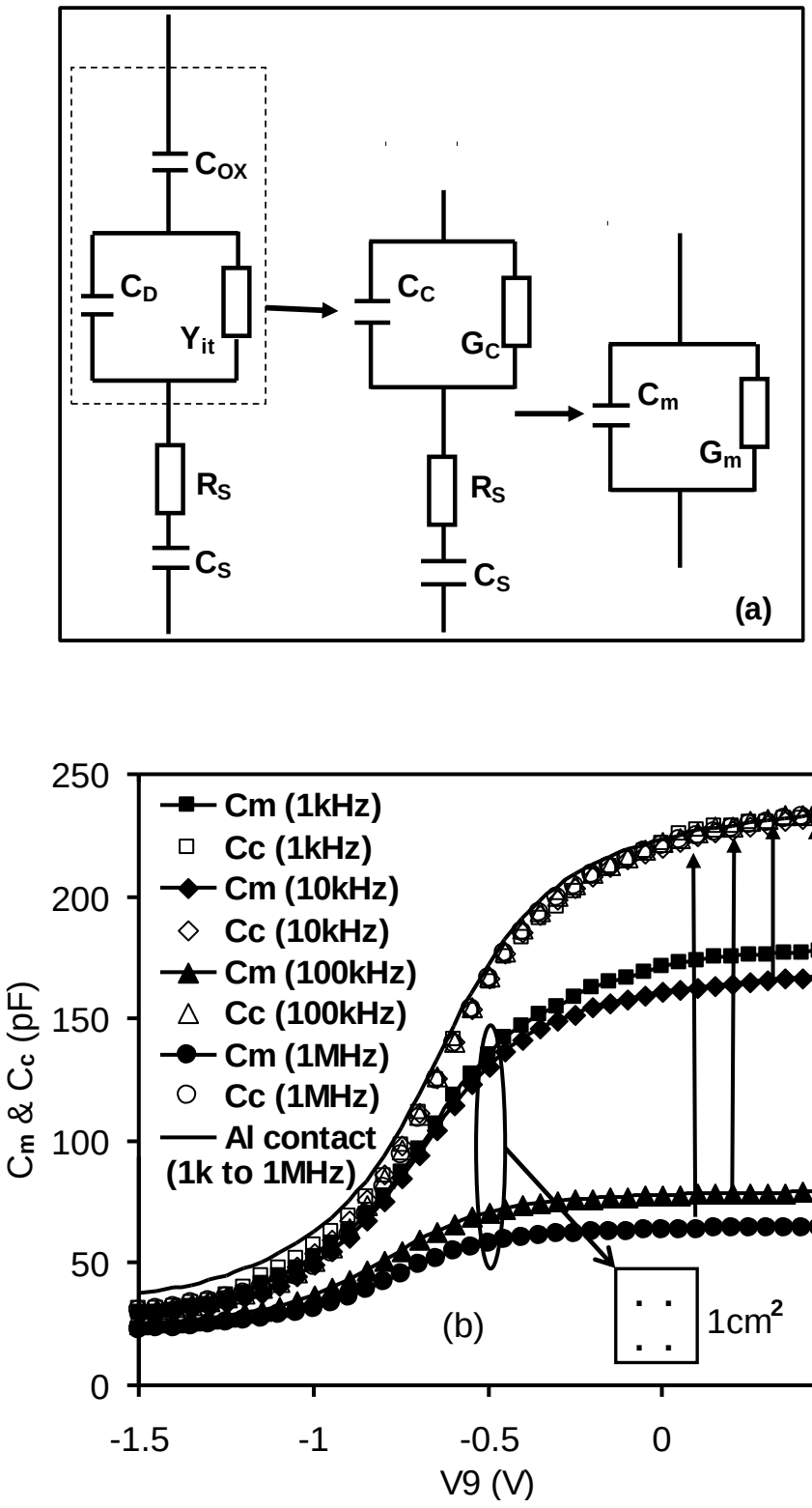

Figure 3-6. *Effects of series resistance and back contact imperfection. (**a**) Equivalent circuit model, taking into account the parasitic components from series resistance, cables and back contact imperfection (with the addition of the C_S and R_S). (**b**)*

Extracted C_C-Vg curves based on measured data C_m and G_m.

3.2 Lossy Interfacial Layer Effect

It should be noted that in Figure 3-2 the dispersion was not caused by parasitic effects, since this sample had a large substrate with an Al thin film on the back. The effect of the lossy interfacial layer between the high-*k* thin film and silicon substrate on the high-*k* MOSC was investigated.

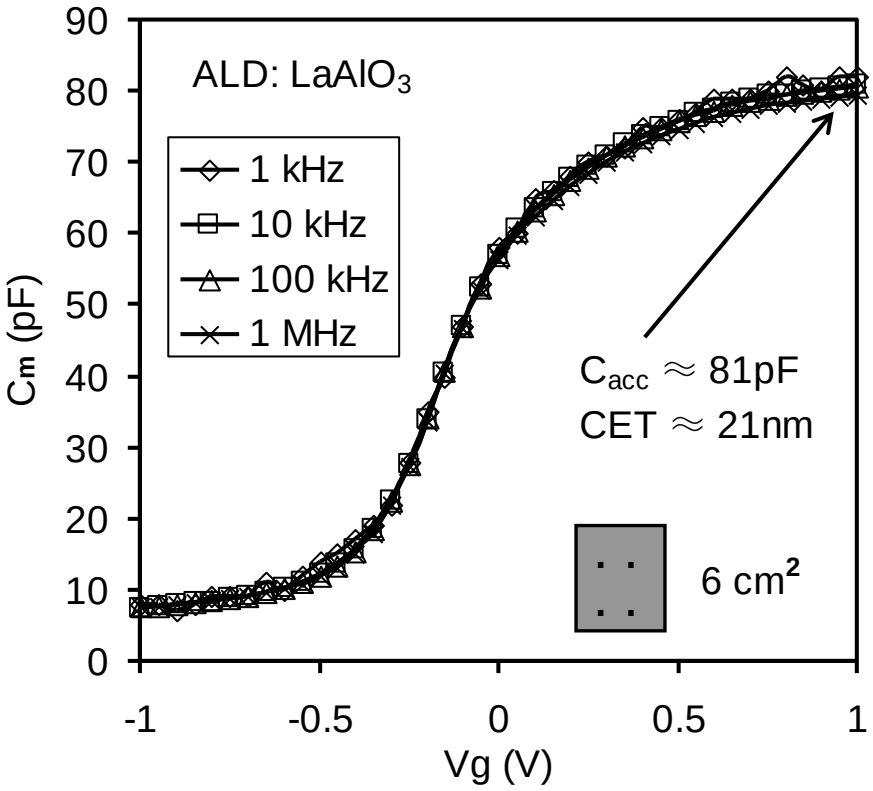

Figure 3-7. *High frequency C-V results of $LaAlO_3$ thin film.*

The absence of frequency dispersion observed in Figure 3-7 may be explained in terms of the thickness of the high-*k* thin film compared to the

interfacial layer. The absence of frequency dispersion in the $LaAlO_3$ sample is observed with an effective area of 6 cm^2 with back Al contact. C_{acc} is the capacitance in the accumulation range. In Figure 3-7, the interfacial layer thickness (~1 nm) was negligible compared with the capacitance equivalent thickness (CET) of ~ 21 nm. Therefore in this case, the high-*k* layer capacitance was much less than the interfacial layer capacitance (*i.e.*, $C_h \ll C_i$) and the effect of C_i on C_m could be ignored. Furthermore the effect of the lossy interfacial layer conductance G_i on frequency dispersion can be suppressed by replacing the native SiO_2 by a denser SiO_2 thin film. In Figure 3-2, the frequency dispersion effect was significant even with the Al back contact and the bigger substrate area. In this case, C_h (CET = 2.7 nm) was comparable with C_i (~1 nm native SiO_2) and the frequency dispersion was attributed to losses in the interfacial layer capacitance, caused by interfacial dislocation and intrinsic differences in bonding coordination across the chemically abrupt ZrO_2/SiO_2 interface.

Based on the above explanation, Figure 3-8a showed a four-element circuit model for high-*k* stacks, adapted from a dual frequency technique[20], with the capacitance value reconstructed from the loss. C_h and G_h represent the actual capacitance and conductance across the high-*k* dielectric. C_D is the depletion capacitance and Y_{it} is the admittance due to interface states, respectively. The expression for the corrected capacitance C_C, is given by[19]:

$$C_C = \frac{\Delta^2(\omega_1{}^2 - \omega_2{}^2)}{I_{m2}\omega_2\omega_1{}^2(\Delta^2+\omega_2{}^2) - I_{m1}\omega_1\omega_2{}^2(\Delta^2+\omega_1{}^2)} \qquad 3\text{-}4$$

where

$$\Delta = \frac{\omega_1 I_{m1} - \omega_2 I_{m2}}{R_{m1} - R_{m2}},\ I_{mj} = \frac{\omega_j C_{mj}}{G_{mj}{}^2 + \omega_j{}^2 C_{mj}{}^2},\ R_{mj} = \frac{G_{mj}}{G_{mj}{}^2 + \omega_j{}^2 C_{mj}{}^2} \qquad 3\text{-}5$$

and C_m and G_m are the measured capacitance and conductance and ω is the measurement angular frequency. At an angular frequency ω_j (j = 1 or 2), the measured capacitance and conductance are C_{mj} and G_{mj}, respectively. Three abstract parameters: Δ, I_{mj} , and R_{mj} have been introduced to reduce the expression of C_C. Figure 3-8b shows the corrected C-V curves from Figure 3-2. All of the extracted C-V curves closely align with one another over the three different frequency pairs to reconstruct the real capacitance values. This indicates that the presence of a lossy interfacial layer is also responsible for the frequency dispersion in high-*k* stacks.

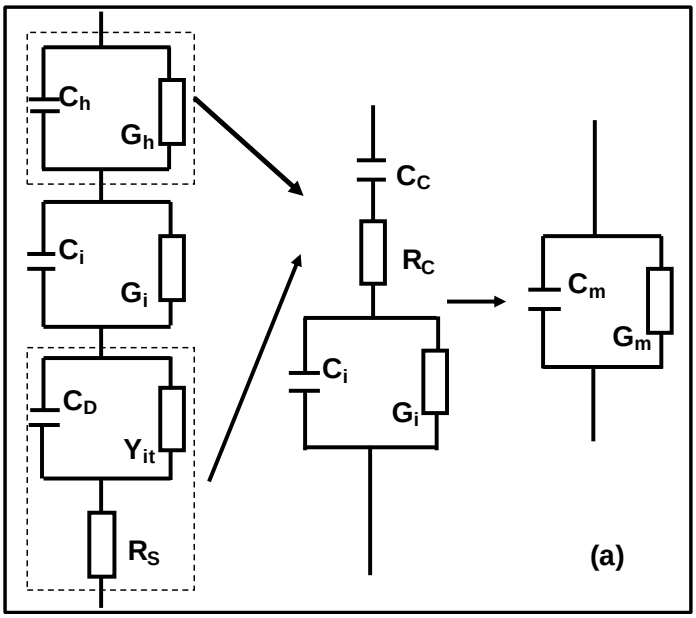

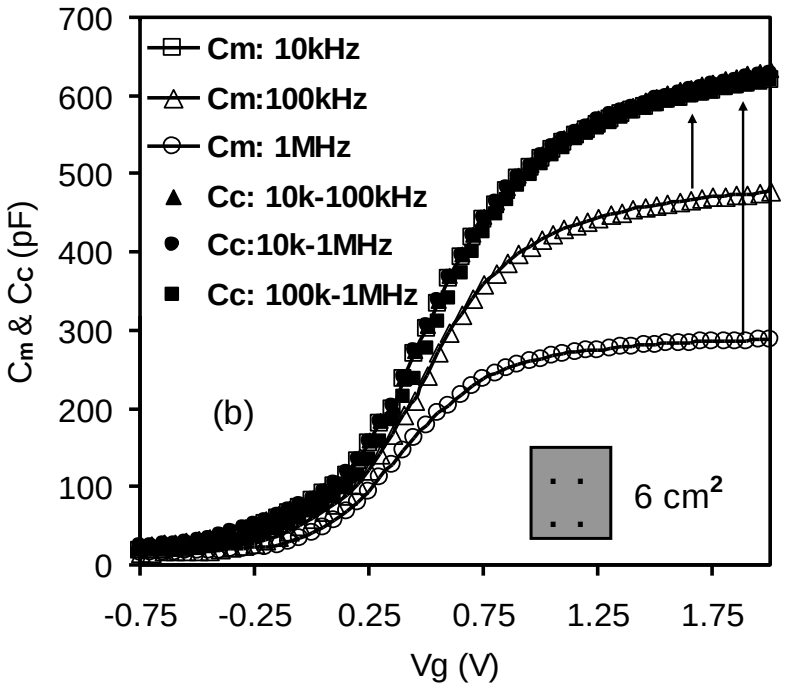

Figure 3-8. *Effect of the lossy interfacial layer on high-k stacks. (**a**) Four-element equivalent circuit model for high-k stacks. (**b**) Extracted Cc-Vg curves based on data from Figure 3-1 and Figure 3-8a.*

3.3 Surface Roughness Effect

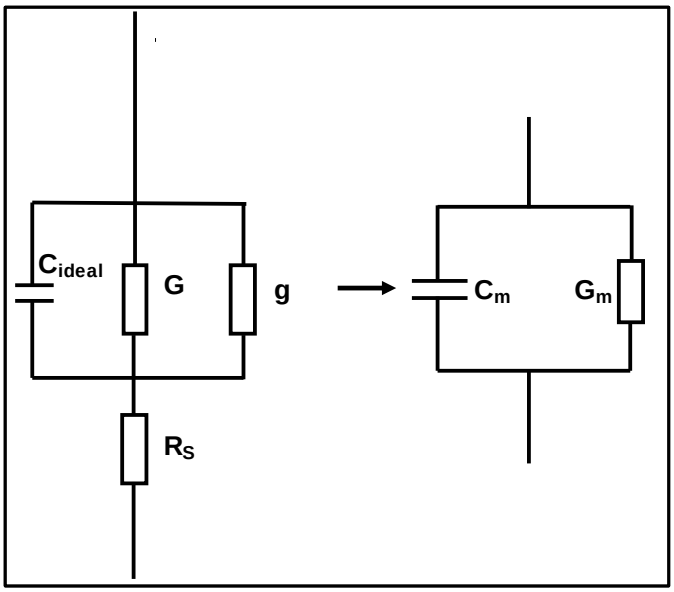

Figure 3-9. *Equivalent circuit of the parallel mode of the measurement system.*

After taking the parasitic effects and the lossy interfacial layer into account, the unwanted frequency dispersion shown in Figure 3-3 may be caused by surface roughness. Frequency dispersion from the effect of surface roughness is well demonstrated in an ultra-thin SiO_2 MOS device[1]. In the following discussion, the effects of direct tunneling, series resistance and surface roughness on the capacitance were taken into account without considering quantum confinement and the polysilicon depletion effect. From Figure 3-9, the measured capacitance C_m is given by[21]:

$$C_m = \frac{C_{ideal}}{[(G+g)R_S+(\omega C_{ideal}R_S)]^2} \qquad 3\text{-}6$$

where G is the conductance due to a pure tunneling effect, g is the conductance due to the surface roughness effect, and R_S is the series resistance. The real capacitance taking into account the surface roughness, C_{ideal}, can be calculated and it is independent of frequency[21]. It was found that the surface roughness affects frequency dispersion when the thickness of ultra-thin oxides is ~1.3nm. To investigate whether the unwanted frequency dispersion of the high-k materials in Figure 3-3 is caused by the surface roughness or not, the surface properties of the $La_xZr_{1-x}O_{2-\delta}$ thin films was studied using AFM. The typical AFM micrographs of the $La_xZr_{1-x}O_{2-\delta}$ annealed thin films (x = 0.35 and x = 0.09) are shown in Figure 3-10.

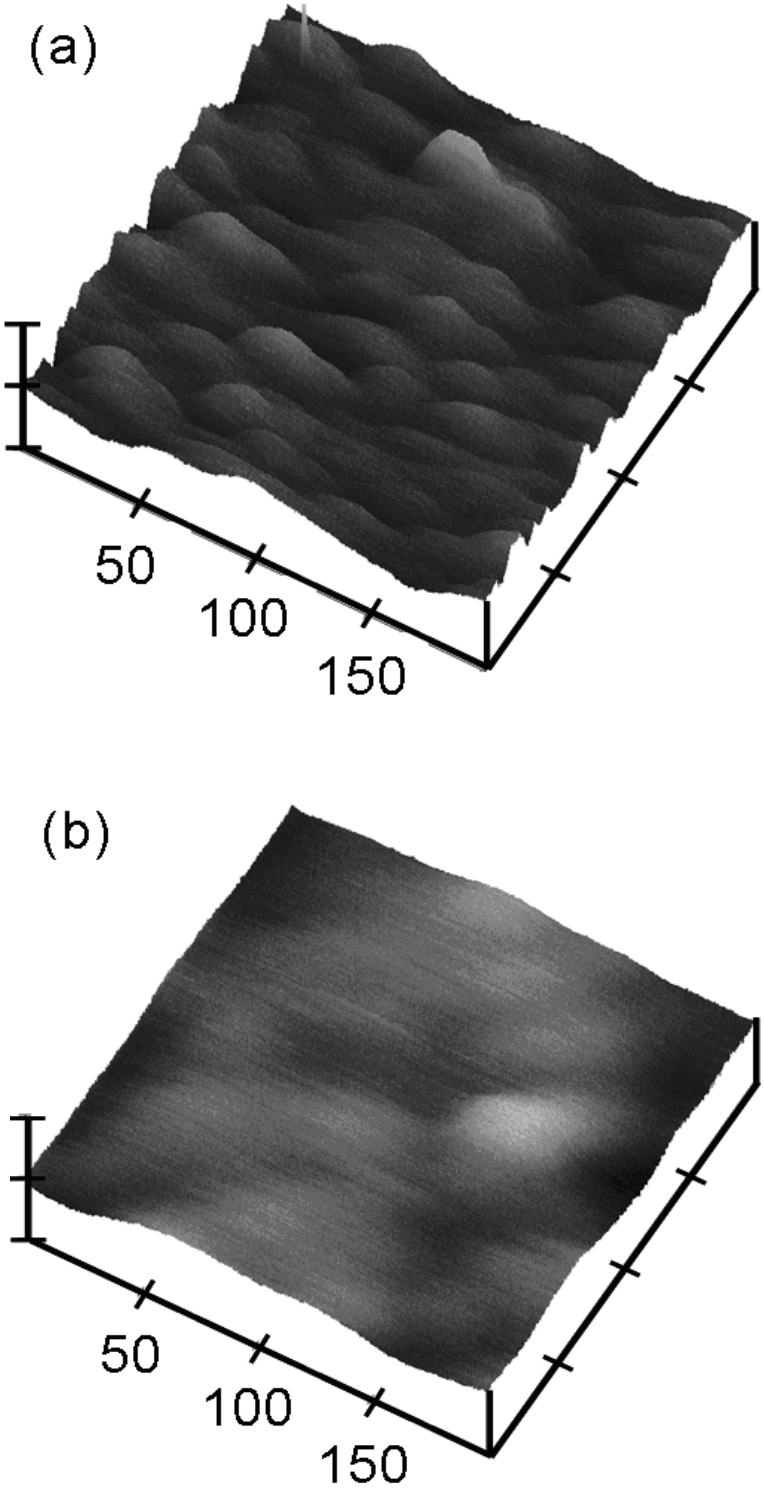

Figure 3-10. *AFM micrographs of the surface of the annealed $La_xZr_{1-x}O_2$ thin films.* (***a***) *x = 0.35;* (***b***) *x = 0.09.*

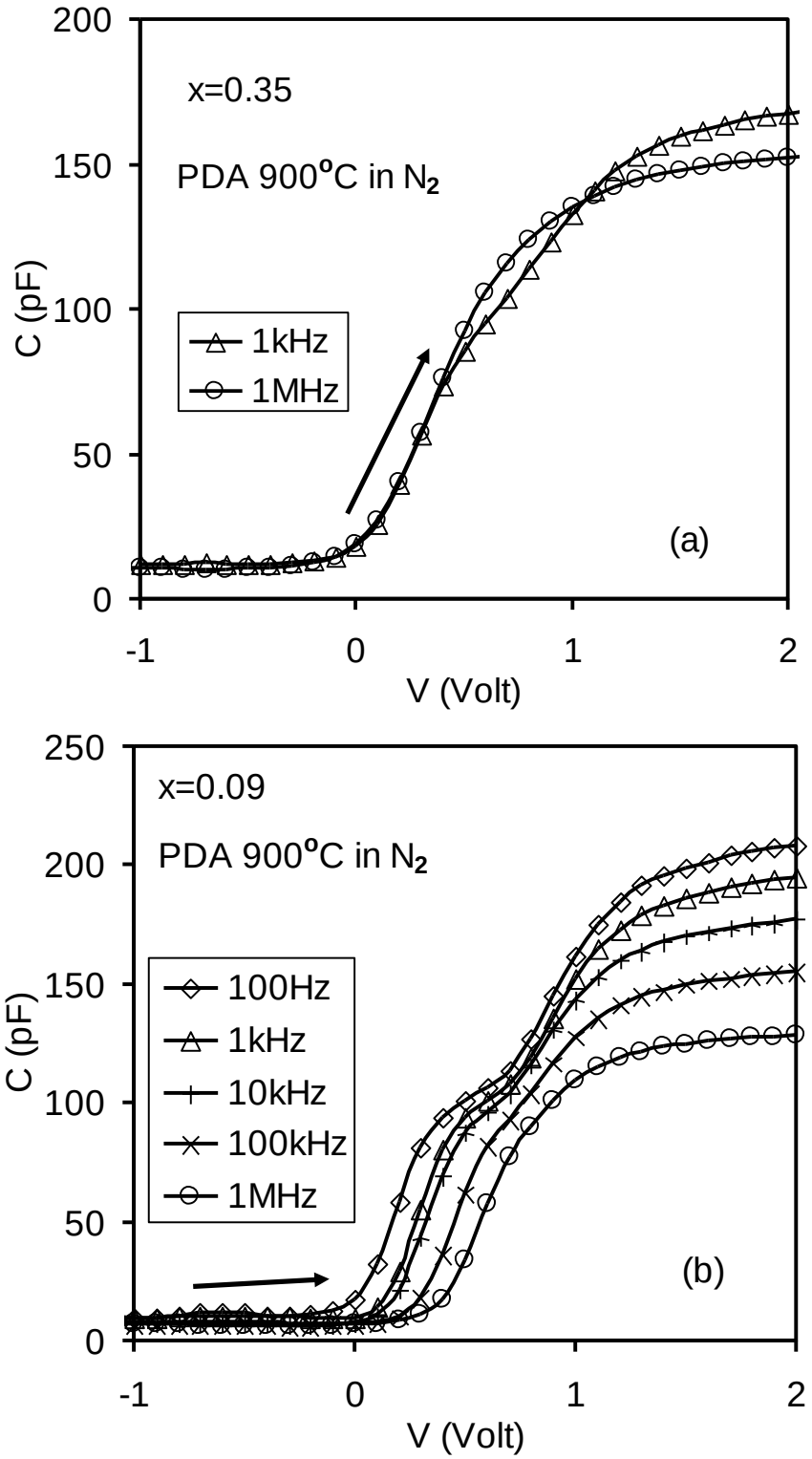

Figure 3-11. *C-V results at different frequencies from the annealed $La_xZr_{1-x}O_{2-\delta}$ samples with back Al contact and an effective substrate area: 6 cm²: (**a**) x = 0.35; (**b**) x = 0.09.*

The Root Mean Square (RMS) roughness of the x = 0.35 thin film is 0.64

nm after annealing as shown in Figure 3-10a. However no significant roughness was observed for the x = 0.09 thin film (RMS roughness of 0.3 nm) shown in Figure 3-10b[14]. It means that the x = 0.35 thin film has a rougher surface than the x = 0.09 thin film. The applied frequency is from 1 kHz to 1 MHz. The annealed thin film with x = 0.09 had large frequency dispersion where the capacitance decreased from 192 pF to 123 pF as the frequency increased from 1 kHz to 1 MHz. However, the annealed thin film with x = 0.35 showed small frequency dispersion where the capacitance decreased from 167 pF to 151 pF and the frequencies changed from 1kHz to 1MHz. Comparing these results from the C-V measurements shown in Figure 3-11, it leads to the conclusion that the surface roughness is not responsible for the observed frequency dispersion of the high-k dielectric thin films in Figure 3-11.

3.4 Other Effects of Frequency Dispersion

There were two further more possible causes of the observed frequency dispersion: polysilicon depletion effect and quantum mechanical confinement. For thinner oxides, the poly depletion effect will become more significant leading to reduced surface potential, channel current, and gate capacitance. Furthermore, poly depletion will affect the extraction of the physical oxide thickness[22-25]. Some analysis and numerical methods for the polysilicon

depletion effect on the MOS device have been proposed[26-27]. The decrease in the gate capacitance caused by polysilicon depletion can be assumed as a result of the increase in the effective gate oxide thickness. There are many surface potential models that can be used to analyze the gate capacitance. These models are solved by the Poisson Equation with boundary conditions to investigate the polysilicon depletion effect[28].

For oxide thicknesses down to 1~3 nm, the quantum mechanical effect should be taken into account[29-31]. There was a difference between the calculated capacitance and the measured capacitance with ultra-thin gate dielectrics. Quantum mechanical confinement would result in the continuous band being quantized into electronic sub-band near the surface. The additional band bending confines the carriers to the narrow surface channel. The electrons redistribute in space due to the confinement effect and the peak of electron density are no longer within the silicon/silicon oxide interface, which would be further away from the surface in MOS devices[32-33]. However since the thickness of the high-*k* layer and the thickness of interfacial layer is greater than 3 nm in the samples under investigation, the quantum mechanical effects were not considered.

References

1. Hirose, M.; Hiroshima, M.; Yasaka, T.; Miyazaki, S. Characterization of silicon surface microroughness and tunneling transport through ultrathin gate oxide. *J. Vac. Sci. Technol*. *A* 1994, *12*, *4*, 1864–1868.
2. Schuegraf, K.F.; King, C.C.; Hu, C. Impact of polysilicon depeletion in thin oxide MOS device. In *VLSI Technology*, June 1992, Seattle, WA; pp. 86–90.
3. Lee, S.-W.; Liang, C.; Pan, C.-S.; Lin, W.; Mark, J.B. A study on the physical mechanism in the recovery of gate capacitance to C_{OX} in implant polysilicon MOS structure. *IEEE Electron Device Lett.* 1992, *13*, *1*, 2–4.
4. Spinelli, A.S.; Pacelli, A.; Lacaita, A.L. An improved formula for the determination of the polysilicon doping. *IEEE Electron Device Lett*. 2001, *22*, *6*, 281–283.
5. Hauser, J.R.; Ahmed, K. Characterization of ultra-thin oxides using electrical C-V and I-V measurements. *AIP Conference Proceedings*, Gaithersburg, Maryland, USA, November 1998; 449, pp. 235–239.
6. Pregaldiny, F.; Lallement, C.; Mathiot, D. Accounting for quantum mechanical effects from accumulation to inversion, in a fully analytical surface potential-based MOSFET model. *Solid State Electron.* 2004, *48*, *5*, 781–787.
7. Sune, J.; Olivo, P.; Ricco, B. Quantum-mechanical modeling of

accumulation layers in MOS structure. *IEEE Trans. Electron Devices* 1992, *39*, *7*, 1732–1739.

8. Pregaldiny, F.; Lallement, C.; van Langevelde, R.; Mathiot, D. An advanced explicit surface potential model physically accounting for the quantization effects in deep-submicron. *Solid-State Electronics* 2004, *48*, *3*, 427–435.
9. Niwa, M.; Kouzaki, T.; Okada, K.; Udagawa, M.; Sinclair, R. Atomic-order planarization of ultrathin SiO_2/Si (001) interfaces. *Jpn. J. Appl. Phys*. 1994, *33*, *1B*, 388–394.
10. Shiau, J.-J.; Fahrenbruch, A.L.; Bube, R.H. Influence of ac contact impedance on high-frequency, low-temperature, or fast-transient junction measurements in semiconductors. *J. Appl. Phys.* 1987, *61*, *4*, 1556–1561.
11. Venkatesan, V.; Das, K.; von-Windheim, J.A.; Geis, M.W. Effect of back contact impedance on frequency dependence of capacitance-voltage measurements on metal/diamond diodes. *Appl. Phys. Lett.* 1993, *63*, *8*, 1065–1067.
12. Lo, S.H.; Buchanan, D.A.; Taur, Y.; Wang, W. Quantum-mechanical modeling of electron tunneling current from the inversion layer of ultra-thin-oxide nMOSFET's. *IEEE Electron Device Lett*. 1997, *18*, *5*, 209–211.
13. Kwa, K.S.K.; Chattopadhyay, S.; Jankovic, N.D.; Olsen, S.H.; Driscoll, L.S.; O'Neill, A.G. A model for capacitance reconstruction from measured lossy MOS capacitance-voltage characteristics. *Semicond. Sci. Technol.* 2003, *18*, *2*, 82–87.

14. Zhao, C.Z.; Taylor, S.; Werner, M.; Chalker, P.R.; Murray, R.T.; Gaskell, J.M.; Jones, A.C. Dielectric relaxation of lanthanum doped zirconium oxide. *J. Appl. Phys.* 2009, *105*, *4*, 044102.

15. Wu, W.H.; Tsui, B.Y.; Huang, Y.P.; Hsieh, F.C.; Chen, M.C.; Hou, Y.T.; Jin, Y.; Tao, H.J.; Chen, S.C.; Liang, M.S. Two-frequency C-V correction using five-element circuit model for high-*k* gate dielectric and ultrathin oxide. *IEEE Electron Device Lett*. 2006, *27*, *5*, 399–401.

16. Lerner, E.J. The end of the road for Moore's law. *IBM J. Res. Develop*. 1999, 6–11.

17. Ahmed, K.; Ibok, E.; Yeap, G.C.-F.; Qi Xiang; Ogle, B.; Wortman, J.J.; Hauser, J.R. Impact of tunnel currents and channel resistance on the characterization of channel inversion layer charge and polysilicon-gate depletion of sub-20-A gate oxide MOSFET's. *IEEE Trans. Electron Devices* 1999, *46*, *8*, 1650–1655.

18. Choi, C.-H.; Jung-Suk Goo; Tae-Young Oh; Zhiping Yu; Dutton, R.W.; Bayoumi, A.; Min Cao; Voorde, P.V.; Vook, D.; Diaz, C.H. MOS C-V characterization of ultrathin gate oxide thickness (1.3-1.8 nm). *IEEE Electron Device Lett*. 1999, *20*, *6*, 292–294.

19. Taechakumput, P.; Zhao, C.Z.; Taylor, S.; Werner, M.; Pham, N.; Chalker, P.R.; Murray, R.T.; Gaskell, J.M.; Aspinall, H.C.; Jones, A.C. Origin of frequency of dispersion in high-*k* dielectrics. In *Proceedings of 7th International Semiconductor Technology Conference ISTC2008*, Pudong.

Shanghai, 2008; pp. 20–26.

20. Yang, K.J.; Chenming, H. MOS capacitance measurements for high-leakage thin dielectrics. *IEEE Trans. Electron Devices* 1999, *46*, *7*, 1500–1501.
21. Zhang, J.L.; Yuan, J.S.; Ma, Y.; Oates, A.S. Modeling of direct tunneling and surface roughness on C-V charateristics of ultra-thin gate MOS capacitors. *Solid State Electron.* 2001, *45*, *2*, 373–377.
22. Arora, N.D.; Rios, R.; Huang, C.L. Modeling the polysilicon depletion effect and its impact on submicrometer CMOS circuit performance. *IEEE Trans. Electron Devices* 1995, *42*, *5*, 935–943.
23. Rios, R.; Arora, N.D.; Huang, C.L. An analytic polysilicon depletion effect model for MOSFET's. *IEEE Electron Device Lett*. 1994, *15*, *4*, 129–131.
24. Gupta, A.; Fang, P.; Song, M.; Lin, M.R.; Wollesen, D.; Chen, K.; Hu, C. Accurate determination of ultrathin gate oxide thickness and effective polysilicon doping of CMOS devices. *IEEE Electron Device Lett.* 1997, *18*, *2*, 580–582.
25. Takeuchi, K.; Kasai, N.; Terada, K. A new effective channel length determination method for LDD MOSFETs. *IEEE 1991 International Conference on Microelectronic Test Structure*, Mar. 18-20 1991; pp. 215–220.
26. Cumberbatch, E.; Abebe, H.; Morris, H.; Tyree, V. Aanalytical surface potential model with polysilicon gate depletion effect for NMOS. In *Proceedings of 2005 Nanotechnology conference*, Anaheim, CA, May 2005; pp. 57–60.

27. Abebe, H.; Cumberbatch, E.; Morris, H.; Tyree, V. Numerical and analytical results for the polysilicon gate depletion effect on MOS gate capacitance. In *Proceedings University Government Industry Micro electronics Symposium*, San Jose, CA, June 2006; pp. 113–117.
28. Lin, W.W. A simple method for extracting average doping concentration in the polysilicon and silicon surface layer near the oxide in polysilicon-gate MOS structures. *IEEE Electron Device Lett*. 1994, *15*, *2*, 51–53.
29. Ohkura, Y. Quantum effects in Si n-MOS inversion layer at high substrate concentration. *Solid State Electron*. 1990, *33*, *12*, 1581–1585.
30. Yeo, Y.C.; Ranade, P.; King, T.J.; Hu, C. Effects of high-*k* gate dielectric materials on metal and silicon gate work function. *IEEE Electron Device Lett*. 2002, *23*, *6*, 342–344.
31. Sue, J.; Olivo, P.; Riccb, B. Quantum-mechanical modeling of accumulation layers in MOS structure. *IEEE Electron Device Lett*. 1992, *39*, *7*, 1732–1739.
32. Moglestue, C. Self-consistent calculation of electron and hole inversion charges at silicon-silicon dioxide interfaces. *J. Appl. Phys*. 1986, *59*, *5*, 3175–3183.
33. Richter, C.A.; Hefner, A.R.; Vogel, E.M. A comparison of quantum-mechanical capacitance- voltage simulators. *IEEE Electron Device Lett.* 2001, *22*, *1*, 35–37.

Chapter 4: Mathematical Models for Dielectric Relaxation

Extrinsic causes of frequency dispersion during C-V measurements in high-*k* materials have been taken into account. After careful considerations of the extrinsic causes for frequency dispersion, high-*k* capacitance C_h was determined. Using the equation below, dielectric constant (*k*) was able to be extracted from the high-*k* capacitance.

$$C_h = \frac{Ak\varepsilon_0}{t_h} \qquad 4\text{-}1$$

where *A* is the area of the MOS capacitor and t_h is the thickness of the high-*k* oxides. Frequency dispersion can now solely be associated with the frequency dependence of the *k*-value in Figure 3-3, Figure 3-11 and Figure 4-1a. The frequency dependence of the *k*-value can be extracted as shown in Figure 4-1b, Figure 4-2 and Figure 4-3. No frequency dependence of *k*-value was observed for the $LaAlO_3/SiO_2$ and ZrO_2/SiO_2 stacks. The frequency dependence of the *k*-value was observed for the $La_xZr_{1-x}O_2/SiO_2$ stacks. Solid lines are from fitting results from the Curie-von Schweidler equation. The details are given below.

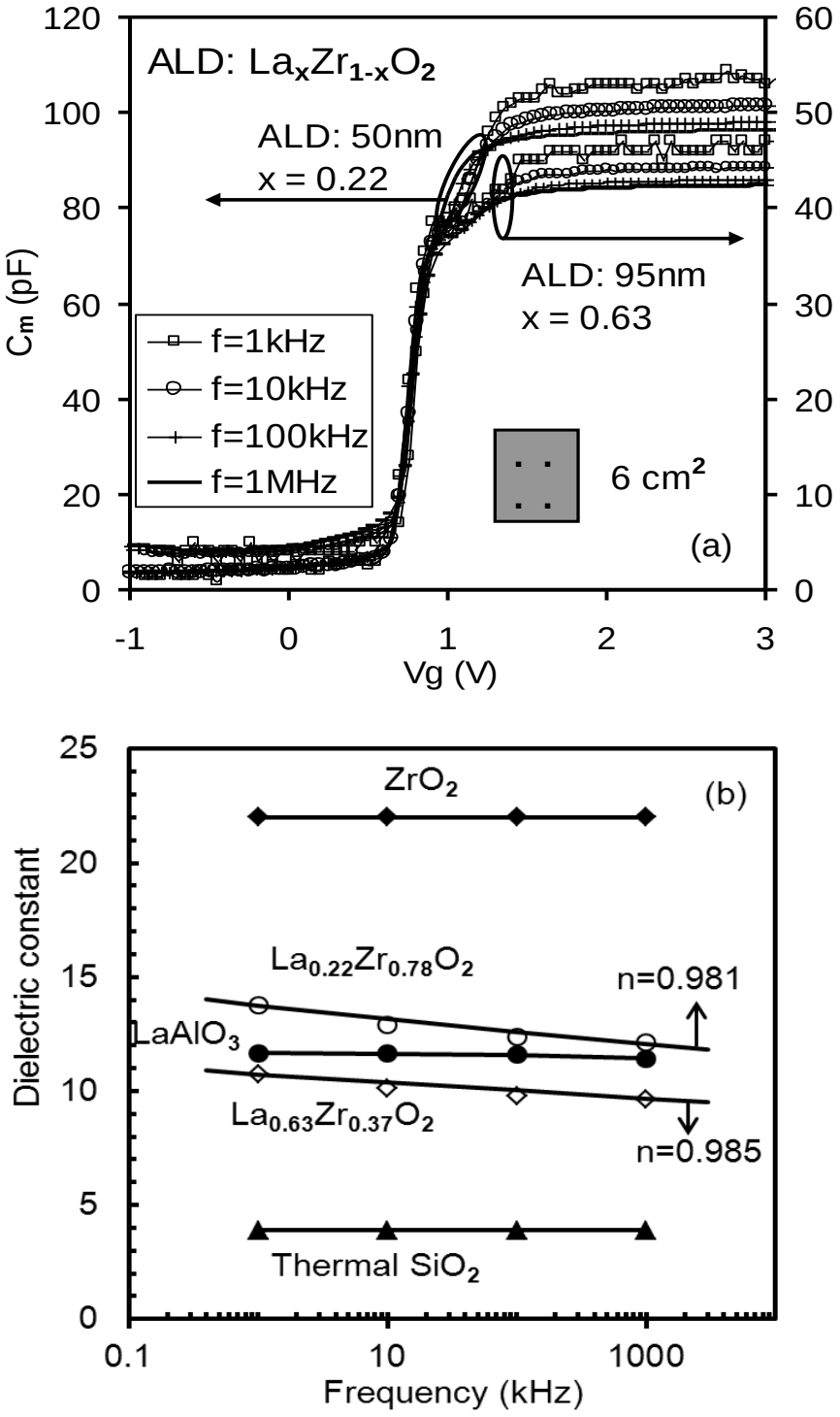

Figure 4-1. *(**a**) Frequency dispersion in C-V measurements observed from $La_xZr_{1-x}O_2$ samples. (**b**) A summary of frequency dependence of k-value extracted from Figure 4-1a, Figure 3-5 (SiO_2), Figure 3-7 ($LaAlO_3$), and Figure 3-8 (ZrO_2).*

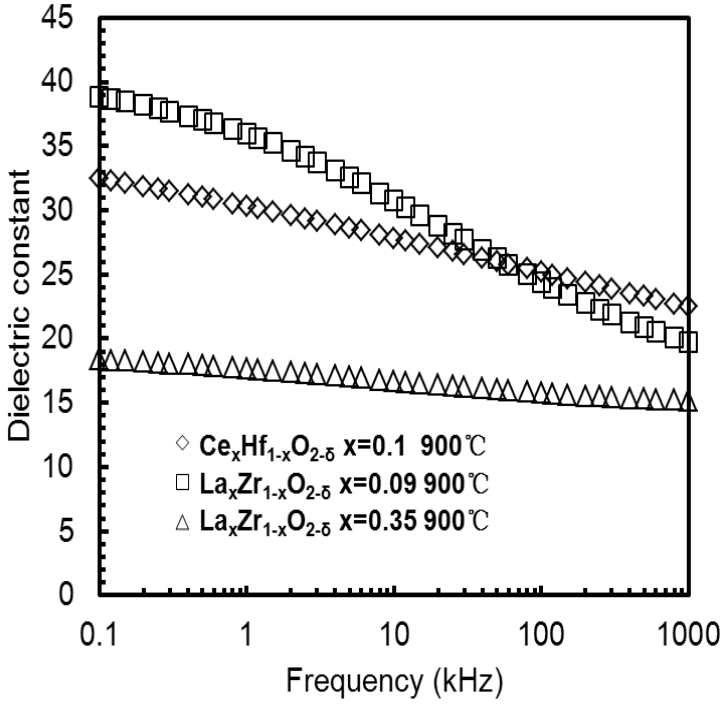

Figure 4-2. *Frequency dependence of the k-value was extracted from C-f measurements of $La_{0.35}Zr_{0.65}O_{2-\delta}$ and $La_{0.09}Zr_{0.91}O_{2-\delta}$ thin films annealed at 900°C, or extracted from Figure 3-11 (a,b).*

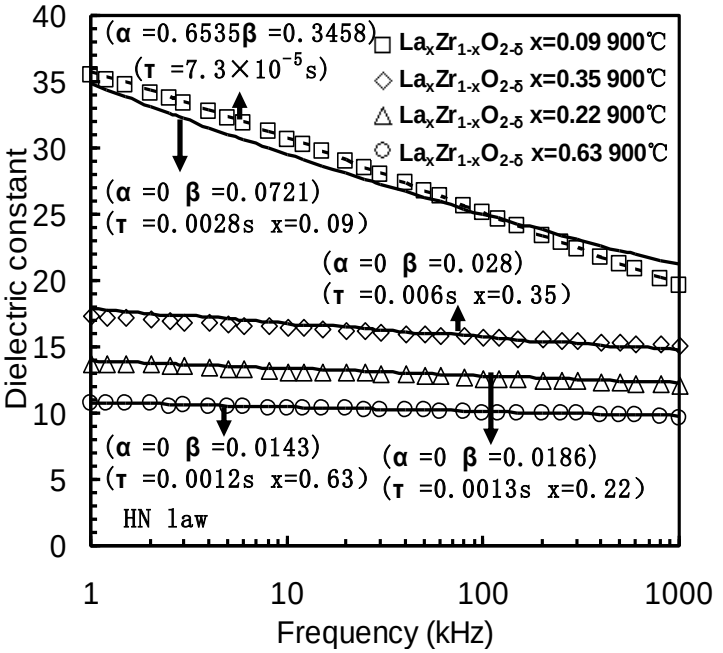

Figure 4-3. *Frequency dependence of the k-value was extracted from C-f measurements observed in four $La_xZr_{1-x}O_{2-\delta}$ thin films.*

C-V data from the annealed thin films ($La_{0.22}Zr_{0.78}O_2$ and $La_{0.63}Zr_{0.37}O_2$) are given in Figure 4-1a. Figure 4-1b showed no frequency dependence of the *k*-value in $LaAlO_3/SiO_2$ and ZrO_2/SiO_2 stacks. However, it was observed in $La_xZr_{1-x}O_2/SiO_2$ stacks. The *k*-values of $La_{0.22}Zr_{0.78}O_2$ and $La_{0.63}Zr_{0.37}O_2$ were observed to decrease from 13.5 and 10.5 to 12 and 9.5 respectively, as the frequency increasing from 1 kHz to 1 MHz. A constant frequency response was observed in thermal SiO_2 shown in Figure 4-1b.

The *k-f* (*k*-value-frequency) data of the $Ce_xHf_{1-x}O_{2-\delta}$, $La_{0.35}Zr_{0.65}O_{2-\delta}$ and $La_{0.09}Zr_{0.91}O_{2-\delta}$ thin films are given in Figure 4-2. Frequency dependence of the $Ce_xHf_{1-x}O_{2-\delta}$ thin film was extracted from Figure 3-3. The experimentally observed dielectric relaxation for $Ce_xHf_{1-x}O_2$ was modeled using the HN relationship. The composition of Ce, x, is 0.10, the relaxation parameter α and the relaxation time τ are 0.75 and 1×10^{-5} s, respectively. The fitted parameters of the dielectric relaxation models for $La_xZr_{1-x}O_2$ were shown in Table 4-1. The zirconia thin film with a lanthanum (La) concentration of x = 0.35 showed that a *k*-value slowly decreased from 18 to 15 as the frequency increased from 100 Hz to 1 MHz. In contrast the lightly doped 9% sample demonstrated a sharp decrease in *k*-value and suffered from a severe dielectric relaxation. A *k*-value of 39 was obtained at 100Hz, but this value was reduced to 19 at 1 MHz. The 10% Ce doped hafnium thin film also had a *k*-value decreasing from 33 at 100 Hz to 21 at 1 MHz. Figure 4-3 summarizes the frequency dependence of *k*-value of four $La_xZr_{1-x}O_2$ thin films from Figures 4-1 and 4-2.

Many dielectric relaxation models were proposed to interpret intrinsic frequency dispersion which is also termed as frequency dependence of *k*-value. The fitted parameters of the dielectric relaxation models for Figure 4-3 are shown in Table 4-1. The squares represent data from the $La_{0.09}Zr_{0.91}O_{2-\delta}$ sample. The diamonds represent data from the $La_{0.35}Zr_{0.65}O_{2-\delta}$ sample. The triangles represent data from the $La_{0.22}Zr_{0.78}O_{2-\delta}$ sample. The circles represent data from the $La_{0.63}Zr_{0.27}O_{2-\delta}$ sample. Solid lines are from fitting results from the Cole-Davidson equation, while the dashed line is from the HN equation. The parameters α, β and τ are parameters from the Cole-Davidson or HN equation. The details of the models are discussed below.

Table 4-1. Fitted parameters of the dielectric relaxation models for Figure 4-3.

Models	**Cole-Cole**		**Cole-Davidson**		**Havriliak-Negami**		
Parameters	α	τ (s)	β	τ (s)	A	β	τ (s)
$La_xZr_{1-x}O_{2-\delta}$ x=0.09	0.75	3.9×10^{-7}	0.0721	0.0028	0.6535	0.3458	7.3×10^{-5}
$La_xZr_{1-x}O_{2-\delta}$ x=0.35	0.866	4.6×10^{-11}	0.028	0.006	0	0.028	0.006
$La_xZr_{1-x}O_{2-\delta}$ x=0.22	0.815	3.8×10^{-11}	0.0186	0.0013	0	0.0186	0.0013
$La_xZr_{1-x}O_{2-\delta}$ x=0.63	0.82	5.2×10^{-12}	0.0143	0.0012	0	0.0143	0.0012

4.1 Curie-von Schweidler and Debye Law

In 1889, Curie-von Schweidler (CS) law was firstly announced and

developed later in 1907[1-2]. The general type of dielectric relaxation in time domain can be described by the CS law (the t^{-n} behavior, $0 \leq n \leq 1$).

$$\frac{dP(t)}{dt} \propto t^{-n} \qquad 4\text{-}2$$

where *P(t)* represents the polarization and the exponent *n* indicates the degree of dielectric relaxation. After a Fourier transform, the complex susceptibility CS relation is:

$$\chi_{CS} = A(i\omega)^{n-1} \qquad 4\text{-}3$$

where *A* and *n* are the relaxation parameters, ε_∞ is the high frequency limit of the permittivity, $\chi_{CS} = [\omega\varepsilon_{CS} - \varepsilon_\infty]/(\varepsilon_s - \varepsilon_\infty)$ is the dielectric susceptibility related to the CS law. The value of the exponent (n) indicated the degree of dielectric relaxation. An $n-1$ value of zero would indicate that the dielectric permittivity was frequency independent.

In 1929, Debye described a model for the response of electric dipoles in an alternating electric field[3]. In time domain, the response of the polarization is:

$$\frac{dP(t)}{dt} = -\frac{P(t)}{\tau} \qquad 4\text{-}4$$

$$P(t) = P_0 exp\left(-\frac{t}{\tau}\right) \qquad 4\text{-}5$$

Unlike the CS law of power law, Debye law was an equation of exponential. As two main branches in the development of dielectric relaxation modeling, CS and Debye are the origins along the evolution beyond doubt. Debye model led to a description for the complex dielectric constant ε^*. However, the change of Debye law was too sharp to describe the response change of the polarization. Therefore, an empirical expression originated from Debye law was proposed by Kohlrausch, Williams and Watts, which is a stretched exponential function, to be referred to later as the Kohlrausch -Williams -Watts (KWW) function widely used to describe the relaxation behavior of glass-forming liquids and other complex systems[4-6]. The detailed information concerning the KWW law will be discussed in the Section 4.3 later. The equivalent of the dielectric response function in time domain is:

$$P(t) = P_0 exp\left[\left(-\frac{t}{\tau}\right)^{\beta_{KWW}}\right] \quad 4\text{-}6$$

After a Fourier transform, the Debye equation in frequency domain and its real and imaginary parts are:

$$\varepsilon^*(\omega) = \varepsilon_\infty + \frac{\varepsilon_S - \varepsilon_\infty}{1+(i\omega\tau)} \quad 4\text{-}7$$

$$\varepsilon'(\omega) = \varepsilon_\infty + \frac{\varepsilon_S - \varepsilon_\infty}{1+\omega^2\tau^2} \quad 4\text{-}8$$

$$\varepsilon''(\omega) = \frac{(\varepsilon_S - \varepsilon_\infty)\omega\tau}{1+\omega^2\tau^2} \quad 4\text{-}9$$

where τ was called the relaxation time which was a function of temperature and it was independent of the time, angular frequency $\omega = 2\pi f$. ε_s was also defined as the zero-frequency limit of the real part, ε', of the complex permittivity. ε_∞ was the dielectric constant at ultra-high frequency. Finally, ε' was the *k*-value.

The Debye theory assumed that the molecules are spherical in shape and dipoles are independent in their response to the alternating field with only one relaxation time. The Debye equation predicates ε' sharply decreases with frequency over a relatively small bandwidth. Generally, the Debye theory of dielectric relaxation is utilized for particular typed polar gases, dilute solutions of polar liquids and polar solids. However, the dipoles for a majority of materials are more likely to be interactive and interdependent in their response to the alternating field. Therefore, very few materials completely are in consistent of the Debye equation with only one relaxation time. The Debye expression cannot interpret the data of polar dielectrics with a distribution of relaxation times (comparing to one relaxation time)[7-8]. For example, Figure 4-2 shows that the intrinsic frequency dispersion of the high-*k* materials ($La_xZr_{1-x}O_2$ and $Ce_xHf_{1-x}O_{2-\delta}$) occurred over a wide frequency range. The data are unable to be fitted with the Debye equation because the high-*k* materials have more than one relaxation time.

4.2 Cole-Cole and Cole-Davidson Law

Since the Debye expression cannot properly predict the behavior of some liquids and solids such as chlorinated diphenyl at −25 °C and cyclohexanone at −70 °C[7], Cole K.S. and Cole R.H. proposed an improved Debye equation, known as the Cole-Cole equation, to interpret data observed on various dielectrics. Among relaxation frequencies Cole-Cole relaxation showed that ε' decreased more slowly with frequency than the Debye relaxation. By observing a large number of materials, they found that when the imaginary part (ε'') was plotted versus ε', a curved arc resulted, whereas a semicircle was predicted by the Debye relation. The Cole-Cole equation can be represented by $\varepsilon^*(\omega)$[7]:

$$\varepsilon^*(\omega) = \varepsilon_\infty + \frac{\varepsilon_s - \varepsilon_\infty}{1+(i\omega\tau)^{1-\alpha}} \qquad 4\text{-}10$$

where τ was relaxation time and α was a constant for a given material, having a value $0 \le \alpha \le 1$. $\alpha = 0$ for Debye relaxation. The real and imaginary parts of the Cole-Cole equation are:

$$\varepsilon'(\omega) = \varepsilon_\infty + (\varepsilon_s - \varepsilon_\infty)\frac{1+(\omega\tau)^{1-\alpha}\sin\left(\frac{1}{2}\alpha\pi\right)}{1+2(\omega\tau)^{1-\alpha}\sin\left(\frac{1}{2}\alpha\pi\right)+(\omega\tau)^{2(1-\alpha)}} \qquad 4\text{-}11$$

$$\varepsilon''(\omega) = (\varepsilon_s - \varepsilon_\infty)\frac{1+(\omega\tau)^{1-\alpha}\cos\left(\frac{1}{2}\alpha\pi\right)}{1+2(\omega\tau)^{1-\alpha}\sin\left(\frac{1}{2}\alpha\pi\right)+(\omega\tau)^{2(1-\alpha)}} \qquad 4\text{-}12$$

The larger the value of α, the larger is the distribution of relaxation times. The Cole-Cole equation can be used to fit the dielectric relaxation results shown in Figure 4-3 of the $La_{0.91}Zr_{0.09}O_2$, $La_{0.22}Zr_{0.78}O_2$, $La_{0.35}Zr_{0.65}O_2$ and $La_{0.63}Zr_{0.37}O_2$ thin films and the fitting parameters are shown in Table 4-1. All of the data are perfectly fitted, but the relaxation time was too small (e.g., 10^{-11}s), as shown in Table 4-1.

Davidson *et al.*[8] proposed the following expression (Cole-Davidson equation) to interpret data observed on propylene glycol and glycerol based on the Debye expression:

$$\varepsilon^*(\omega) = \varepsilon_\infty + \frac{\varepsilon_s - \varepsilon_\infty}{(1+i\omega\tau)^\beta} \qquad 4\text{-}13$$

where τ was the relaxation time and β was a constant for a given material. The smaller the value of β then the larger was the distribution of relaxation times. For angular frequencies $\omega > 1/\tau$, the Cole-Davidson model exhibits an asymmetric broadening of the spectrum towards high frequency. The data of propylene glycol and glycerol can be fitted with the Debye formula in the low frequency region. However, at high frequencies, the Debye formula is no longer suitable for fitting. The data can be properly fitted by the Cole-Davidson formula instead[9]. It was reported as a limiting case to the Debye equation. The real and imaginary parts of the Cole-Davidson equation

are given by:

$$\varepsilon'(\omega) = \varepsilon_\infty + (\varepsilon_s - \varepsilon_\infty)(cos\,\varphi)^\beta\, cos\,\beta\,\varphi \quad 4\text{-}14$$

$$\varepsilon''(\omega) = (\varepsilon_s - \varepsilon_\infty)(cos\,\varphi)^\beta\, sin\,\beta\,\varphi \quad 4\text{-}15$$

$$\varphi = tan^{-1}(\omega\tau) \quad 4\text{-}16$$

The Cole-Davidson equation could also be used to fit the dielectric relaxation results shown in Figure 4-3 and the fitted parameters are shown in Table 4-1. However, the fitting for the $La_{0.91}Zr_{0.09}O_2$ thin films was not acceptable.

The Cole-Cole and Cole-Davidson equations are empirical and could be considered to be the consequence of the existence of a distribution of relaxation times rather than that of the single relaxation time (Debye equation). The physical reason for the distribution of relaxation times in the Cole-Cole and Cole-Davidson empirical equations is not yet clear. The reason for a distribution of relaxation times has been identified in certain particular cases, e.g., the occurrence of protonic resonance (reported by Kliem and Arlt[10]) and the porosity effect (proposed by Cabeza *et al*.[11]).

4.3 Havriliak-Negami Law

In 1966, S. Havriliak and S. J. Negami reported the Havriliak-Negami (HN) equation which combined Cole-Cole and Cole-Davidson equations for twenty one polymers[12-13]. The HN equation[13] is:

$$\varepsilon^*(\omega) = \varepsilon_\infty + \frac{\varepsilon_s - \varepsilon_\infty}{[1+(i\omega\tau)^{1-\alpha}]^\beta} \qquad 4\text{-}17$$

The real and imaginary parts of the HN equation are given by:

$$\varepsilon'(\omega) = \varepsilon_\infty + (\varepsilon_s - \varepsilon_\infty)\frac{cos(\beta\Phi)}{\left[1+2(\omega\tau)^{1-\alpha}\, sin\left(\frac{\pi\alpha}{2}\right)+(\omega\tau)^{2(1-\alpha)}\right]^{\frac{\beta}{2}}} \qquad 4\text{-}18$$

$$\varepsilon''(\omega) = (\varepsilon_s - \varepsilon_\infty)\frac{\sin(\beta\Phi)}{\left[1+2(\omega\tau)^{1-\alpha}\, sin\left(\frac{\pi\alpha}{2}\right)+(\omega\tau)^{2(1-\alpha)}\right]^{\frac{\beta}{2}}} \qquad 4\text{-}19$$

$$\Phi = tan^{-1}\frac{(\omega\tau)^{1-\alpha}\, cos\frac{1}{2}\pi\alpha}{1+(\omega\tau)^{1-\alpha}\, sin\frac{1}{2}\pi\alpha} \qquad 4\text{-}20$$

where α and β are the two adjustable fitting parameters. α is related to the width of the loss peak and β controls the asymmetry of the loss peak[14]. In this model, parameters α and β could both vary between 0 and 1. The Debye dielectric relaxation model with a single relaxation time α = 0 and β = 1, the Cole-Cole model with symmetric distribution of relaxation times follows for β = 1 and $0 \leq \alpha \leq 1$, and the Cole-Davidson model with an asymmetric distribution of relaxation times follows for α = 0 and $0 \leq \beta \leq 1$. The HN equation had two distribution parameters α and β but Cole-Cole and Cole-Davidson equations had only one.

This relaxation function had two intriguing features associated with it. First, and most importantly, it represented the experimental quantities almost within their fitting range. Secondly, this function could be considered as a generalized way of writing the two well documented dispersion functions of Cole[8]. Hartmann *et al.*[14] have shown that the five parameters HN model used in the frequency domain can accurately describe the dynamic mechanical behavior of polymers, including the height, width, position, and shape of the loss peak.

The HN equation can be used to fit the dielectric relaxation of the four $La_{0.91}Zr_{0.09}O_2$, $La_{0.22}Zr_{0.78}O_2$, $La_{0.35}Zr_{0.65}O_2$ and $La_{0.63}Zr_{0.37}O_2$ thin films more accurately than the Cole-Cole and Cole-Davidson equations which have only one distribution parameter. The fitting curves are shown in Figure 4-3. The fitting parameters of the $La_xZr_{1-x}O_2$ (x = 0.09, 0.22, 0.35 and 0.63) dielectrics are provided in Table 4-1.

From Table 4-1 and Figure 4-3, the fitting results of the Cole-Davidson equation showed that the asymmetry of the dielectric loss peak, β, increases with decreasing concentration, x, of La. To best fit the x = 0.09 sample, the width change of the loss peak α should be taken into account and, therefore, the HN Equation should be used, where α = 0.6535, β = 0.3458 and τ = 7.3 × 10^{-5} s.

4.4 Kohlrausch-Williams-Watts Law

To fit the data in time domain, an empirical expression was proposed by Kohlrausch, Williams and Watts, which is a stretched exponential function[15], $e^{-\frac{t}{\tau_K}^{\beta_K}}$, to be referred to later as the Kohlrausch-Williams-Watts (KWW) function. The equivalent of the dielectric response function is:

$$f(t) = \frac{d\Phi}{dt} \qquad 4\text{-}21$$

$$\Phi(t) = e^{-\frac{t}{\tau_K}^{\beta_K}} \qquad 4\text{-}22$$

where the τ_K is the characteristic relaxation time, β_K is a stretching parameter, whose magnitude could vary from 0 to 1. For β_K = 1 the Debye process is obtained. In order to analyze the KWW law in the frequency domain, a Fourier transform is needed. The KWW function in the frequency domain[15] is:

$$\varepsilon^*(\omega) = \varepsilon_\infty + (\varepsilon_s - \varepsilon_\infty)\int_0^\infty \beta\tau^{-\beta_K} t^{\beta_K - 1} e^{-\frac{t}{\tau}^{\beta_K} - i\omega t} dt \qquad 4\text{-}23$$

The KWW law has been widely used to describe the relaxation behavior of glass-forming liquids and other complex systems[16]. The KWW law is not simply an empirical expression, but has a profound theoretical significance. Ngai *et al.* [17–20] developed a coupling model and derived the Kohlrausch function theoretically. It has already been pointed out by Yoshihara and

Work[21] from their careful dielectric measurements that the HN equation can describe the complex permittivity of poly more precisely than the KWW function because the HN equation has two distribution parameters α and β[22]. However, a possible relationship between α, β and β_K was hinted at by the results in Reference[23–25], where the following analytical relations could be derived:

$$\beta_K = [(1-\alpha)\beta]^{\frac{1}{1.23}} \qquad 4\text{-}24$$

For characteristic relaxation times, the relationship between τ (the relaxation time of the HN equation) and τ_k is

$$ln\left(\frac{\tau}{\tau_K}\right) = 2.6 \times (1-\beta_K)^{0.5}\, e^{-3\beta_K} \qquad 4\text{-}25$$

where α and β are the distribution parameters of the HN equation and β_K is the distribution parameter of the KWW equation. For the shape parameters, there is a direct transformation from the HN parameters into the KWW parameters. It is well known that a Fourier transform is needed to analyze the KWW law in the frequency domain. However, there is no analytic expression for the Fourier transform of the KWW function in the frequency domain. A Fourier transform of the KWW function in the frequency domain can be approximated by a HN function which has a more complex relaxation form,

but not vice versa[26].

Since KWW model does not hold the analytical expression due to the difficult to integral nature in the equation, computation of Fourier transform poses numerical problems originating from cutoff effects which yield unwanted oscillations, especially when treating real data. A novel model is proposed here to simplify the original KWW model which has an analytical expression in both high and low frequency-domain.

In the remainder of the part, we elaborate on the following themes. Figure 4-4 above showed the comparison between the Cole-Cole plot for CD model and the original KWW model with different value of the external parameter. The horizontal axes (dielectric permittivity) have been normalized as the maximum permittivity value equals to one. The value of $\tau\omega$ has been chosen from 10^{-5} to 10^{5}. The differences between these two models can be neglected in both high frequency region and low frequency region. In the following part, the slope of these curves was used to find the relationship between these two models. Then the simplified KWW model was proposed and a critical comparison was made between the simplified one and the original one.

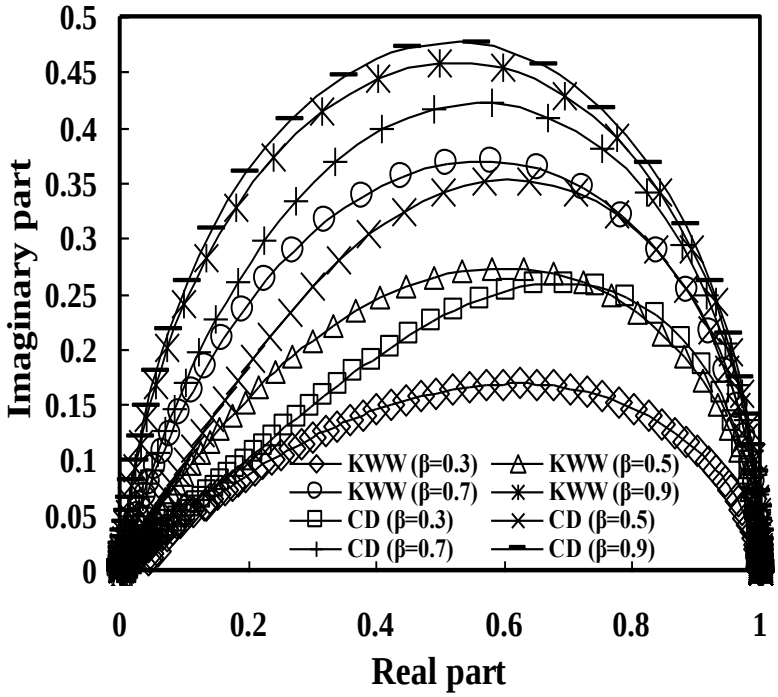

Figure 4-4. *Cole-Cole plot for CD function and KWW function for β=0.3, 0.5, 0.7 and 0.9 when $\tau\omega$ changes from 10^{-5} to 10^{5} as labeled.*

The empirical decay function for KWW model was given as: $\varphi_{KWW}(t) = e^{[-(\frac{t}{\tau_{KWW}})^{\beta_{KWW}}]}$.

The complex permittivity $\varepsilon^*(\omega) = \varepsilon'(\omega) - j\varepsilon''(\omega)$ can be expressed by the Kremers-Kroning relation:

$$\varepsilon^*(\omega) = \varepsilon_\infty + (\varepsilon_S - \varepsilon_\infty)\int_0^\infty \left[-\frac{d\varphi_{KWW}(t)}{dt}\right] \times e^{-j\omega t}dt \qquad 4\text{-}26$$

where ε_s is the static dielectric constant, ε_∞ is the dielectric constant with very high frequency, and ω is the angular frequency.

The decay function was inserted into equation 4-26 and the integration

was used. Given s = $a + j\omega$ and $z = st$, ($a \rightarrow 0^+$) the path of the integration can be changed from the real axis to the imaginary axis. The Maclaurin series was used for simplification. Then an infinite integral of an infinite series was obtained:

$$\frac{\varepsilon^*(\omega)-\varepsilon_\infty}{\varepsilon_0-\varepsilon_\infty} = 1 - lim_{a\rightarrow 0^+} \frac{j\omega}{s} \int_0^\infty e^{-z} \times \sum_{n=0}^\infty \frac{\left[-(\frac{z}{s\tau_{KWW}})^{\beta_{KWW}}\right]^n}{n!} dz \qquad 4\text{-}27$$

It was possible to prove that the integral and summation signs of equation 4-27 can be exchanged. Then the series expansion was obtained:

$$\frac{\varepsilon^*(\omega)-\varepsilon_\infty}{\varepsilon_0-\varepsilon_\infty} = 1 - \sum_{n=0}^\infty \frac{(-1)^n}{(j\omega\tau_{KWW})^{n\beta_{KWW}} n!} \Gamma(1+n\beta_{KWW}) \quad 4\text{-}28$$

When τ_{KWW} >>1, the real part ε' of equation 4-28 can be simplified as:

$$\varepsilon''(\omega) \approx \frac{cos(\frac{\beta_{KWW}\pi}{2})\Gamma(1+\beta_{KWW})}{(\omega\tau_{KWW})^{\beta_{KWW}}} \qquad 4\text{-}29$$

The imaginary part ε'' of equation 4-28 can be simplified as:

$$\varepsilon''(\omega) \approx \frac{sin(\frac{\beta_{KWW}\pi}{2})\Gamma(1+\beta_{KWW})}{(\omega\tau_{KWW})^{\beta_{KWW}}} \qquad 4\text{-}30$$

Then the slope of Cole-Cole plot for KWW model in high frequency region can be simplified as:

$$\frac{\varepsilon''(\omega)}{\varepsilon'(\omega)} \approx tan(\frac{\beta_{KWW}\pi}{2}) \qquad 4\text{-}31$$

However, for τ_{KWW}<<1, equation 4-28 has a slow convergence and it can not be simplified. The asymptotic expansion for small τ_{KWW} was introduced:

$$1 + \sum_{n=0}^{\infty} \frac{(-j\omega\tau_{KWW})^{n+1}}{n!} \frac{1}{\beta_{KWW}} \Gamma(\frac{n+1}{\beta_{KWW}}) \qquad 4\text{-}32$$

For β_{KWW}<1, the series 4-32 constitute the asymptotic expansion for equation 4-26.

The second part of the series was chosen as the first neglected term which is:

$$(-j\omega\tau_{KWW})^2 \frac{1}{\beta_{KWW}} \Gamma(\frac{2}{\beta_{KWW}}) \qquad 4\text{-}33$$

When τ_{KWW}<10^{-3} s and β_{KWW}≥0.3, the real part of the series can be simplified as:

$$\varepsilon'(\omega) = 1 - \frac{(\omega\tau_{KWW})^2}{C\beta_{KWW}} \Gamma(\frac{2}{\beta_{KWW}}) \qquad 4\text{-}34$$

where *C* is a constant bigger than one. The imaginary part can be simplified as:

$$\varepsilon''(\omega) \approx \frac{\omega\tau_{KWW}}{\beta_{KWW}}\Gamma(\frac{1}{\beta_{KWW}}) \qquad 4\text{-}35$$

The slope of Cole-Cole plot for KWW model in low frequency region can be shown as:

$$\frac{\varepsilon''(\omega)}{\varepsilon'(\omega)-1} = -\frac{1}{\omega\tau_{KWW}}\frac{\Gamma(\frac{1}{\beta_{KWW}})}{C\times\Gamma(\frac{2}{\beta_{KWW}})} \approx -tan(\frac{\pi}{2}) \qquad 4\text{-}36$$

After using several frequency-domain spectroscopies, it was empirically found that the following expression was a good fit to the data which was known as the Cole-Davison function:

$$\frac{\varepsilon^*(\omega)-\varepsilon_\infty}{\varepsilon_0-\varepsilon_\infty} = \frac{1}{(1+j\omega\tau_{CD})^{\beta_{CD}}} \qquad 4\text{-}37$$

where β_{CD} is a parameter between zero and one. The real part ε' and imaginary part ε'' can be got and shown as:

$$\varepsilon'(\omega) = (cos\,\varphi)^{\beta_{CD}}\,cos(\beta_{CD}\varphi) \qquad 4\text{-}38$$

$$\varepsilon'(\omega) = (cos\,\varphi)^{\beta_{CD}}\,sin(\beta_{CD}\varphi) \qquad 4\text{-}39$$

$$\varphi = tan^{-1}\,\omega\tau_{CD} \qquad 4\text{-}40$$

Then the slope of Cole-Cole plot for CD model in high frequency region

can be simplified as:

$$\frac{\varepsilon''(\omega)}{\varepsilon'(\omega)} = tan(\beta_{CD}\varphi) \approx tan(\frac{\beta_{CD}\varphi}{2}) \qquad 4\text{-}41$$

For low frequency:

$$\frac{\varepsilon''(\omega)}{\varepsilon'(\omega)-1} = \frac{(cos\,\varphi)^{\beta_{CD}}\, sin(\beta_{CD}\varphi)}{(cos\,\varphi)^{\beta_{CD}}\, cos(\beta_{CD}\varphi)-1} \approx \frac{\beta_{CD}\varphi}{1-\frac{(\beta_{CD}\varphi)^2}{2}-1} \approx -tan(\frac{\pi}{2}) \qquad 4\text{-}42$$

Based on the equation 4-31, equation 4-36, equation 4-41 and equation 42, the KWW model and CD model can have the similar results for both high frequency region and low frequency region if the following equation is satisfied: $tan\frac{\beta_{KWW}\pi}{2} = tan\frac{\beta_{CD}\pi}{2}$. From the comparison above, it obviously means: $\beta_{CD} = \beta_{KWW}$.

Figure 4-5 compared the real part of the original KWW equation and the simplified equation 4-29 in high frequency-domain for β=0.3, 0.5, 0.7 and 0.9. The vertical axes have been normalized to make the maximum value to one. HFA represents High Frequency Approximation for short. It was clearly presented that the simplified model (β=0.3, 0.5 and 0.7) coincided with the original one comprehensively in the high frequency domain ($0<\lg(\omega\tau)<3$). For the simplified model with β=0.9, the curve fitted excellently with the original model. However, some margins of error were observed in the frequency domain ($0<\lg(\omega\tau)<1$). Nevertheless, for high-k materials, normally, the

dielectric relaxation phenomenon was not obvious which meant the value of β is close to zero. It meant that the simplified models were able to fully be suitable for high-*k* materials in high frequency range.

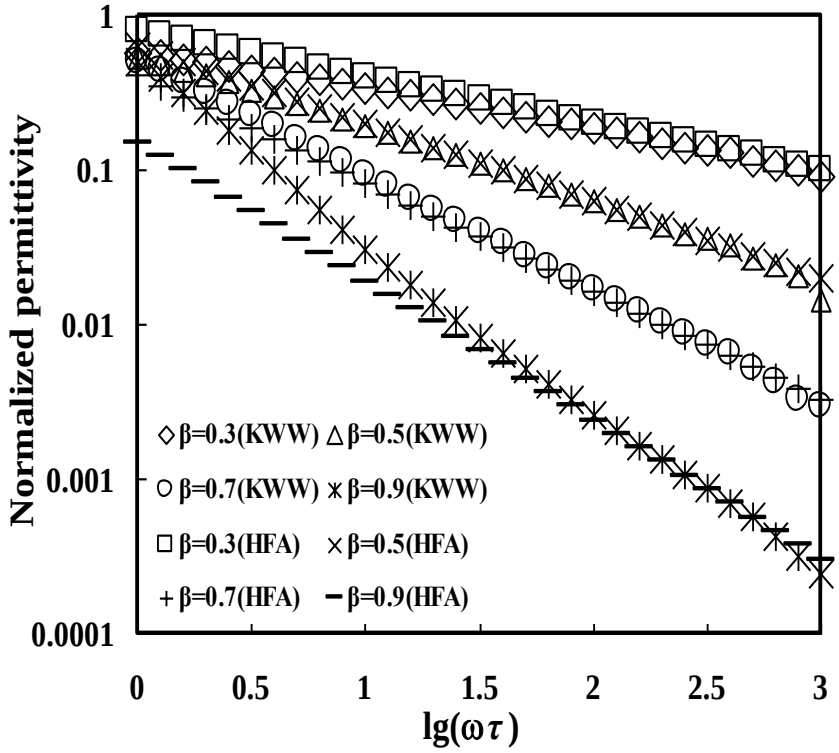

Figure 4-5. *Linear-log plot for the real part of the original KWW function and simplified KWW function with β=0.3, 0.5, 0.7 and 0.9 when ωτ changes from 1 to 1000 as labeled.*

Figure 4-6 compares the real part of the original KWW equation and the simplified equation (7) in low frequency region as β=0.3, 0.5, 0.7 and 0.9. *C*=1 at the same time. The vertical axes have been normalized to make the maximum value to be one. LFA stands for Low Frequency Approximation. It

was clear that for LFA, the changes of the boundary of suitable region were obvious. As the value of β increased, the suitable regions increased as well. For the different values of β, the boundary of suitable region in HFA changed very small unless β was very close to one.

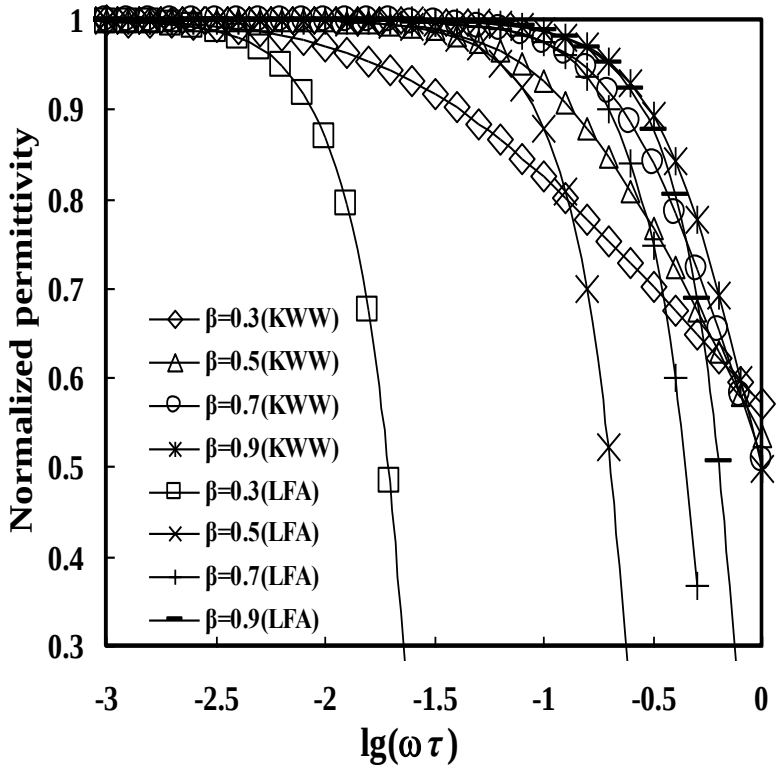

F*igure 4-6.* *Linear-linear plot for the real part of the original KWW function and simplified KWW function with β=0.3, 0.5, 0.7 and 0.9 when ωτ changes from 0.001 to 1 as labeled.*

For high-*k* materials, as mentioned above, the value of β (KWW and CD) for dielectric relaxation was very close to zero. This brought a challenge for the original KWW equation. When using the original one to fit the dielectric

constant versus frequency data, it surely took a long time to accomplish with unwanted oscillations from cutoff effects. The simplified KWW model, Equation 4-29 offered a convenient solution for the fitting issue. Furthermore, a comparison was made between the simplified KWW model and the original one. The simplified model was shown to fit the dielectric relaxation data of high-*k* materials to a high degree of accuracy and it was almost fitted equally excellent with CD model does.

4.5 Final Fitting of Frequency Domain Response

A theoretical description of the slow relaxation in complex condensed systems is still a topic of active research despite the great effort made in recent years. There exist two alternative approaches to the interpretation of dielectric relaxation: the parallel and series models[27]. The parallel model represents the classical relaxation of a large assembly of individual relaxing entities such as dipoles, each of which relaxes with an exponential probability in time but has a different relaxation time. The total relaxation process corresponds to a summation over the available modes, given a frequency domain response function, which can be approximated by the HN relationship.

The alternative approach is the series model, which can be used to describe briefly the origins of the CS law. Consider a system divided into two

interacting sub-systems. The first of these responds rapidly to a stimulus generating a change in the interaction which, in turn, causes a much slower response of the second sub-system. The state of the total system then corresponds to the excited first system together with the un-responded second system and can be considered as a transient or meta-stable state, which slowly decays as the second system responds.

In some complex condensed systems, neither the parallel nor the series approach is accepted. For the final fitting of the frequency domain response, the frequency dependence of complex permittivity $\varepsilon^*(\omega)$ can be expressed by combining the CS law and the modified Debye law (HN or KWW law)[28]:

$$\varepsilon^*(\omega) = \varepsilon_\infty + \chi^*_{CS}(\omega) + \chi^*_{HN}(\omega) - \frac{i\sigma_{DC}}{\omega\varepsilon_S} \qquad 4\text{-}43(a)$$

$$\varepsilon^*(\omega) = \varepsilon_\infty + \chi^*_{CS}(\omega) + \chi^*_{KWW}(\omega) - \frac{i\sigma_{DC}}{\omega\varepsilon_S} \qquad 4\text{-}43(b)$$

$$\chi^*_{CS}(\omega) = A(i\omega)^{n-1} \qquad 4\text{-}44$$

$$\chi^*_{HN}(\omega) = \frac{\varepsilon_S - \varepsilon_\infty}{[1+(i\omega\tau)^{1-\alpha}]^\beta} \qquad 4\text{-}45(a)$$

$$\chi^*_{KWW}(\omega) = (\varepsilon_s - \varepsilon_\infty)\int_0^\infty \beta\tau^{-\beta_K} t^{\beta_K - 1} e^{-\frac{t}{\tau}^{\beta_K} - i\omega t} dt \qquad 4\text{-}45(b)$$

where ε_∞ was the high frequency limit of permittivity, ε_s is the permittivity of free space, σ_{DC} is the DC conductivity. The parameters in the equation are in form of physical meanings (activation energy: E_A):

$$\tau = \tau_0 exp\left[-\frac{E_{A,\tau}}{k(T-T_\tau)}\right] \qquad 4\text{-}46$$

$$\sigma_{DC} = \sigma_0 exp\left[-\frac{E_{A,\sigma}}{k(T-T_\sigma)}\right] \quad 4\text{-}47$$

$$\alpha = \alpha_0 exp\left[-\frac{E_{A,\alpha}}{k(T-T_\alpha)}\right] \quad 4\text{-}48$$

$$\beta = \beta_0 exp\left[-\frac{E_{A,\beta}}{k(T-T_\beta)}\right] \quad 4\text{-}49$$

$$n = n_0 exp\left[-\frac{E_{A,n}}{k(T-T_n)}\right] \quad 4\text{-}50$$

HN law was a modified Debye equation via evolution. Thus, CS and HN law in time domain represented the original power-law and exponential dependence respectively. Most of dielectric relaxation data were able to be modeled by the final fitting law: the combined CS+HN laws.

Based on the discussion above, the dielectric relaxation results of $La_{0.35}Zr_{0.65}O_2$ for as-deposited and PDA samples (shown in Fig. 4-7) have been modeled with the CS and HN relationships (see solid lines in Fig. 4-7)[27]. Significant dielectric relaxation was observed in the air-annealed sample. Solid lines are the fitting results using CS and HN equations. The relaxation of the as-deposited film obeyed a combined CS+HN laws. After the 900 °C PDA, the relaxation behavior of the N_2-annealed film was dominated by the CS law, whereas the air-annealed film was predominantly modeled by the HN relationship that was accompanied by a sharp drop in the *k*-value.

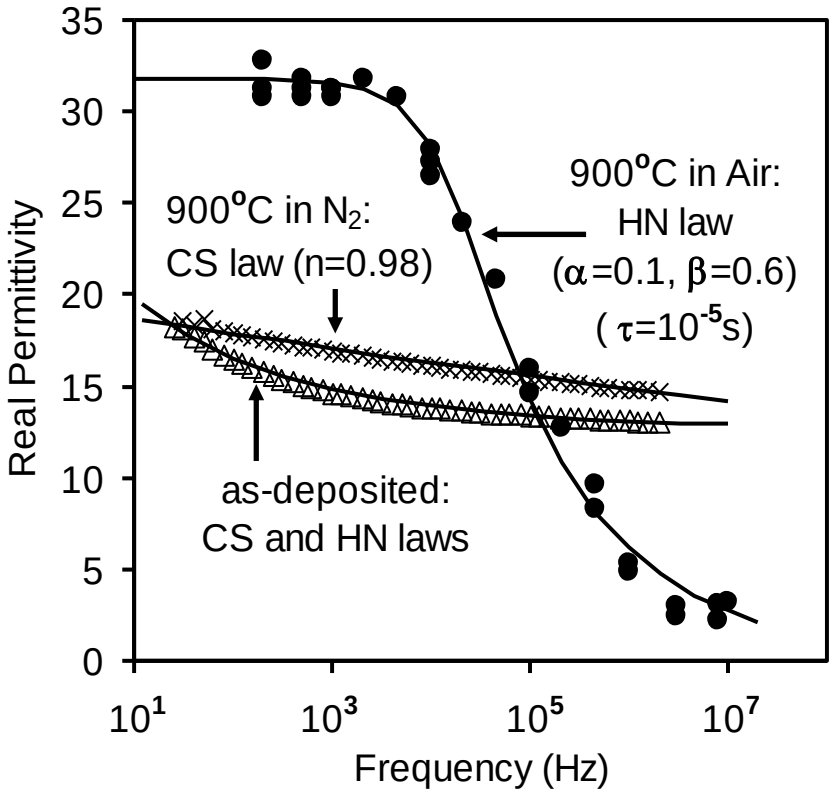

Figure 4-7. *Frequency dependence of k-value of $La_{0.35}Zr_{0.65}O_2$ dielectric for as-deposited and PDA samples.*

The frequency dependent change in the real and imaginary permittivity of $La_2Hf_2O_7$ dielectric for the as-deposited and PDA samples is shown in Fig. 4-8[29]. Two dot-lines and two solid lines are the fitted results using CS and HN laws. Clearly, the PDA process improved the dielectric relaxation and reduced the dielectric loss. The dielectric relaxation of the PDA films was revealed to be dominated by the CS law (n=0.9945, see two dot lines in Fig. 4-8) at $f<3\times10^4$ Hz. However, at $f>3\times10^4$ Hz, the HN law plays an important role (α=0.08, β=0.45, and $\tau=1\times10^{-8}$ s, see two solid lines in Fig. 4-8). The dielectric loss reduces at $f<3\times10^4$ Hz because an increase of the interfacial layer thickness

caused the reduction of the DC conductivity.

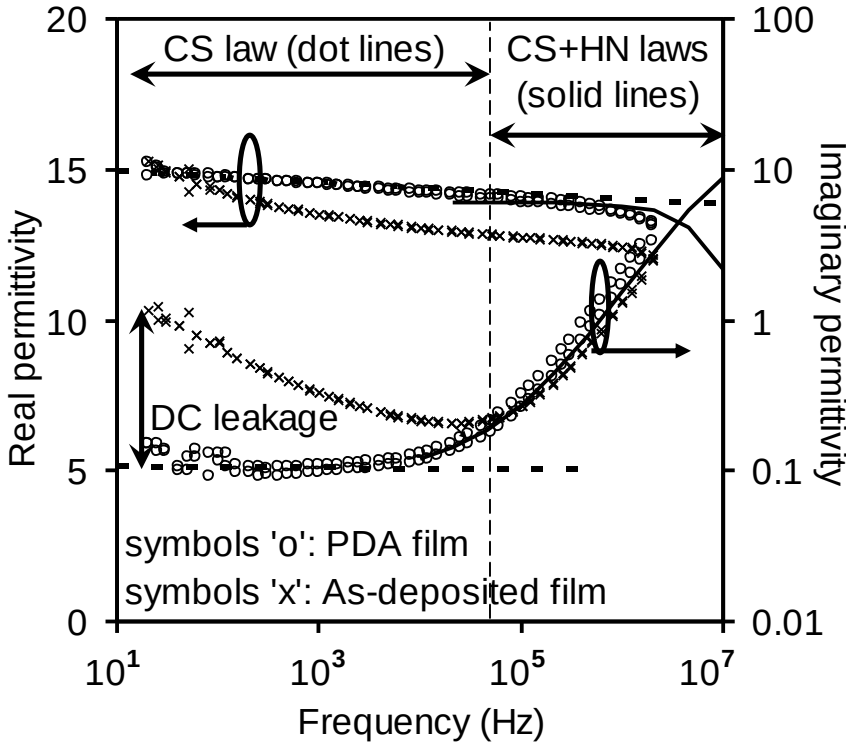

Figure 4-8. *Frequency dependence of the real and imaginary permittivities of $La_2Hf_2O_7$ dielectric for the as-deposited and PDA samples.*

Frequency dependence of the *k*-value was extracted from C-*f* measurements observed in the $La_xZr_{1-x}O_{2-\delta}$ thin films (shown in Fig. 4-3)[30]. Solid lines are from fitting results from the Cole-Davidson equation, while the dashed line is from the HN equation. α, β and τ are parameters from the Cole-Davidson or HN equation. The Cole-Cole and Cole-Davidson equation could fit the dielectric relaxation results of the $La_{0.91}Zr_{0.09}O_2$, $La_{0.22}Zr_{0.78}O_2$, $La_{0.35}Zr_{0.65}O_2$ and $La_{0.63}Zr_{0.37}O_2$ thin films. The $La_xZr_{1-x}O_{2-\delta}$ thin films can be also modeled by the HN equation more accurately than the Cole-Cole and

Cole-Davidson equations.

The dielectric relaxation data in Figure 4-3 were modeled by the CS law or the combined CS+KWW laws, as shown in Figure 4-9. The measured data are the same as Figure 4-3. All solid lines are fitting results from the CS law or the combined CS+KWW laws. β_K, τ_K and n are parameters of the KWW law and CS law. The k-values of the $La_xZr_{1-x}O_2$ (x = 0.22, 0.35 and 0.63) dielectrics clearly show a power-law dependence on frequency known as the CS law, $k \propto f^{n-1}$, $(0 \le n \le 1)$[31-32]. For $La_xZr_{1-x}O_{2-\delta}$ thin films with x = 0.63, x = 0.35 and x = 0.22 La content, the dielectric relaxation response could be fitted by the pure CS law, the n values were 0.981, 0.98 and 0.985 when the composition of La, x, was 0.22, 0.35 and 0.63, respectively.

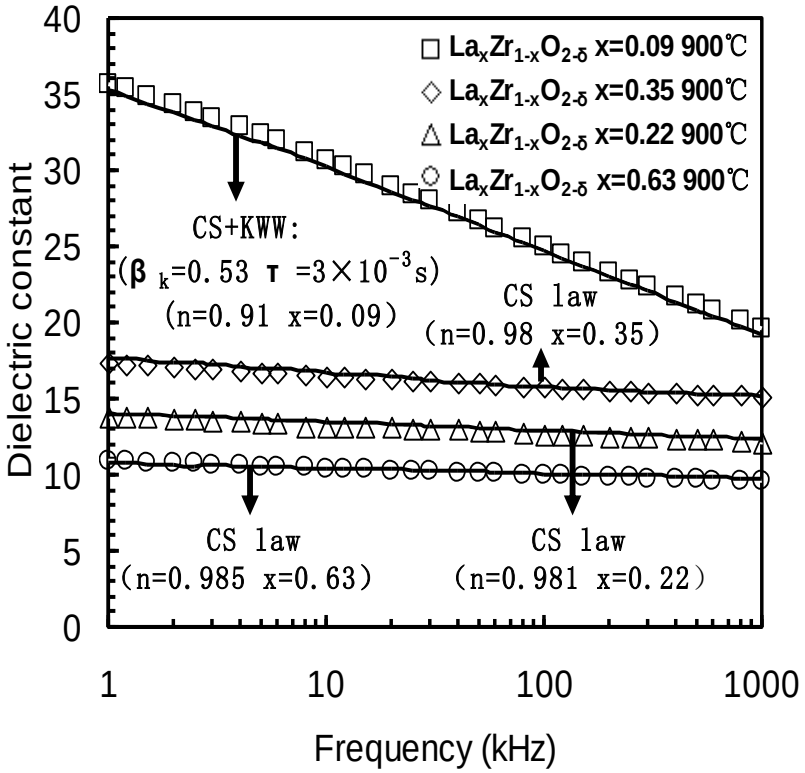

Figure 4-9. *Fitting results from the CS law or the combined CS+KWW laws.*

However, for the x = 0.09 La content, the dielectric relaxation response could not be modeled by the pure CS law or the pure KWW law, but could be modeled by the combined CS+KWW law. The relaxation parameter β_k and n were 0.53 and 0.91, respectively, and the relaxation time τ_K was 3×10^{-3} s, as shown in Figure 4-9. From Figure 4-9, the exponent value n decreased with increasing k-values.

Compared with Figure 4-3, it was found that the combined CS+KWW relaxation process (β_k = 0.53 and n = 0.91) could be substituted by the HN function where α and β were 0.6535 and 0.3458, respectively, in Figure 4-3 because both the HN function and the combined CS+KWW relationship both have two distribution parameters.

References

1. Curie JR: sur le pouvoir inducteur specifique et sur la conductibilite des corps cristallises. *Ann Chim Phys* 1889, 18: 203.
2. Von Schweidler E: Studien uber die anomalien im verhalten der dielektrika. *Ann Phys* 1907, 24: 711–770.
3. Debye P: Polar Molecules; Chemical Catalogue Company 1929: New York, NY, USA.

4. Williams G, Watts DC: Non-symmetrical dielectric relaxation behaviour arising from a simple empirical decay function. *Trans Faraday Soc* 1969, 66: 80–85.
5. Bokov AA, Ye ZG: Double freezing of dielectric response in relaxor $Pb(Mg_{1/3}Nb_{2/3})O_3$ crystals. *Phys. Rev. B* 2006, 74, 13: 132102.
6. Ngai KL, Plazek DJ: A quantitative explanation of the difference in the temperature dependences of the viscoelastic softening and terminal dispersions of linear amorphous polymers. *J Polym Sci Polym Phys* 1986, 24, 3: 619–632.
7. Cole, K.S.; Cole, R.H. Dispersion and absorption in dielectrics. *J. Chem. Phys.* 1941, *9*, 341–351.
8. Davidson, D.W.; Cole, R.H. Dielectric relaxation in glycerol, propylene glycol and n-propanol. *J. Chem. Phys.* 1951, *19*, *12*, 1484–1490.
9. Davidson, D.W.; Cole, R.H. Dielectric relaxation in glycerine. *J. Chem. Phys.* 1950, *18*, 1417.
10. Kliem, H.; Arlt, G. A relation between dielectric distribution functions and structural properties of amorphous matter. *CEIDP Annu. Rep.* 1987, *56*, 325.
11. Kliem, H.; Arlt, G. A relation between dielectric distribution functions and structural properties of amorphous matter. *CEIDP Annu. Rep.* 1987, *56*, 325.
12. Havriliak, S.; Negami, S. A complex plane analysis of α-dispersions in some polymer systems. *J. Polym. Sci. Pt. C* 1966, *14*, *1*, 99–117.
13. Havriliak, S.; Negami, S. A complex plane representation of dielectric

mechanical relaxation processes in some polymers. *Polymer* 1967, *8*, 161–210.

14. Hartmann, B.; Lee, G.F.; Lee, J.D. Loss factor height and width limits for polymer relaxations. *J. Acoust. Soc. Am.* 1994, *95*, *1*, 226–233.
15. Jonscher, A.K. *Dielectric Relaxation in Solids*; Chelsea Dielectric Press: London, NY, USA, 1983.
16. Williams, G.; Watts, D.C. Non-symmetrical dielectric relaxation behaviour arising from a simple empirical decay function. *Trans. Faraday Soc.* 1969, *66*, 80–85.
17. Bokov, A.A.; Ye, Z.-G. Double freezing of dielectric response in relaxor $Pb(Mg_{1/3}Nb_{2/3})O_3$ crystals. *Phys. Rev. B* 2006, *74*, *13*, 132102.
18. Ngai, K.L.; Plazek, D.J. A quantitative explanation of the difference in the temperature dependences of the viscoelastic softening and terminal dispersions of linear amorphous polymers. *J. Polym. Sci. Polym. Phys.* 1986, *24*, *3*, 619–632.
19. Rendell, R.W.; Ngai, K.L.; Rajagopal, A.K. Volume recovery near the glass transition temperature in poly(vinyl acetate): predictions of a coupling model. *Macromolecules.* 1987, *20*, *5*, 1070–1083.
20. Ngai, K.L.; Fytas, G. Interpretation of differences in temperature and pressure dependences of density and concentration fluctuations in amorphous poly(phenylmethyl siloxane). *J. Polym. Sci. Polym. Phys.* 1986, *24*, *8*, 16833–1694.

21. Yoshihara, M.; Work, R.N. Dielectric relaxation in undiluted poly(4-chlorostyrene)2 characteristics of the high-frequency tail. *J. Chem. Phys.* 1981, *74*, *10*, 5872–5876.
22. Shioya, Y.; Mashimo, S. Comparison between interpretations of dielectric behavior of poly (vinyl acetate) by the coupling model and the Havriliak-Negami equation. *J. Chem. Phys.* 1987, *87*, *5*, 3173–3177.
23. Boese, D.; Kremer, F.; Fetters, F.J. Molecular dynamics in bulk cis-polyisoprene as studied by dielectric spectroscopy. *Macromolecules* 1990, *23*, *3*, 829–835.
24. Boese, D.; Momper, B.; Meier, G.; Kremer, F.; Hagenah, J.-U.; Fischer, E.W. Molecular dynamics in poly(methylphenylsiloxane) as studied by dielectric relaxation spectroscopy and quasielastic light scattering. *Macromolecules* 1989, *22*, *12*, 4416–4421.
25. Alvarez, F.; Alegria, A. Relationship between the time-domain Kohlrausch-Williams-Watts and frequency-domain Havriliak-Negami relaxation functions. *J. Colmenero, Phys. Rev. B* 1991, *44*, *14*, 7306–7312.
26. Bokov, A.A.; Kumar, M.M.; Xu, Z.; Ye, Z.-G. Non-arrhenius stretched exponential dielectric relaxation in antiferromagnetic $TiBO_3$ single crystals. *Phys. Rev. B* 2001, *64*, *22*, 224101.
27. Zhao CZ, Werner M, Taylor S, Chalker PR, Jones AC, Zhao C: Dielectric relaxation of La-doped Zirconia caused by annealing ambient. *Nanoscale Research Letters* 2011, 6: 48.

28. Zhao CZ, Taylor S, Werner M, Chalker PR, Murray RT, Gaskell JM, Jones AC: Dielectric relaxation of lanthanum doped zirconium oxide. *Journal of Applied Physics* 2009, 105: 044102.

29. Zhao CZ, Taylor S, Werner M, Chalker PR, Gaskell JM, Jones AC: Frequency dispersion and dielectric relaxation of $La_2Hf_2O_7$. *J. Vac. Sci. Technol. B* 2009, 27, 1: 333.

30. Tao J, Zhao CZ, Zhao C, Taechakumput P, Werner M, Taylor S, Chalker PR: Extrinsic and intrinsic frequency dispersion of high-*k* materials in capacitance-voltage measurements. *Materials* 2012, 5: 1005-1032.

31. Zhao, X.; Vanderbilt, D. First-principles study of structural vibrational and lattice dielectric properties of hafnium oxide. *Phys. Rev. B* 2002, *65*, *23*, 1–4.

32. Wu, W.H.; Tsui, B.Y.; Huang, Y.P.; Hsieh, F.C.; Chen, M.C.; Hou, Y.T.; Jin, Y.; Tao, H.J.; Chen, S.C.; Liang, M.S. Two-frequency C-V correction using five-element circuit model for high-*k* gate dielectric and ultrathin oxide. *IEEE Electron Device Lett*. 2006, *27*, *5*, 399–401.

Chapter 5: Physical Mechanism for Dielectric Relaxation

A dielectric material is a non-conducting substance whose charges are polarized under the influence of an applied electric field. Dielectric behavior must be specified with respect to the time or frequency domain. Different mechanisms show different dynamic behaviors in the time domain. In consequence, adsorption occurs at different windows in the frequency domain.

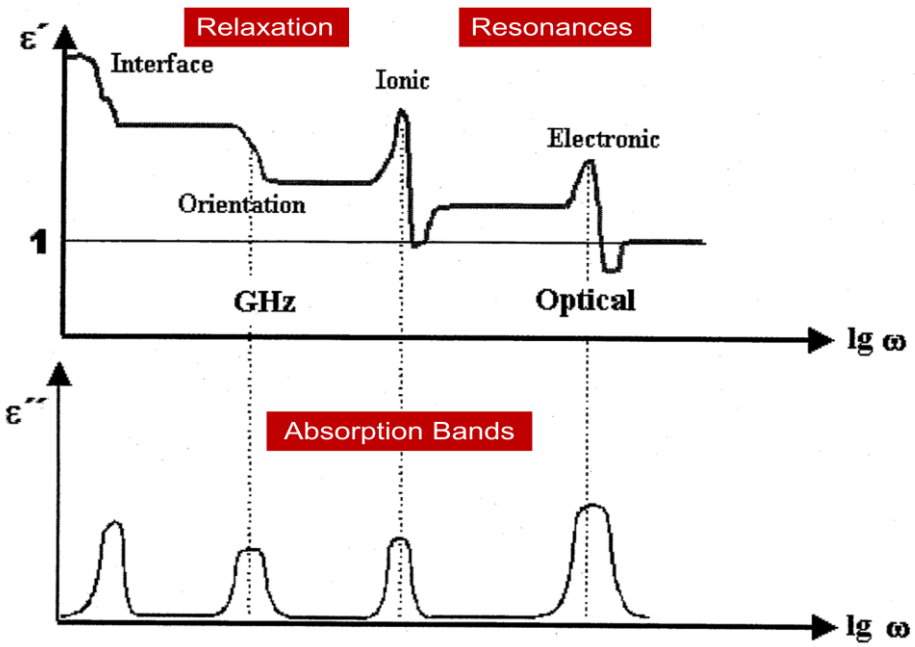

Figure 5-1. *Physical mechanisms of dielectric relaxation in real and imaginary part.*

For the physical mechanism of the dielectric relaxation, Figure 5-1 is to describe the degree of polarization in a given material within frequency domain[1]. The response of the dielectric relaxation in lower frequency range is firstly categorized into the interface polarization. In the region, surfaces, grain boundaries, inter-phase boundaries may be charged, i.e. they contain dipoles which may become oriented to some degree in an external field and thus contribute to the polarization of the material. It is within the orientation polarization as frequency increasing. Here the material must have natural dipoles which can rotate freely. As the frequency increases further, dielectric relaxation is termed as ionic and electronic polarization. Mutual displacement of negative and positive sub-lattice in ionic crystals taken place. In this case a solid material must have some ionic character. Then, it is observed that displacement of electron shell is positioned against positive nucleus. Also, the region is called atomic polarization. In a summary, it is clear that the degree of polarization is related to the structure of the material. Therefore, dielectric behavior in electrostatic and alternating electric fields depends on static and dynamical properties of the structure.

5.1 Lanthanum-doped Zirconium Oxide

X-ray diffraction data is shown in Figure 5-2 from an as-deposited film

and from annealed samples with a La content of x=0, x=0.09, x=0.22 and x=0.35. * denotes monoclinic diffraction peaks from the x=0.09 sample. All as-deposited samples were effectively amorphous and showed no diffraction features. After annealing, XRD data from the un-doped sample (x=0) shows that the film had crystallized, forming a mixed phase of monoclinic, with diffraction peaks at 28.4° (-111), 31.7° (111), 34.2° (002) and 35.4° (200), and a diffraction peak at 30.4° corresponding to either the tetragonal (101) diffraction peak or the cubic (111) peak. The tetragonal or cubic phase cannot be unambiguously distinguished by XRD. In comparison the result from a lightly La doped (x=0.09) film contains a much broader peak centered about 30° corresponding to the tetragonal or cubic phase, with only a small content from the monoclinic phase. The difference in diffraction peak widths from the two films is indicative of their average grain sizes, with the much broader peak from the x=0.09 sample indicative of smaller crystal grains. Two diffraction peaks at 30.0° and 34.6° were observed for the x=0.22 sample and two diffraction peaks at 29.3° and 33.9° were observed for the most heavily doped, x=0.35 annealed film. These are from either the tetragonal or cubic phase, the shifts in peak positions relative to the x=0 and x=0.09 samples arises from the excessively high La contents expanding the lattice. No monoclinic content was observed for either of the two most heavily doped samples. These results show that by increasing the La content the general trend is to suppress the monoclinic phase and stabilize the tetragonal or cubic phase; however the

relationship is not straight forward and the crystal grain size is also affected by the level of doping.

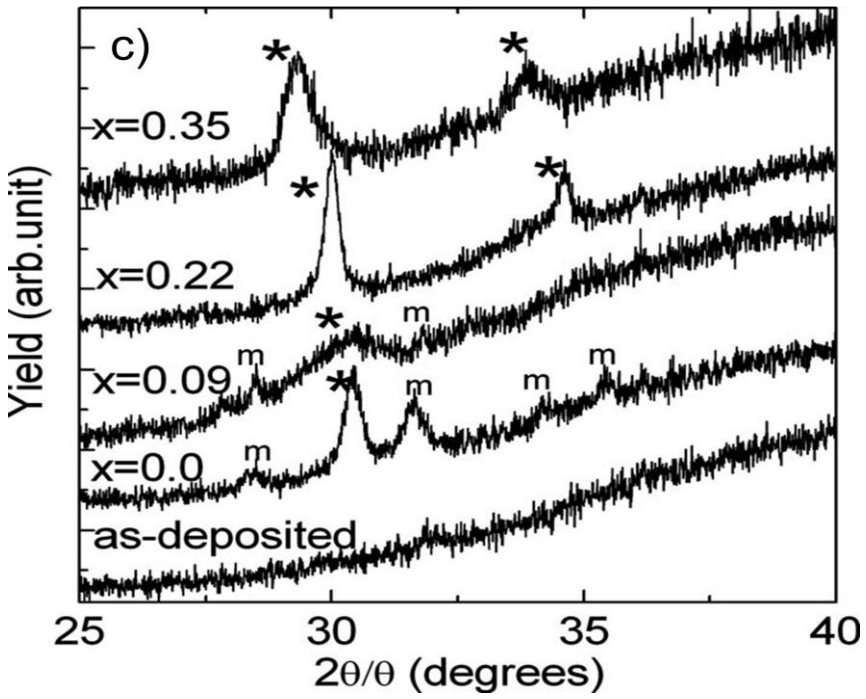

Figure 5-2. *X-ray diffraction data for $La_xZr_{1-x}O_{2-\delta}$ thin films deposited by ALD, as-deposited and following annealing at 900°C in N_2 for 15min.*

XTEM was carried out on both x=0.09 and x=0.35 lanthanum doped zirconium oxide samples. Images[2] from the annealed samples are shown in Figure 5-3a and Figure 5-3b. These images show that equiaxed nanocrystallites of ~4 nm diameter form in the x=0.09 sample, in contrast to a larger ~15 nm diameter crystal for the x=0.35 sample. This trend is also consistent with the average grain size estimated using a Scherrer analysis of the XRD data shown in Figure 5-2, which gives similar values. It appears that varying the doping level changes the phase that the films crystallize into

during annealing, it also affects the size of the crystal grains formed.

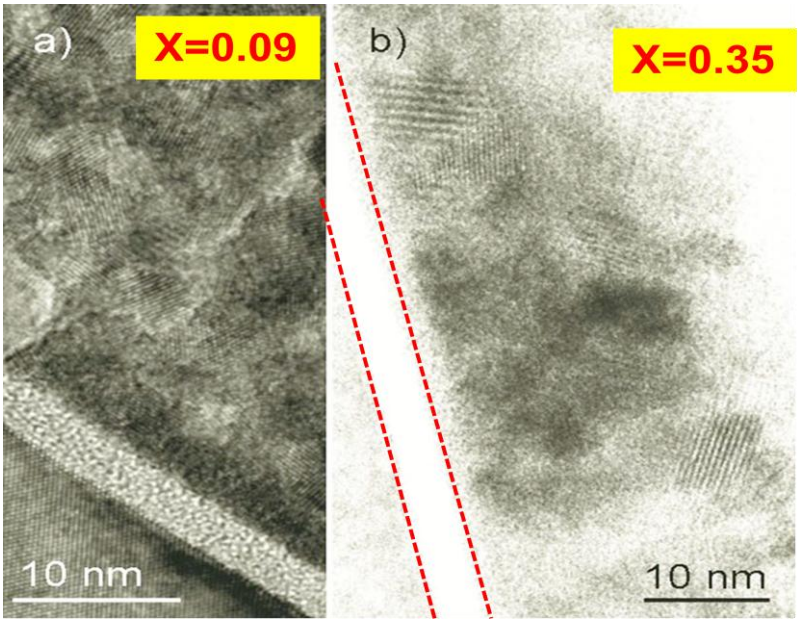

Figure 5-3. *XTEM images from two $La_xZr_{1-x}O_{2-\delta}$ films, which were annealed in N_2 at 900°C for 15min. (a) Small nano-crystallites are formed in the x=0.09 sample (b) with larger crystalline grains formed in the x=0.35 sample.*

The relationship between the extracted *k*-value and test frequency is shown for annealed samples in Figure 5-4, having been extracted from the strong accumulation capacitance at +3V (<+1MV/cm). When the effects in the previous section are accounted for, Figure 5-4 reveals that the frequency dependency of *k*-value is a real material property of the $La_xZr_{1-x}O_{2-\delta}$ dielectric films. The un-doped ZrO_2 film (x=0) has a relatively flat frequency response and a *k*-value of 17 at 50Hz and 16 at 100 kHz. In comparison to the un-doped sample, the sample doped with a La content of x=0.09 has a significant increase of the *k*-value of the dielectric, but also has a large dielectric

relaxation. A *k*-value of 40 is obtained at a frequency of 50Hz, but reduces substantially as the frequency is increased, dropping to 25 at 100 kHz. Nevertheless the doped film always has a higher *k*-value than the un-doped film. The sample with a La content of x=0.22 has a flatter frequency response, but with lower overall values of 22 at 50Hz and 19 at 100 kHz. At a frequency of 2MHz the *k*-values of the x=0.09 and x=0.22 films are almost identical. For the highest doped sample, x=0.35, there is a further reduction in the *k*-values, with only a marginal improvement over the un-doped sample. That is, at a frequency range of 1k to 2MHz, the *k*-values of the x=0.00 and x=0.35 films are almost identical. An inset in the figure illustrates the relationship between the level of doping and the *k*-value. Other studies also show maxima in the region of 10% doping[3-4]. While there is an understanding within the literature that doping can enhance *k*-values, the frequency response of doped films has not previously been addressed. The present study shows that the dielectric relaxation is most severe at concentration levels where the highest *k*-values are achieved. To be able to implement doped dielectric films in future semiconductor devices, the frequency response of the films must be understood.

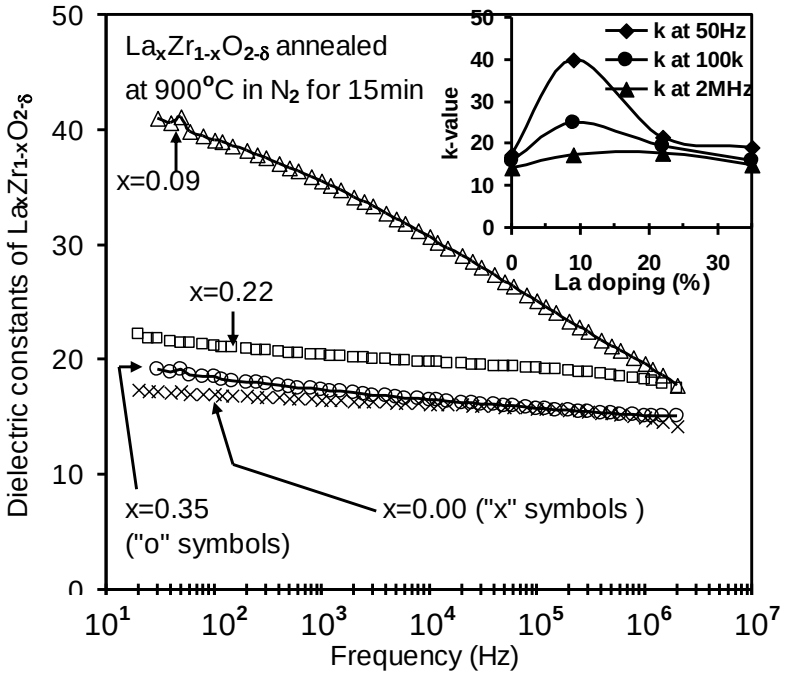

Figure 5-4. *Frequency dependence of the k-value of annealed $La_xZr_{1-x}O_{2-\delta}$ thin films. An inset shows the change in k-value with doping level, at different frequencies.*

The effect of annealing on the dielectric relaxation is shown by the results in Figure 5-5 which contains the results of as-deposited and annealed samples with a La concentration of x=0.09 and x=0.35. Solid lines are fitted results using either CS or CS + KWW relationships. For the x=0.35 dielectric (open and closed circle symbols), the annealing improves the dielectric relaxation and has weak effect on the k-value, that is, there is a small increase in k-value at some frequencies and there is a flatter frequency response compared to the as-deposited sample. For the x=0.09 as-deposited sample, the k-values are low and annealing (and hence crystallization into predominantly the tetragonal or cubic phase) produces the high k-values. It is possible that the dielectric relaxation behavior observed is due to the level of stress in the

crystalline grains, depending on the grain size, analogous to the behavior of ferroelectric ceramics.

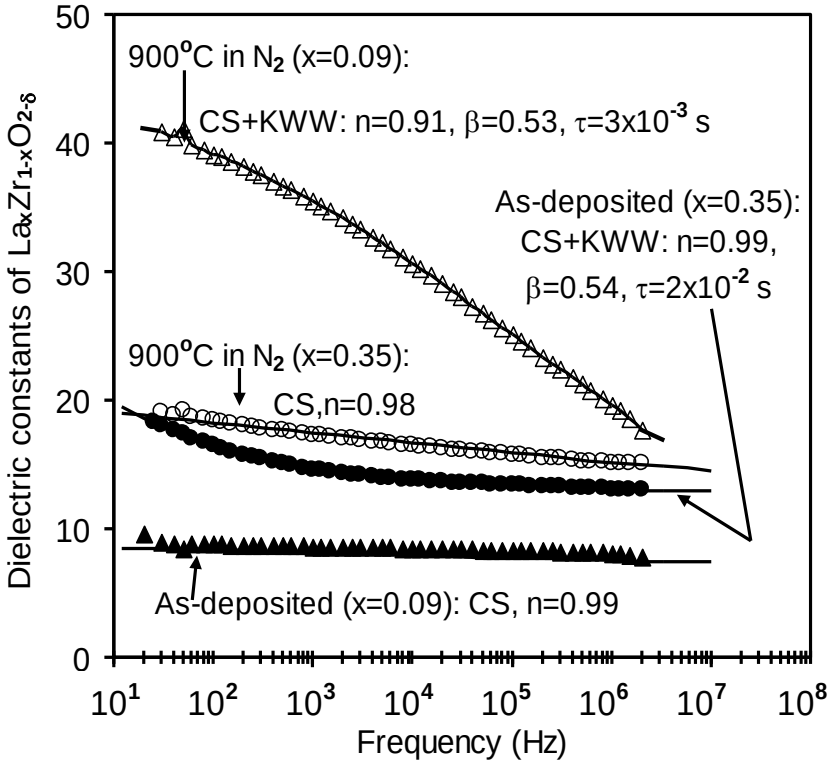

Figure 5-5. *A comparison between $La_xZr_{1-x}O_{2-\delta}$ as-deposited and annealed samples.*

5.2 As-Deposited and Post Deposition Annealed Cerium Oxides

Figure 5-6 is XRD diffraction patterns for 250 °C as-deposited and annealed samples. The grain size of annealed sample (9.55 nm) is bigger than the original sample (8.83 nm), which suggest that post deposition annealing in

vacuum (700 °C - 900 °C) causes an increase in the size of the crystalline grains. The same phenomenon is also recorded in the 150 °C as-deposited and annealed samples.

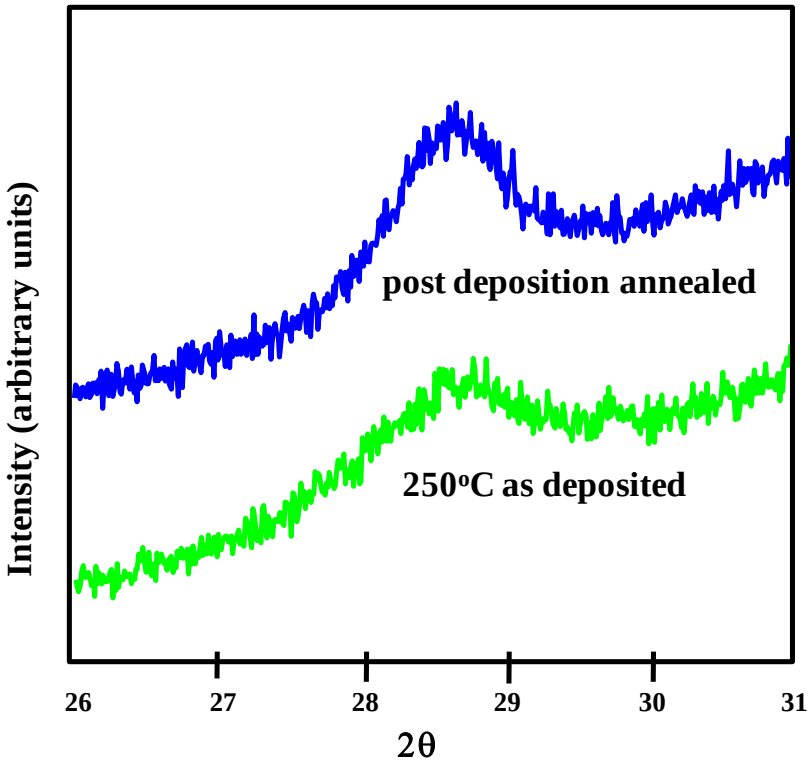

Figure 5-6. *XRD patterns for the 250°C samples (green for the as-deposited and blue for the post deposition annealed).*

C-V measurements are used to characterize frequency dispersion[5] and obtain permittivity of CeO_2 thin films. A typical set of C-V characteristics of the as-deposited (dashed line) under different frequencies (100 Hz, 1 kHz, 10 kHz, 100 kHz and 1 MHz) is shown in Figure 5-7 for the sample of deposition temperature 150 °C. Remarkable frequency dispersions on C-V curves are

observed for both the as-deposited and the annealed samples. Compared to the as-deposited samples, the annealed samples show pronounced accumulation capacitance reduction. The most important effect of annealing is related to weakened accumulation capacitance and hence reduced *k*-value. C-V measurements are carried out from strong inversion (-1 V) toward strong accumulation (2 V). Noticeable frequency dispersions on C-V curves are observed. Similar cases also happened in rest of the as-deposited samples (deposition temperature: 200 °C - 350 °C). Under the frequency of 1 MHz, the capacitance is 310 pF in strong accumulation. Enhanced capacitance (1420 pF) in strong accumulation under the frequency of 100 Hz is observed. The capacitance value is more than four times of the 1 MHz case. Moreover, it is found that the tendency of strong accumulation capacitance is inverse-linear with frequency. In contrast, C-V measurement of the annealed sample (solid line) is also demonstrated in Figure 5-7. Compared to the as-deposited high-*k* film, the annealed sample shows pronounced accumulation capacitance reduction. The most obvious effect of annealing is related to weakened accumulation capacitance and hence reduced *k*-value. Insignificant frequency dispersion is observed from 100 Hz to 1 MHz. The capacitance at 100Hz of annealed sample decreases by approximately 70% compared with the as-deposited one. The accumulation capacitance value is 410 pF. The capacitances from 1 kHz to 1 MHz are in the range of 180 pF - 240 pF. Similar relieving frequency dispersions are also seen for the 250 °C annealed sample

(compared to 250 °C as-deposited sample). The dielectric constant can be extracted from the capacitance values in strong accumulation. In Figure 5-7, for the 150 °C as-deposited sample, the extracted *k* value at 1 MHz is 42. Likewise, the *k* value at 1 MHz is 36 for the 150 °C annealed sample.

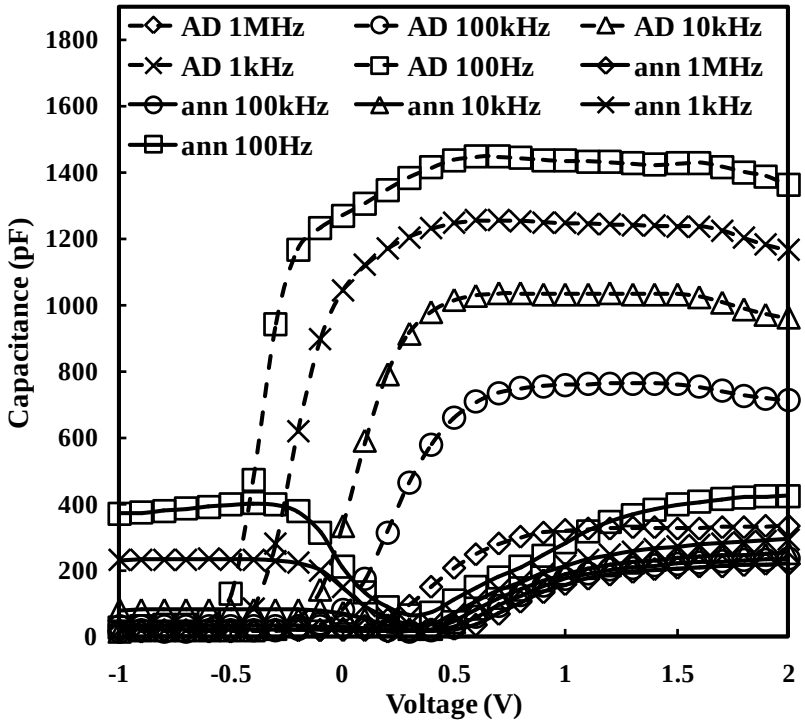

Figure 5-7. *Capacitance-Voltage (C-V) measurement of the as-deposited (AD) and the annealed (ann) samples under different frequencies (100Hz, 1kHz, 10kHz, 100kHz and 1MHz).*

In order to further investigate the *k*-value dependent frequency dispersion for CeO_2, normalized dielectric constant is quantitatively utilized to characterize the dielectric constant variation. At the very start, as-deposited and annealed samples are used. Concerning the 250 °C sample, the

comparison between the as-deposited and annealed is given in Figure 5-8. It is observed that the dielectric relaxation for the as-deposited sample (triangle-symbol) is serious than the annealed one (square-symbol). From the analysis at all frequencies, the normalized *k* value of the as-deposited sample is lower. Obviously, the worst case happens at 1 MHz and the normalized dielectric constant is 0.11. It means that the *k* value is only 10% of the highest *k* value measured at 100 Hz. The conclusion is made upon the data that the CeO_2 samples have eased frequency dispersion after annealed. From the analysis of Figure 5-6, the grain size for annealed samples is larger than the as-deposited one. It is easy to make an inference that grain size affects dielectric relaxation. The smaller grain size has bigger dielectric relaxation.

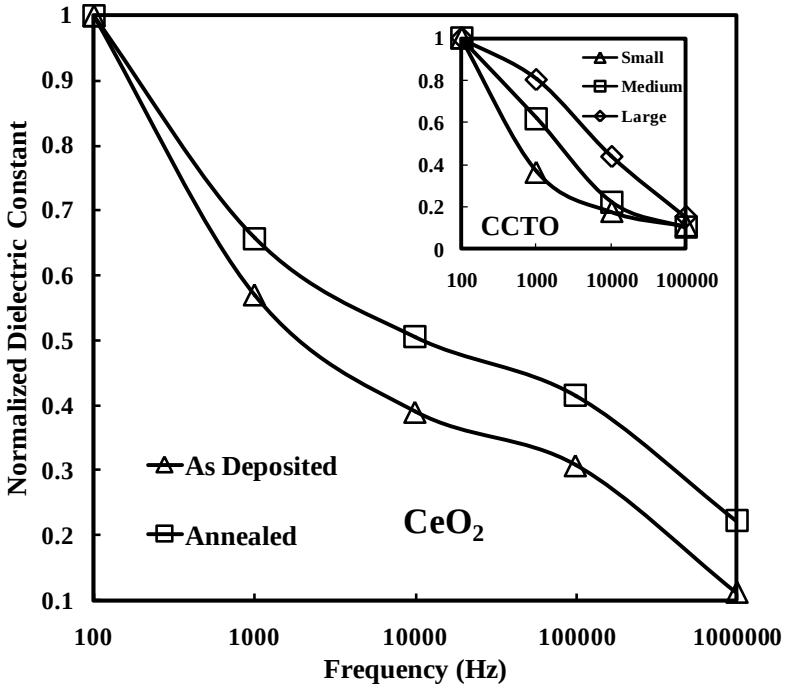

Figure 5-8. *Normalized dielectric constants for the as-deposited and the annealed samples under different frequencies (100Hz, 1kHz, 10kHz, 100kHz and 1MHz).*

These findings are in good agreement with theoretical and experimental studies which confirm that grain size makes significant impact on dielectric relaxation. Yu et al.[6] reported the effect of grain size on the ferroelectric relaxor behavior in $CaCu_3TiO_{12}$ (CCTO) ceramics. The normalized dielectric constant value of CCTO over frequency response (100, 1k, 10k and 100k Hz) is extracted as supporting evidence here, which is shown in the inset of Figure 5-8. CCTO ceramics with different grain sizes (small, medium and large) were prepared. Strong frequency dispersion of dielectric constant for all the grain size is related to the frequency dependent board and shift of glasslike transition temperature. It is finally associated with the slowing down of dipolar fluctuation within the polar nanodomain. The dielectric relaxation for small grain size sample is the worst. The dielectric constant at 100k Hz is only 10% of the value at 100 Hz, which is similar to the as deposited temperature 250 °C CeO_2 sample. The medium grain size CCTO sample is superior to the small sample at all frequencies. Moreover, the large grain size sample performs better than the medium one. The effect of grain size mainly originates from higher surface stress in smaller grain due to its higher concentration of grain boundary. To illustrate this point, surface stress in grain is high, medium and low for the small, medium and large grain size CCTO samples. As surface stress increases, the glasslike transition temperature decreases considerably. It is attributed to the enhancement of the correlations among polar nanodomain. Ultimately, both frequency dispersion and

relaxation strength, as typical characteristic of relaxor ferroelectrics, will increase when grain size decrease.

5.3 As-Deposited Cerium Oxides under Various Deposition Temperatures

XRD diffraction patterns for films as-deposited at 150 °C, 200 °C, 250 °C, 300 °C and 350 °C are shown in the inset of Figure 5-9. Diffraction scans with a slower scan speed were performed in the region of the peak to obtain full width at half-maximum data (the most distinct diffraction peak). XRD results show crystalline diffraction features for all deposition temperatures. The grain size value is obtained by Scherrer formula[7] based on XRD data (in Figure 5-9). The measurements performed have the grain size changing from 6.14 nm for the 150 °C sample, to 23.62 nm for the 350 °C sample. For 200 °C, 250 °C and 300 °C samples, the grain size are 6.69 nm, 8.83 nm and 15.86 nm respectively. There is a clear trend that the grain size increases with increasing deposition temperature, which might be attributed to increased mobility of the deposited material with increased deposition temperature.

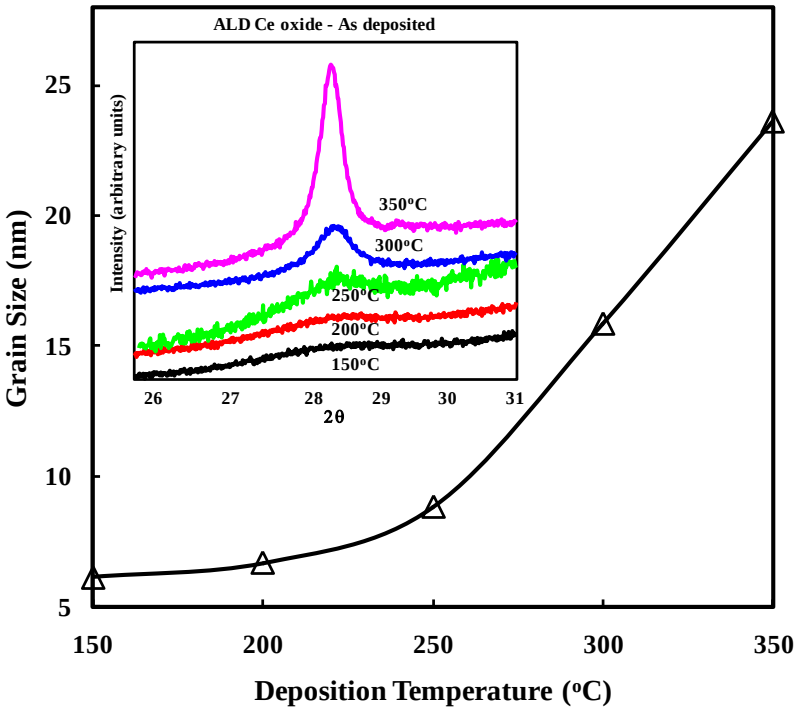

Figure 5-9. *Grain sizes for the as-deposited CeO_2 samples under different deposition temperatures (150°C, 200°C, 250°C, 300°C and 350°C).*

Figure 5-10 lists normalized dielectric constant for all as-deposited CeO_2 samples under the deposition temperatures (150 °C, 200 °C, 250 °C, 300 °C and 350 °C). It is known from XRD (Figure 5-9 inset) and Raman scattering spectrum that grain size increases as deposition temperature increases. The relationship between grain size value and deposition temperature is explained as follow: 6.13 nm for 150 °C, 6.69 nm for 200 °C, 8.83 nm for 250 °C, 15.85 nm for 300 °C and 23.62 nm for 350 °C. Large dielectric relaxation happens for the sample of 6.13 nm (diamond-symbol). The minimum *k* value at 1 MHz is one third of the maximum value at 100 Hz. When deposition temperature increases, the dielectric relaxation is even worse for the sample of

6.69 nm (square-symbol). The *k* value variation is more significant at all the frequencies. In addition, the most severe dielectric relaxation is recorded for the sample of 8.83 nm (star-symbol). It is noted that the sample of 8.83 nm has the worst dielectric relaxation for both as-deposited and annealed samples. The worst case is that the *k* value at 1 MHz takes only 10% of the *k* value at 100 Hz. From the figure, the normalized dielectric constants are the lowest for all the frequencies, which means the dielectric constant makes the most significant value drop in the region of higher frequencies. The sample of 15.85 nm (triangle-symbol) has significant improvement on dielectric relaxation. The *k* value variation is narrowed. The sample of 23.62 nm (round-symbol) shows more stable frequency response for the *k* value. As a consequence, it is not always true for the inference we made above: the smaller grain size has a larger dielectric relaxation (the sample of 8.83 nm has the worst dielectric relaxation, but 8.83 nm is not the smallest grain size value among all the samples). Nevertheless, if a comparison is made between samples of 6.13 nm (the smallest) and 23.62 nm (the largest), the larger grain size sample is proved to have better performance on dielectric relaxation under high frequency measured condition. It is also consistent with the experimental results we obtained before[8].

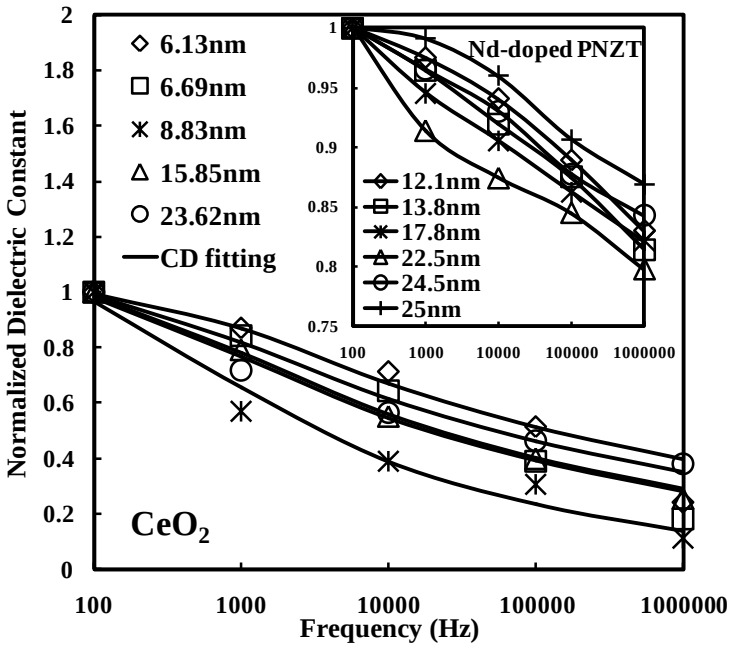

Figure 5-10. *Normalized dielectric constants for the as-deposited samples under different frequencies (100Hz, 1kHz, 10kHz, 100kHz and 1MHz).*

Similarly, the effect of grain size on dielectric relaxation is found on the Nd-doped $Pb_{1-3x/2}Nd_x(Zr_{0.65}Ti_{0.35})O_3$ composition (PNZT)[19], where x = 0.00, 0.01, 0.03, 0.05, 0.07, 0.09. PNZT were prepared by traditional mixed oxide solid state reaction method. The grain size decreases with increasing Nd doping (x). The normalized dielectric constant vs. frequency is extracted in the inset of Figure 5-10. Strong frequency dispersion is observed for all the samples. It is clear that the deteriorative degree of dielectric relaxation increases from 12.1 nm, reaches the peak at 22.5 nm and then declines. A comparison between samples of 12.1 nm and 25 nm is made. Uniformly, the sample with the grain size of 25 nm is shown to perform superior on dielectric relaxation. The dielectric constant frequency response of the PNZT samples shares exactly the

same with CeO_2 samples. One possible reason of the observation above could be due to the broadened dielectric peak and the transition temperature shift. The dielectric constant shows phase transition as expected for normal ferroelectrics. The region around the dielectric peak is broadened, which is one of most important characteristics of disordered perovskite structure with diffuse phase transition. Transition temperature is found to shift forward lower temperature with the grain size from 12.1 nm to 22.5 nm, with further larger grain size remained at the same position. Concerning the strong frequency dispersion, it is mainly attributed to the low frequency space charge accumulation effect. Such strong frequency dispersion in dielectric constant appears to be a common feature in ferroelectrics associated with non-negligible ionic conductivity.

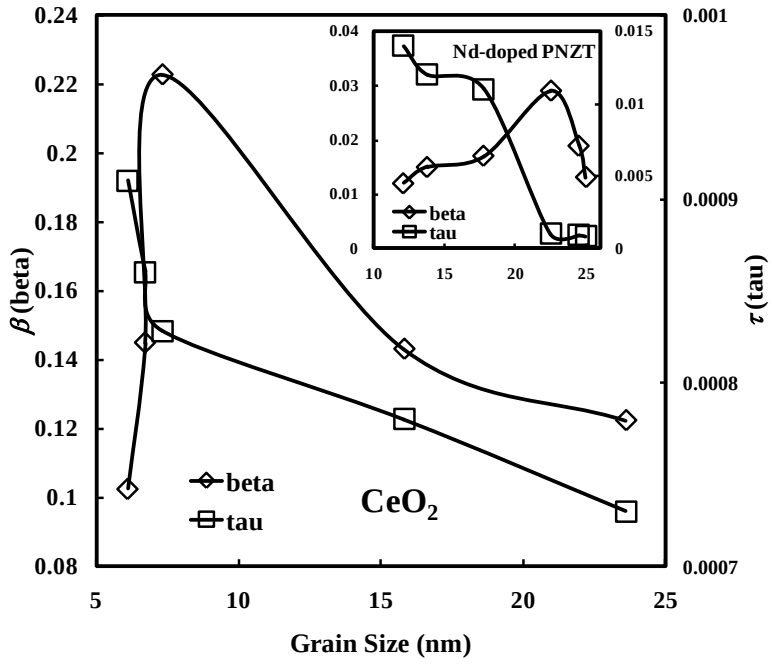

Figure 5-11. *Cole-Davidson fitting parameters: β (beta) and τ (tau) for the as-deposited CeO_2 samples with different grain sizes.*

Dielectric relaxation can be described by Cole-Davidson (CD) law for all the CeO_2 samples. CD fitting are denoted as the solid-lines in the Fig. 6. CD law is widely used in glass forming materials to explain the frequency dependent dielectric relaxation[10]. The fitting parameters of CD equation: β (beta) and τ (tau) are demonstrated in Figure 5-11. Left Y coordinate axis is for beta value and right Y coordinate axis is for tau value. Subsequently, X coordinate axis is for the grain size of the samples. It is clear that the trend of beta increases from 6.13 nm, peaks at 8.83 nm with the beta value of 0.21 and then descends. Thus, the curve of beta is found to be consistent with deteriorative degree of dielectric relaxation, which agrees with fact that the slop of the real part ε' to frequency is dependent on parameter beta. Furthermore, the asymmetry of loss factor is more serious as the parameter beta increases. For the parameter tau, the trend decreases from 6.13 nm to 23.62 nm. The real part of CD equation shifts horizontally to higher frequency value as the values of tau decrease. Usually, tau is identical in form with Vogel-Fulcher-Tammann (VFT) law for the temperature dependence of viscosity of a number of polar materials[11]. Through VFT law, activation energy and freezing temperature can be obtained. Tau is probably determined by the depositon temperature. So the related activation and freezing temperature could be calculated afterwards. The cause for a distribution of relaxation times occasionally has been made associated with certain particular cases, e.g. the suggestion made by Kliem and Arlt[12] concerning the occurrence of

protonic resonance, Cabeza et al.[13] concerning the porosity effect. Equally, dielectric relaxation of the PNZT samples can be modeled by CD law as well. The inset of Figure 5-11 shows the relationship between CD fitting parameters (beta and tau) and grain size likewise. The trend of beta rises from 12.1 nm, peaks at 22.5 nm with the beta value of 0.03 and then glides back downwards within the range of 22.5 nm to 25 nm. The beta is proven to represent the deteriorative degree of dielectric relaxation. In the same manner, the trend of tau decreases from 12.1 nm to 25 nm.

References

1. Schroeder T: Physics of dielectric and DRAM. *IHP Im Technologiepark* 2010, Frankfurt, Germany.
2. Zhao CZ, Taylor S, Werner M, Chalker PR, Murray RT, Gaskell JM, Jones AC: Dielectric relaxation of lanthanum doped zirconium oxide. *Journal of Applied Physics* 2009, 105: 044102.
3. Fischer and A. Kersch, The effect of dopants on the dielectric constant of HfO2 and ZrO2 from first principles, *Appl. Phys. Lett.* 2008, 92, 012908.
4. S. Govindarajan, T. S. Boscke, P. Sivasubramani, P. D. Kirsch, B. H. Lee, H. –H. Tseng, R. Jammy, U. Schroder, S. Ramanathan, and B. E. Gnade,

Higher permittivity rare earth doped HfO2 for sub-45-nm metal insulator semiconductor devices, *Appl. Phys. Lett.* 2007, 91, 062906.

5. Tao J, Zhao CZ, Zhao C, Taechakumput P, Werner M, Taylor S, Chalker PR: Extrinsic and intrinsic frequency dispersion of high-*k* materials in capacitance-voltage measurements. *Materials* 2012, 5: 1005-1032.
6. Yu HT, Liu HX, Hao H, Guo LL, Jin CJ: Grain size dependence of relaxor behavior in $CaCu_3Ti_4O_{12}$ ceramics. *Appl Phys Lett* 2007, 91: 222911.
7. Scherrer P: Estimation of the size and internal structure of colloidal particles by means of Rontgen. *Gott Nachr* 1918, 2: 98-100.
8. King PJ, Werner M, Chalker PR, Jones AC, Aspinall HC, Basca J, Wrench JS, Black K, Davies HO, Heys PN: Effect of deposition temperature on the properties of CeO_2 films grown by atomic layer deposition. *Thin Solid Films* 2011, 519: 4192-4195.
9. Mohiddon MA, Kumar A, Yadav KL: Effect of Nd doping on structural, dielectric and thermodynamic properties of PZT (65/35) ceramic. *Physica B* 2007, 395: 1-9.
10. Dotson TC, Budzien J, McCoy JD, Adolf DB: Cole-Davidson dynamics of simple chain models. *J Chem Phys* 2009, 130: 024903.
11. Ngai KL, McKenna GB, McMillan PF, Martin S: Relaxation in glass forming liquids and amorphous solids. *J Appl Phys* 2000, 88: 3113-3157.
12. Kliem H, Arlt G: A relation between dielectric distribution functions and structural properties of amorphous matter. *CEIDP Annu Rep* 1987, 56: 325.

13. Cabeza M, Keddam M, Novoa XR, Sanchez I, Takenouti H: Impedance spectroscopy to characterize the pore structure during the hardening process of Portland cement paste. *Electrochim Acta* 2006, 51: 1831-1841.

Chapter 6: Conclusion and Further Work

In summary, in the thesis, extrinsic and intrinsic frequency dispersion has been investigated and discussed in detail. Two causes of extrinsic frequency dispersion were investigated: firstly the parasitic effect (series resistance, back contact imperfection, cables and connections) and the lossy interfacial layer. These effects were analyzed and modeled based on correction models. Secondly, the surface roughness was observed in ultra-thin dioxide thin films. However, after AFM micrographs were analyzed, the surface roughness was found to be not responsible for the observed frequency dispersion of the thick high-*k* dielectric thin films (>3 nm).

After causes for the extrinsic frequency dispersion were considered and determined, intrinsic frequency dispersion (dielectric relaxation) was found to be strongly related to the frequency dependence of the *k*-value on the high-*k* MOS capacitors. For low levels of doping (~10%), *k*-values of 39 and 33 were obtained from the $La_{0.09}Zr_{0.91}O_{2-\delta}$ thin film and $Ce_{0.1}Hf_{0.9}O_{2-\delta}$ thin film, respectively, at 100 Hz; while no significant enhancement of the *k*-value was achieved with high levels of doping (such as 35%).

The dielectric relaxation models in the frequency domain (such as the

Cole-Cole equation, the Cole-Davidson equation, the HN equation) and in the time domain (such as the KWW law and the CS law) were comprehensively considered. The dielectric relaxation results of the $Ce_xZr_{1-x}O_{2-\delta}$, $LaAlO_3$, ZrO_2 and $La_xZr_{1-x}O_{2-\delta}$ thin films may be described by either the combined CS+KWW laws or the HN relationship. The fitting results of the HN equation showed that the asymmetry of the dielectric loss peak β increases with decreasing concentration levels of La x. For a severe dielectric relaxation (for example, the significant decrease of the k-value with increasing frequency for the $La_{0.09}Zr_{0.91}O_{2-\delta}$ thin film), the width change of the loss peak α played an important role during data fitting. For the $La_{0.09}Zr_{0.91}O_{2-\delta}$ thin film, it was found that the combined CS+KWW relaxation process (β_k = 0.53 and n = 0.91) can be substituted by the HN function where distribution parameters α and β were 0.6535 and 0.3458, respectively because both the HN function and the combined CS+KWW relationship had two distribution parameters.

It was found that dielectric relaxation is related to the size of the crystal grains formed during annealing and that doping affects the size of the crystal grains formed. CeO_2 thin films were found to be deposited as a crystalline film for a range of substrate temperatures within the ALD growth window of the $Ce[mmp]_4$ precursor with water as an oxidant. XRD and Raman scattering spectrum show an increase in grain size for increasing growth temperatures. From C-V measurement of the samples, strong frequency dispersion is observed. In order to further investigate dielectric relaxation, the normalized

dielectric constant is utilized for CeO_2 samples of different grain sizes. CeO_2 sample has better dielectric relaxation after annealing since the annealed sample has larger grain size. Within the grain size range of CeO_2 samples (6.13 - 23.62 nm), the most serious dielectric constant frequency dispersion is found in the sample of 8.83 nm. Similarly, the relationship between grain size and dielectric relaxation is also observed in CCTO and Nd-doped PNZT samples. The mechanism of grain size effects is attributed to the alignment enhancement of the polar nano-domains.

The rapid growth of the Flash memory market has been driven by the increase of memory capacity and the decrease of unit price, due to the continuous downscaling of Flash memory cells. However, the scaling of the conventional SiO_2-based tunnel and control dielectric layers in Flash memory technology is fast approaching its limits, as increasing leakage current through thinner SiO_2 layers will result in a fast data loss. According to the ITRS Roadmap 2013, this becomes the most pressing issue to be solved for floating-gate Flash memory. Furthermore, starting from the 45-40 nm technology generation for floating-gate Flash devices, the spacing between two adjacent floating gates becomes too small to allow the control gate to overlap the floating gate on the vertical sidewalls in minimum feature-sized cells. In order to maintain the coupling ratio, this will require a further reduction of the dielectric thickness between control and floating gates, i.e., the inter-poly dielectric (IPD), which will, in turn, inevitably increase the

leakage and degrade the data retention.

The introduction of high-*k* materials as the IPD in floating-gate Flash memory has been proposed as a potential solution. Higher dielectric constant will increase the IPD capacitance without reducing its physical thickness and therefore help in maintaining the coupling ratio and allow the cell size to continue downscaling. A large amount of work will be carried out to investigate the capabilities and limits of using high-*k* layers to replace the conventional oxide-nitride-oxide stack in the further works. The key issues are the capabilities of the SiO_2/high-*k* layers to provide enough program/erase windows, sufficient data retention and endurance, and most importantly, a low leakage to guarantee longer retention.